SIMULATING LUMINANCE DISTRIBUTIONS OF LUMINAIRES FROM RAY FILES

Jan AUDENAERT

Jury:
Prof. dr. ir. Jean Berlamont, president (Department of Civil Engineering, KU Leuven)

Prof. dr. ir. Geert Deconinck, promotor (ESAT-ELECTA, KU Leuven)

Prof. dr. Peter Hanselaer, promotor (Light and Lighting Laboratory, KU Leuven)

Dr. Guy Durinck, promotor (Light and Lighting Laboratory, KU Leuven)

Prof. dr. ir. Philip Dutré, assessor (Computer Graphics Group, KU Leuven)

Prof. dr. ir. Patrick De Visschere,assessor (ELIS, Ghent University)

Prof. dr. Youri Meuret, assessor, (Light and Lighting Laboratory, KU Leuven)

Prof. dr. ir. Ben Somers (Division Forest, Nature and Landscape, KU Leuven)

Dr. Rudy Geens (Havells-Sylvania)

Dissertation presented in partial fulfilment of the requirements for the degree of Doctor in Engineering

June 2014

ISBN 978-94-6018-846-6
D/2014/7515/70

Preface

Four years ago I was thrilled when I could finally say my master's thesis was finished – I thought my studying days were over and felt ready to pursue a life of happiness in the industry. Several days later someone asked me if I would be interested in starting a Phd. at the Light & Lighting laboratory. This was an opportunity not included in my grand scheme of life at that time. After thinking it through, I decided wholeheartedly to accept the challenge.

And a challenge it was.
Starting out with a degree in information and communication technology meant a vast amount of studying to get a grasp of the nature of light. Lifelong learning, a buzzword these days, turned out to be quite enjoyable. Looking back, these past four years have been a great experience on so many levels. Foremost, due to a number of people for whom I would like to take this opportunity to express my gratitude.

First I would like to thank my supervisors; prof. dr. ir. Geert Deconinck, dr. Guy Durinck and prof. dr. Peter Hanselaer, for: the continuous support and guidance, proofreading my publications and – to be honest – for the incessant patience and trust, even when there where longer periods that my research did not produce any successful results.

Furthermore, I wish to thank my Phd. assessors; prof. dr. ir. Philip Dutré, prof. dr. ir. Patrick Devisschere and prof. dr. Youri Meuret for their expertise on which I could rely. Each, being from a different scientific domain, provided valuable insights on how the performed work could be improved.

Similarly, I want to thank all the members of the examination committee for evaluating this dissertation and for giving comments and suggestions on the contents.

Of course, none of this would have been possible without the financial funding from the agency for Innovation by Science and Technology (IWT – sb grant #091442). Thanks to the IWT, I was able to carry out my research, acquire new testing and measurement equipment, visit international conferences and more important: it allowed me to focus on my research without having to worry about funding during the past four years.

To all my past and present colleagues of the Light & Lighting laboratory: thank you for the cooperation and friendly atmosphere. Each and every one of you were always very helpful in providing assistance when asked. While each individual has their own background and expertise, together we form an excellent team – something which is clearly visible when looking at the many successful collaborations with the industry and the academic achievements of the laboratory.

It is known that a person is shaped to who he is by his environment and past experiences. Undoubtedly, without my parents assistance, guidance, advice and loving care throughout the years I would not be writing this. While being from a large family with five children, I could always rely on them no matter what.
I thank you both for everything you have done for me!
I sincerely hope, life will be kind for the both of you to still be around for a long time to come, making it possible to witness these kind of great milestones of any of your children.

Finally, Magali, thank you for your love, support and patience during the past years. I consider myself lucky to have found someone like you who is there for me and who understands what I am trying to say without necessarily having to say a thing. You truly motivated me to keep on going and made me thoughtful on what the really important things are in life.

Jan Audenaert
Gent, June 2014.

Abstract

For luminaires having a non-uniform luminance distribution, glare evaluation should be based on luminance maps. However, if the light source within the luminaire is modeled as a ray file, which is essential if the optics surrounding the light source are in close proximity, such luminance maps cannot be simulated directly in ray tracing software.

A method that makes use of a brute force ray tracing approach to enable the simulation of luminance maps is presented. While this method yields valid results, it does however require huge amounts of computing power and time. An alternative technique based on ray file sampling in combination with geometrical modeling is presented and discussed. This method does not have the drawbacks of the brute force approach and results in highly accurate luminance distributions.

In addition, the impact of the Bidirectional Scattering Distribution Function (BSDF) of a material on the quality of the ray file of a luminaire is investigated. The reflecting properties of a highly diffuse material and a more specular material are modeled in various ways and the impact on the ray file and the corresponding luminance distributions is analyzed.

Finally, keeping in mind that the BSDF plays an important role in shaping the near-field, a study is performed to gain insight into how a measured BSDF is influenced by the characteristics of the BSDF measurement setup itself such as beam diameter and detector aperture. In literature, BSDF variations as large as an order of magnitude have been reported in round-robin tests where several labs measured the same sample. Much of these variations can be attributed to the specific design of the measurement device. To minimize this influence, a deconvolution method is presented to reconstruct the true BSDF from experimental data. The subsequent effects of this procedure on the luminance maps is illustrated.

Samenvatting

Tot op vandaag worden verlichtingstoestellen vooral gekarakteriseerd m.b.t. hun intensiteitsverdeling in de ruimte en de verlichtingssterkte die gegenereerd wordt op het taakoppervlak. Het uitzicht van het verlichtingstoestel zelf wordt meestal niet in overweging genomen. Nochtans biedt de luminantieverdeling van een toestel noodzakelijke informatie om ook de lichtkwaliteit te kunnen inschatten. De mate van verblinding veroorzaakt door een verlichtingstoestel met een niet-uniforme luminantieverdeling zal immers gebaseerd zijn op de speciefieke luminantieverdeling van dat verlichtingstoestel. De huidige ray-tracingsoftware is in staat om luminantieverdelingen te genereren op voorwaarde dat het toestel wordt gedefinieerd als een oppervlaktebron. Om nauwkeurige optische simulaties uit te voeren, wordt de lichtbron, en dus ook het toestel, optisch gemodelleerd als een *ray file*. In dit geval is het niet mogelijk om met de huidige ray-tracingsoftware deze luminantieverdelingen te simuleren.

Een eerste methode om toch deze luminantieverdelingen te kunnen simuleren is gebaseerd op een zogenaamde *brute-force* methode. Deze methode, hoewel ze ons in staat stelt om kwalitatief goede luminantieverdelingen te simuleren, vergt zeer veel rekenkracht en/of rekentijd.
In dit doctoraat wordt een alternatieve methode, gebaseerd op het bemonsteren en geometrisch modeleren van een *ray file*, voorgesteld. De berekeningstijd is aanvaardbaar en de nauwkeurigheid van deze methode is bovendien ook zeer hoog.

Niet enkel de lichtbron maar ook de lichtverstrooiingseigenschappen aan het oppervlak van een materiaal dat zich rond de lichtbron bevindt (*Bidirectional Scattering Distribution Function – BSDF)* hebben een belangrijke invloed op de luminantieverdelingen van het complete verlichtingstoestel. Deze invloed wordt geanalyseerd door de *BSDF* van zowel een diffuus materiaal als een meer spiegelend materiaal te meten en te modelleren. Vervolgens worden luminantieverdelingen gesimuleerd, rekening houdend met deze verschillende types van *BSDF*-karakterisatie.

Aangezien de specifieke *BSDF-waarden* zelf ook een grote impact hebben op luminantieverdelingen, wordt er nagegaan in welke mate de *BSDF* nauwkeurig kan bepaald worden en welke invloed het *BSDF* meetinstrument heeft op het verkregen resultaat. De voornaamste vervormingen geïntroduceerd door het meettoestel zelf komen voort uit de eindige diameter van de lichtbundel waarmee het te karakteriseren materiaal belicht wordt en de eindige apertuur van het meettoestel.

Aangezien er geen echte standaard meetopstelling werd gedefinieerd, is het dan ook bijzonder moeilijk om waarden, bekomen via verschillende toestellen, met elkaar te vergelijken. In de literatuur werd melding gemaakt van een *round-robin* test en afwijkingen met grootte-orde factor 10 werden gerapporteerd. Om de invloed van het meettoestel op de meting te neutraliseren, zonder het toestel fysisch aan te passen, wordt in dit doctoraat een deconvolutietechniek voorgesteld. Er wordt ook nagegaan in welke mate het al dan niet toepassen van deze deconvolutie op de *BSDF* data een invloed heeft op de gesimuleerde luminantieverdelingen.

List of abbreviations

ASTM	American Society for Testing and Materials
BEF	Brightness Enhancement Film
BRDF	Bidirectional Reflectance Distribution Function
BSDF	Bidirectional Scattering Distribution Function
BTDF	Bidirectional Transmittance Distribution Function
CAD	Computer Aided Design
CCD	Charged-coupled device
CDM	Ceramic Discharge Metal-halide
CIE	Commission Internationale de l'Eclairage
CPU	Central Processing Unit
CV	Coefficient of Variation
DOI	distinctness-of-image
FWHM	Full Width at Half Maximum
GPMCPET	Gloss Painted MicroCellular PolyEthylene Terephthalate
GPU	Graphics Processing Unit
LCD	Liquid Crystal Display
LED	Light Emitting Diode
LID	Luminous Intensity Distribution
MCPET	MicroCellular PolyEthylene Terephthalate
NCC	Normalized Cross Correlation
NRMSE	Normalized Root Mean Square Error
RCS	Ray Collecting Surface
RPLED	Remote Phosphor LED
TIS	Total Integrated Scatter
Xe	Xenon

Table of contents

Chapter 1

Introduction

1.1 Optical design of luminaires

Luminaires have become ubiquitous in everyday life, from road lighting/signalization and indoor lighting to industrial and highly specialized lighting. All these luminaires however have one thing in common: they were designed to meet specific requirements with regard to typical optical quantities such as the total light output/efficiency and the luminous intensity distribution (LID) and/or illuminance distribution on a task surface.
However, more and more optical engineers acknowledge the need to investigate the luminance distribution of the lit luminaire during the development stage [Koshel, 2002]. Luminance distributions, i.e., luminance maps, are not only a tool to assess subjective criteria such as the aesthetics of the lit luminaire, but also provide objective information to assess criteria such as contrast [CIE 95, 1992], uniformity and the degree of discomfort glare [Kim et al., 2008; Teppei et al., 2006; Paul and Einhor, 2000; Eble-Hankins, 2008]. Indeed, discomfort glare, expressed in terms of the Unified Glare Rating (UGR) [CIE 117, 1995], can be calculated from average luminance values which are found by dividing far field intensity values by the surface area of the light source. However, for luminaires with a non-uniform luminance distribution, this approach becomes invalid, and glare evaluation should be based on luminance maps [CIE 205, 2013] which are converted to brightness images. Glare sources can then be identified from these brightness images [Nakamura, 2008]. Evidently these derived optical quantities are only as accurate as the data they are derived from, i.e., luminance distributions.

The design of optical systems is nowadays performed using ray tracing software as it allows virtual prototyping and as such enables a fast and less expensive development cycle because the number of test prototypes can be reduced drastically. A large variety of ray tracers are available ranging from ray tracers to calculate acoustics [Krokstad et al., 1968; Aretz and Vorländer, 2014] and even ballistics [Butler and Stephens, 2007] to ray tracers that trace light through a scene or optical system. The latter category can again be divided into two major application domains: computer graphics rendering [Dutré et al., 2006] and imaging/non-imaging optical design [Malacara, 2004; Smith, 2000]. While the techniques adopted in both domains are highly similar- light is discretized in rays and traced through a scene or optical system- the largest difference is situated in the requirements regarding accuracy and physical correctness. In computer graphics the laws of physics are quite bendable; models of light sources and optical properties of materials can be rather simple as the goal of computer graphics is primarily to create images that look good and realistic regardless whether they are physically correct. However, in imaging/non-imaging optical design the laws of physics have to be adhered to in order to enable physically accurate simulations.

Evidently, imaging/non-imaging optical ray tracing simulations can only be as accurate as the input which is given to the ray tracer. Three major input components can be distinguished for any ray tracing software: geometry, light source and optical properties of materials and surfaces. The geometry of a virtual model of an optical design is well defined as it is often drawn using traditional computer aided design (CAD) software. Additionally, the virtual model can be reproduced very accurately using either standard techniques such as casting, injection molding, high speed milling, etc. or the more advanced state-of-the-art 3D-printing techniques. As such, the accuracy of the geometry is not discussed in this thesis.

Unlike the geometry of a light source or luminaire, the optical properties of light sources, materials and surfaces are less straightforward to implement in ray tracing software.

Ray files of light sources offer a highly accurate description of a light source and are thus the preferred way to model a light source when accurate simulations are necessary [Joo et al., 2009]. Due to the nature of a ray file, spatial luminance distributions however cannot be directly obtained.

To model optical scattering of surfaces of materials, various reflectance/transmittance models exist and are often available as built-in libraries in ray tracing simulation software. However, in many cases these models are quite simple and as such large errors can be introduced in subsequent ray tracing simulations [Audenaert et al., 2011].

This work discusses and addresses these issues and presents techniques to enable the simulation of luminance distributions when a light source is characterized by a ray file. Additionally, it is investigated to what extent the optical modeling of surface scattering of materials influences simulated luminance distributions of luminaires.

A commercially available ray tracer, TracePro® from Lambda Research Corporation, has been used throughout this research. The presented techniques however are not restricted to this software and can be implemented in any ray tracer. A brief overview of the features of this ray tracer along with other popular ray tracers for imaging/non-imaging ray tracing is given in section 1.2. The optical measurement equipment is briefly presented in section 1.3. An overview of the performed research is given in section 1.4.

1.2 Ray tracing software for imaging/non-imaging optical design

Several commercial ray tracers are available for imaging/non-imaging optical design such as TracePro® from Lambda Research Corporation [TracePro, 2013], ASAP from Breault Research Organization [ASAP, 2013] and LightTools® from Synopsis Optical Solutions [Hayford and David, 1997; LightTools, 2013]. While the specific implementation of these ray tracers are different, they all share a common goal: to enable accurate physically correct simulations of an optical system. Additional utilities such as optimization modules are available for these ray tracers, which allows for an even faster design cycle and fine tuning of an optical system. The largest difference between these ray tracers is the 3D modeling: in ASAP a geometry is defined by surfaces that act as an interface boundary between different materials/media while in TracePro and LightTools the geometry is modeled as solid bodies which in turn contain surfaces.

In ray tracers, light rays having a radiant or luminous flux, starting position and direction, are emitted from a defined source and traced throughout the optical system, i.e. light tracing or forward ray tracing.

Each ray is checked for intersection with each surface present in the model through a ray/surface intersection algorithm. This technique is called non-sequential ray tracing as the order in which a ray intersects a surface is not known in advance. This allows the generation of so called child rays and stray light analysis. Sequential ray tracing on the other hand requires a user defined order in which each ray intersects each surface. While being significantly faster it does not allow stray light analysis. The above discussed ray tracers all implement a non-sequential ray tracing approach.

During the traversal of the optical system a ray can have several optical interactions with defined geometry to which optical properties are assigned. Such interactions include reflection, transmission, refraction, absorption,… These interactions will alter the payload of a ray (i.e. radiant flux) or the direction of the ray. After all rays have been traced through the optical system, an analysis can be performed to evaluate the optical properties of the whole optical system.

1.3 Measurement equipment

1.3.1 Near-field goniophotometer

The use of a ray file to model the optical characteristics of a light source is a well-known and popular method to achieve accurate results through light tracing when simulating properties such as the illuminance distribution on a task surface or the LID of luminaires. Especially if the source is interacting with optical components at a close distance (i.e. near-field region), ray files are the only way to achieve reliable results [Joo et al., 2009]. A ray file is merely a large collection of rays, each having a radiant or luminous flux, starting position and direction. If a sufficient number of rays are used, a highly accurate representation of a light source is achieved. This ray file however, cannot be measured directly but instead is generated from a collection of measured luminance distributions in combination with the total emitted luminous flux.

These measurements are performed in a near-field goniophotometer [Ashdown and Rykowski, 1998; Ashdown and Salsbury, 2006; Bredemeier et al., 2007; CIE TC-2-62, 2010; López et al., 2012], shown in figure 1.1, which features a calibrated luminance camera and a photometer attached to a rotating arm which moves to various positions on an imaginary spherical surface.

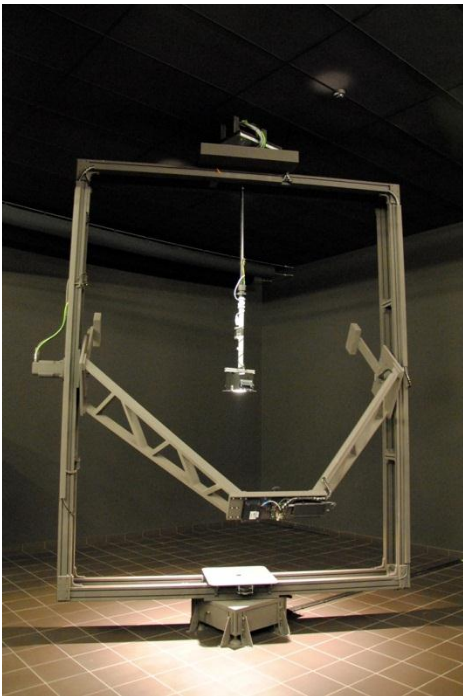

Figure 1.1 – Near-field gonio photometer type: RiGo801 for luminaires from TechnoTeam GmbH, with a light source aligned in the center of the device.

The light source for which a ray file is to be generated is aligned in the center of the device. Depending on the size of the light source or luminaire, a different size of near-field goniophotometer is required to maintain an adequate spatially resolved image captured by the luminance camera.

During a near-field measurement, the luminance camera captures relative spatial luminance distributions of the light source as seen from a specific point of view located on the imaginary sphere, while the photometer captures the local illuminance; these measurements are repeated for many points located on the imaginary sphere. As a result, a set of relative luminance images and illuminance values are recorded. The absolute total luminous flux emitted by the light source can then be calculated by numeric integration of the illuminance values. Each pixel of each captured luminance image contains a luminance value relative to the total emitted flux. Additionally each pixel of each luminance image corresponds to a different direction. As such, each pixel can be used to consider a ray for which the luminous flux and direction is known. From these data, it becomes possible to generate a LID as only the ray directions and associated luminous fluxes are needed. For a ray file however, one last piece of information is needed: the starting position of each ray. This position can be calculated by finding the intersection between the ray directions and a user defined bounding surface. This user defined surface should always be chosen as close as possible to the bounding surface of the light source.

As a near-field goniophotometer is equipped with a calibrated luminance camera, it is also possible to measure absolute luminance distributions of a light source as seen from a specific viewing direction. By measuring the luminance distribution with different integration times a high-dynamic range luminance distribution can be captured as is shown in figure 1.2.

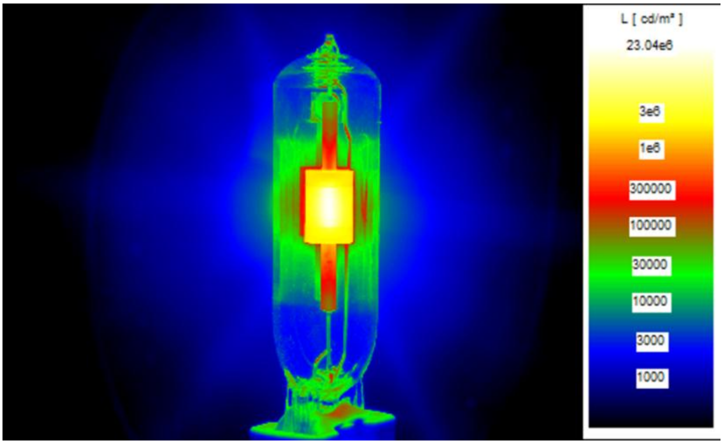

Figure 1.2 – A false color high-dynamic range luminance distribution of a Ceramic Discharge Metal-halide (CDM) lamp measured with a near-field goniophotometer type: RiGo801 for lamps and small luminaires.

Additionally the luminous intensity distribution can be measured directly using only the photometer under the condition that the largest dimension of the light source to be measured is at least 15 times smaller than the distance from the center of the device towards the photometer and the intensity distribution is not too narrow (far field approximation) [CIE 121, 1996].

1.3.2 Bidirectional Scattering Distribution Function measurement device

Surface scattering properties are fully described and defined by the bidirectional scatter distribution function (BSDF), which includes both the bidirectional reflectance distribution function (BRDF) and the bidirectional transmittance distribution function (BTDF). A BSDF measurement device measures the amount of light scattered by a surface as the direction of illumination or viewing is changed.

The spectral Bidirectional Scatter Distribution Function at wavelength λ, $BSDF_e$ or q_e, is defined as the surface radiance of a sample in a particular viewing direction, due to the scattering of radiation incident from a particular direction of irradiation:

$$BSDF_{\mathrm{e}}(\theta_{\mathrm{i}},\phi_{\mathrm{i}},\theta_{\mathrm{s}},\phi_{\mathrm{s}},\lambda)=\frac{\mathrm{d}L_{\mathrm{e,s}}(\theta_{\mathrm{i}},\phi_{\mathrm{i}},\theta_{\mathrm{s}},\phi_{\mathrm{s}},\lambda)}{\mathrm{d}E_{\mathrm{e,i}}(\theta_{\mathrm{i}},\phi_{\mathrm{i}},\lambda)}\left[\frac{1}{\mathrm{sr}}\right] \tag{1.1}$$

with (θ_i,ϕ_i) the spherical coordinates of the radiation incident on the surface, (θ_s,ϕ_s) the spherical coordinates of the light scattered from the surface, $\mathrm{d}L_{\mathrm{e,s}}$ the differential spectral radiance and $\mathrm{d}E_{\mathrm{e,i}}$ the differential spectral irradiance from a differential solid angle. All spherical coordinates are referenced to the surface normal.

To determine q_e of opaque, translucent or transparent materials from measurement data, the American Society for Testing and Materials (ASTM) has proposed the following practical formula [ASTM E2387, 2005]:

$$BSDF_{\mathrm{e}}=\frac{\Phi_{\mathrm{e},\lambda,\mathrm{s}}}{\Phi_{\mathrm{e},\lambda,\mathrm{i}}\Omega_{\mathrm{s}}\left|\cos\theta_{\mathrm{s}}\right|}\left[\frac{1}{\mathrm{sr}}\right] \tag{1.2}$$

with $\Phi_{\mathrm{e},\lambda,\mathrm{s}}$ and $\Phi_{\mathrm{e},\lambda,\mathrm{i}}$ the scattered radiant flux towards the detector and the incident radiant flux on the sample, respectively, Ω_{s} being the solid angle of the detector aperture.

The experimental setup for BSDF acquisition developed at the Light&Lighting Laboratory [Leloup et al., 2008], shown in figure 1.3, is ideally suited for measuring BSDFs of structured materials used in luminaire design, as a relatively wide collimated light bundle is used to illuminate the sample. Other important features of the device include: a double beam correction to ensure stability of the illumination system, a high uniformity of the illumination spot and a total uncertainty budget to fall within the range of 1.8 to 2.4% across the visible spectrum [Leloup et al., 2008]. The measurement instrument has a circular detector aperture with an adjustable diameter of maximum 25.4 mm at a distance of 886 mm from the measured sample, resulting in a maximum solid angle of $6.25\ 10^{-4}$ sr. The detector is mounted at the end of an optical bench which can be positioned into various positions on an imaginary spherical surface by rotation of two independent axes.

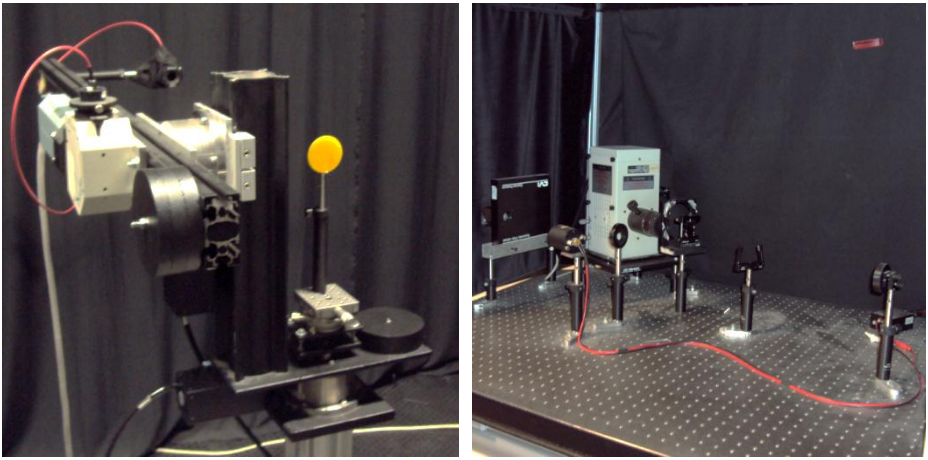

(a) (b)

Figure 1.3 – BSDF measurement set-up. (a) Sample holder and detector system consisting of two independent axes and a detector connected to a charged-coupled device (CCD). (b) Illumination system with a 300W Xe-Lamp, focusing mirror, double beam correction system and neutral density filter wheel.

1.4 Research questions

For luminaires having a non-uniform luminance distribution, glare evaluation should be based on luminance maps. At present, these luminance distributions cannot be simulated when light source models based on experimental near-field goniophotometric data are used. To enable these simulations, the following research questions will have to be answered:

- *When a light source is modeled as a ray file, which is essential if optics are in close proximity of the light source, how should luminance distributions be simulated?*

- *What is the effect of the optical modeling of the surface scattering properties of a material surrounding a light source on the simulated luminance distributions?*

- *How and to what extent can the process of measuring these optical surface scattering properties be improved in order to reduce the measurement error imposed by the measurement device itself?*

1.5 Overview

This doctoral thesis describes the approach and accuracy of a spatial and angular luminance distribution simulated from a given ray file. First, in chapter 2 a method that makes use of a brute force ray tracing approach is presented. While the presented method yields valid results, it does however require huge amounts of computing power and/or time.

In chapter 3, an alternative method based on ray file sampling in combination with a geometrical modeling is presented and discussed. This method does not have the drawbacks of the brute force approach and results in highly accurate luminance distributions.

Once the method to simulate accurate luminance distributions from ray files has been established, it is useful to explore the properties of the ray file itself. The impact of the BSDF of a material on the quality of the ray file of a luminaire is investigated in chapter 4. The reflecting properties of a highly diffuse material and a more specular material are modeled in various ways and the impact on the ray file and the corresponding luminance distributions is investigated.

Finally, keeping in mind that the BSDF plays an important role in shaping the near-field, a study is performed to gain insight as to how a measured BSDF is influenced by the BSDF measurement setup itself. In literature, measurement variations as large as an order of magnitude have been reported in round-robin tests where several labs characterized the same sample [Stover, 1995]. Much of these variations can be attributed to the specific design of the measurement device. To minimize the influence of the measurement device on the measured BSDF data, a deconvolution method is presented. The subsequent effects of such a deconvolution on luminance maps is illustrated.

In chapter 6, the general conclusions are summarized and future research is discussed.

Chapter 2

Simulating luminance distributions from ray files through brute-force ray tracing

2.1 Introduction

As discussed in chapter 1, luminance maps of a luminaire offer the possibility to predict contrast, uniformity and the degree of discomfort glare of luminaires having a non-uniform luminance distribution but also to predict the visual aesthetics of the lit luminaire. These are important design aspects when developing modern lighting fixtures, especially when using small and intense light sources like LED [Teppei et al., 2006; Paul and Einhor, 2000]. A luminance map displays the spatial luminance distribution in a particular viewing direction, with luminance defined as:

$$L = \frac{\mathrm{d}^2\Phi}{\mathrm{d}\Omega_\mathrm{o}\mathrm{d}A_\mathrm{s}\cos(\theta_\mathrm{s})}\left[\frac{\mathrm{cd}}{\mathrm{m}^2}\right] \tag{2.1}$$

with θ_s the angle between a vector normal to the source and a vector pointing from the part of the source under consideration to the observer o, $\mathrm{d}A_\mathrm{s}\cos(\theta_\mathrm{s})$ the apparent source area as observed by the observer, $\mathrm{d}\Omega_\mathrm{o}$ the solid angle subtended by the observer and $\mathrm{d}^2\Phi$ the luminous flux within the cone defined by the differential source area under consideration and the observer differential surface.

Luminance maps are commonly generated using reverse ray tracing (i.e. eye tracing) [Dutré et al., 2006]. Rays are traced from the observer's point of view throughout the optical system of lenses, reflectors, scattering materials, etc. until they intersect with a surface defined as a light source. This approach requires the light source to be defined as a "surface source" having a predefined LID - which in turn means a uniform exitance across the surface source. When a ray finally hits such a surface source, the ray trace is aborted and the assigned LID is sampled. As the surface area of the source is known and a uniform exitance is assumed a luminance value can be calculated by dividing the sampled intensity by the surface area of the source. Accordingly, a luminance value is assigned to the ray. Optical interactions of each ray are stored, and are taken into account to calculate the luminance value of each pixel in the luminance map, represented by a pixelated viewing plane. Simulation time can be shortened significantly by applying importance sampling. When importance sampling is used, more rays will be traced to a specific direction (importance target) when scattering occurs at a surface. During the simulation of luminance distributions this target coincides with the location of the defined surface source. This is a valuable technique because many rays are required to form an accurate image or luminance map on the virtual screen.

For many optical systems, light sources need to be characterized very accurately, both angularly and spatially, especially when they are located in the proximity of other optical components [Kari et al., 2011]. Such an accurate light source representation can be achieved with ray files obtained from near-field goniophotometer measurements. While no standardized file format for ray files is available at the moment [Muschaweck, 2011], ray files traditionally contain a predefined number of rays, each ray typically represented by a starting position, a direction vector, and a luminous flux. Recent research investigated and suggested the incorporation of luminance in ray files [Muschaweck, 2012], however at the moment such ray files cannot be generated directly from near-field goniophotometer measurements. The traditional ray files offer an excellent way of describing light sources when LIDs or illuminance distributions have to be simulated [Joo et al., 2009]. However, they cannot be used directly to simulate a luminance map, as this requires the light source to be modeled through surface sources to allow the sampling of the LID of the light source.

In this chapter we explore the possibility to create luminance maps using forward ray tracing only, thus enabling the creation of luminance maps of luminaire models using ray files as sources and circumventing the issues discussed above. Basically the approach, called a brute force ray tracing technique, consist of tracing a very large number of rays from the source throughout the optical system. Afterwards, only the rays reaching the observer are taken into account to calculate the luminance distribution. The advantages of this approach are two-fold. The method does not require any additional source geometry to be modeled, so no artifacts can be introduced during this stage. Furthermore, once the brute force forward ray tracing is performed, the data offer the possibility to generate luminance maps for any observer's point of view on an interactive basis, eliminating the need to perform a separate ray trace for each point of view. However, to create an accurate luminance map for every possible observer position an enormous amount of rays have to be traced. This is not necessarily a major problem since the simulation can be split into several chunks which can be processed in parallel on different machines.

To be able to compare the results of the brute force ray tracing method to the reverse ray tracing technique, a non-uniform surface source was defined. Luminance maps were then generated using both the brute force ray tracing approach and the conventional reverse ray tracing approach. A good agreement was obtained. A reduction in simulation time was achieved by parallel ray tracing computation and digital enhancement techniques.

2.2 Brute force methodology

The goal of the experiment is to investigate whether it is possible to generate luminance maps using forward ray tracing while maintaining the same quality as the luminance maps found with reverse ray tracing. In order to compare both methods it is necessary to implement the light source as a surface source, even though the final goal is to allow the generation of luminance maps with light sources modeled as ray files.

2.2.1 Preparing the model

In figure 2.1 the geometry of a simulation performed with the reverse ray tracing based luminance module in TracePro® is shown. The luminance distribution on the virtual screen is simulated. To create an equivalent luminance map with forward ray tracing, it is necessary to add a surface with the same dimensions, position and orientation as the virtual screen to the model. This surface, from now on called “ray collecting surface” (RCS), has no optical properties and intersecting rays will not be altered. The data characterizing the rays that intersect the RCS, i.e. intersection position and direction vector will be stored. From this data the luminance map will be constructed. Note that the RCS should be positioned almost directly in front of the source or luminaire. Once the sources and additional surface have been defined the forward ray tracing process can be started.

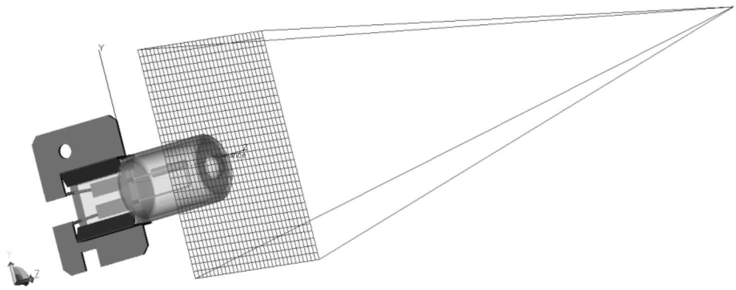

Figure 2.1 – TracePro®'s built-in luminance map module with a virtual screen resolution of 32x32 pixels. The observer plane is oriented parallel with the virtual screen and aligned with the central pixel of the luminance map. The lamp model displayed is an automotive halogen headlamp from the standard TracePro® library.

2.2.2 Data acquisition/selection and luminance map properties

When all rays have been traced from the source(s), an incident ray table (IRT) is generated at the RCS. Since the IRT is a collection of all rays that intersect the RCS some data trimming is required in order to take into account only those rays which actually reach the observer, defined as a circular disc, as shown in figure 2.2.

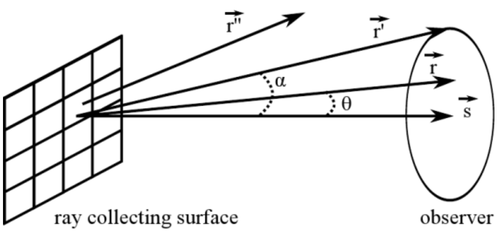

Figure 2.2 – Data selection: only the rays from the IRT for which $\theta < \alpha$ are selected.

In the example given in figure 2.2, only ray $\vec{r}$ is selected, ray $\vec{r}''$ is discarded. This selection is expressed by equation 2.2:

$$\theta = \cos^{-1}\left(\frac{\vec{r}.\vec{s}}{\left\|\vec{r}\right\|\left\|\vec{s}\right\|}\right) < \alpha \qquad (2.2)$$

with: $\vec{s}$ a vector pointing from a pixel of the RCS (part of the source) under study to the center of the observer, $\vec{r}$ the direction vector of the ray and α the angle between $\vec{r}'$ (a direction vector towards the edge of the observer) and $\vec{s}$.

From the selected ray data the luminance map of the ray collecting surface is generated. The RCS is divided into pixels and the total luminance for each pixel is determined in the following way: at each pixel p the individual contribution of a single ray i is defined as:

$$L_{p,i} = \frac{\Delta\Phi_i}{\Delta\Omega_o \Delta A_p \cos\theta_p} \left[\frac{\text{cd}}{\text{m}^2}\right] \tag{2.3}$$

with: $\Delta\Phi_i$ the luminous flux associated with ray i, $\Delta A_p\cos\theta_p$ the apparent surface area of pixel p and $\Delta\Phi_o$ the solid angle subtended by the observer o. The total luminance of each pixel is then defined by equation 2.4.

$$L_p = \sum_i L_{p,i} \tag{2.4}$$

The final image quality will depend on the pixel resolution. It should be noted that in the case of a higher resolution more relevant rays are necessary to build a high quality luminance map. If the resolution is chosen too high for the amount of selected rays, the luminance value found for most pixels will be inaccurate and some pixels will never be intersected by a ray, introducing “dead” pixels.

2.2.3 Digital enhancement techniques

Luminance maps consist of spatially distributed luminance values thus forming an image. The resolution of a luminance map, regardless whether it is measured by a digital luminance camera or constructed from ray tracing data, is determined by a finite number of pixels. In many ray tracing software, digital filters [Gonzalez and Woods, 2002] are commonly implemented to improve the quality of generated images. Two types of digital filters can be used, based on enhancement in either the spatial or frequency domain. In the following section we will briefly discuss four filters from the spatial domain that will be applied to the simulation: an averaging filter, a weighted averaging filter, a selective averaging filter and a selective weighted averaging filter. The latter two are adaptive filter types. All four mentioned filters are commonly used in digital image processing.

Generally speaking a filter in the spatial domain is a transformation T of an image f with MxN pixels to an image g with MxN pixels as expressed in the following equation: $g(x,y) = T[f(x,y)]$. For each of the filters which have a different kernel, with dimensions $M_k \text{x} N_k$ the following equation is applied to generate the filtered image:

$$g(x,y)=\sum_{s=-(M_k-1)/2}^{(M_k-1)/2}\sum_{t=-(N_k-1)/2}^{(N_k-1)/2} w(s,t)\, f(x+s,\, y+t) \qquad (2.5)$$

with: $x = 0,1,...M-1$, $y = 0,1,...N-1$ and $w(s,t)$ the kernel of the filter. Following equation 2.5, each of the filters will calculate a pixel at position (x, y) of the filtered image by taking into account the neighboring pixels in the original image *f*. The size of the kernel also determines the number of pixels that are contributing to every filtered pixel. The simplest kernel is a kernel where each neighboring pixel has the same weight, i.e. an averaging filter. Slightly modifying this kernel gives us the average weighted filter which assigns different weights to different positions in the kernel. Typically this means that pixels located near the central pixel contribute more to the filtered pixel than pixels which are at a larger distance. A 3x3 averaging kernel and a 5x5 weighted averaging kernel are shown in figure 2.3.

$$\frac{1}{9}\begin{pmatrix}1 & 1 & 1\\ 1 & 1 & 1\\ 1 & 1 & 1\end{pmatrix} \qquad \frac{1}{100}\begin{pmatrix}1 & 2 & 4 & 2 & 1\\ 2 & 4 & 8 & 4 & 2\\ 4 & 8 & 16 & 8 & 4\\ 2 & 4 & 8 & 4 & 2\\ 1 & 2 & 4 & 2 & 1\end{pmatrix}$$

Figure 2.3 – Left: kernel of an averaging filter. Right: kernel of a weighted averaging filter.

Both these filters can be used to reduce random noise introduced by random processes such as occurring in ray tracing. However, the blurring of sharp edges could be a disadvantage. A more advanced filter can be constructed by adding a boolean matrix to the kernel. This boolean matrix is constructed according to equation 2.6:

$$B_{x,y} = \begin{cases} 1, \left| f(x+s, y+t) - f(x,y) \right| < \gamma f(x,y) \\ 0, \left| f(x+s, y+t) - f(x,y) \right| \geq \gamma f(x,y) \end{cases} \qquad (2.6)$$

with γ representing the maximum fraction that a pixel *p* can deviate from the selected pixel *s* before the pixel is discarded during the averaging. In practice this means that sharp edges in an image will be retained, as long as the appropriate value is set for γ, while the areas that are more or less uniform will be averaged. The full kernel of a selective weighted averaging filter is shown in figure 2.4, which consist of a scaling factor, a weight matrix *W* and a boolean matrix *B*.

$$\frac{1}{\sum_{s=-(M_k-1)/2}^{(M_k-1)/2}\sum_{t=-(N_k-1)/2}^{(N_k-1)/2}(w_{s,t}.b_{s,t})}\begin{pmatrix}1&2&4&2&1\\2&4&8&4&2\\4&8&16&8&4\\2&4&8&4&2\\1&2&4&2&1\end{pmatrix}*\begin{pmatrix}B_{11}&B_{12}&B_{13}&B_{14}&B_{15}\\B_{21}&B_{22}&B_{23}&B_{24}&B_{25}\\B_{31}&B_{32}&B_{33}&B_{34}&B_{35}\\B_{41}&B_{42}&B_{43}&B_{44}&B_{45}\\B_{51}&B_{52}&B_{53}&B_{54}&B_{55}\end{pmatrix}$$

Figure 2.4 – Kernel of a selective weighted averaging filter composed of a scaling factor, a weight matrix and boolean matrix. Note that $*$ is an element-wise matrix product and $w_{s,t}$ the matrix element on row s and column t.

By replacing the scaling factor and weight matrix in figure 2.4 by the kernel of an averaging filter a selective averaging filter is constructed.

2.3 Experimental validation

2.3.1 Experiment setup

A non-uniform lambertian emitting surface source without any additional optical components such as reflectors or lenses was selected. In figure 2.5 the surface source with the RCS is shown. The source consists of 3 separate ring shaped sources each having a different luminance.

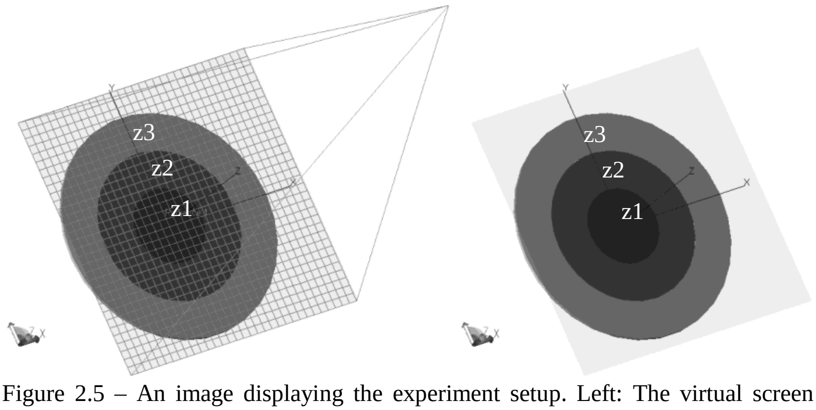

Figure 2.5 – An image displaying the experiment setup. Left: The virtual screen from the reverse ray tracing based luminance map module is shown with a resolution of 32x32 pixels. Right: In the forward ray tracing case the RCS is positioned where the luminance map will be generated.

The RCS is positioned similar to the virtual screen from the existing software module. The observer is oriented parallel with the virtual screen and aligned with the central pixel of the luminance map at a distance of 150mm, the size of the virtual screen is 70mm x 70mm.

The total luminous flux emitted by the source is set at 600 lumen. In each ray tracing run 50 000 000 rays are traced. The rays are distributed over the 3 zones (z1, z2 and z3) in such a way that the ray density per luminous flux is constant, thus ensuring that sufficient rays are assigned to each zone, even to a zone having a low luminous flux. These constraints are expressed in equations 2.7 and 2.8. The number of rays originating in each zone is determined from these expressions, as illustrated in table 2.1.

$$\#rays_{z1} + \#rays_{z2} + \#rays_{z3} = 5.10^{7} \tag{2.7}$$

$$\frac{\#rays_{z1}}{\Phi_{z1} A_{z1}} = \frac{\#rays_{z2}}{\Phi_{z2} A_{z2}} = \frac{\#rays_{z3}}{\Phi_{z3} A_{z3}} \tag{2.8}$$

with Φ_{zi} and A_{zi} respectively the luminous flux and surface area of zone *i* and $\#rays_{zi}$ the number of rays assigned to zone *i*.

Table 2.1: Ray distribution across surface sources 1,2 and 3 as calculated by equations 4.5 and 4.6

	Φ_{zi} **[lm]**	A_{zi} **[m²]**	$\#rays_{zi}$
Zone 1	300	0.0003	10 714 286
Zone 2	200	0.0009	21 428 571
Zone 3	100	0.0016	17 857 143

As the sources are lambertian emitters, the relation between the luminance and luminous flux of each zone i can be calculated as:

$$L_i = \frac{\Phi_{zi}}{\pi A_{zi}} \left[\frac{\text{cd}}{\text{m}^2} \right] \tag{2.9}$$

Applying equation 2.9 to each zone yields: $L_1 = 303\,964\,\text{cd/m}^2$, $L_2 = 67\,547\,\text{cd/m}^2$ and $L_3 = 20\,264\,\text{cd/m}^2$. The ray tracing experiment is set up in such a way that several simulations are performed in parallel on different machines in order to keep the run time as short as possible. In this experiment, 28 runs (50 000 000 rays per run) were performed, with a total number of rays of 1 400 000 000. Note, that for each ray tracing session, a different seed has to be assigned to the random number generator of the ray tracer, in order to assure that each run uses a unique set of rays. For each session an IRT for the ray collecting surface is calculated. These incident ray tables are then combined into one. Note that the luminous flux carried by each ray has to be divided by the number of seeds.

2.3.2 Data processing

The first step in the data processing stage is the removal of rays which are not contributing to the luminance map by applying equation 2.2. In this experiment we set $\alpha = 1.5°$. By adjusting the plane half angle α as defined in figure 2.2, the solid angle by which rays are selected can be changed. The higher the value of α the more rays that will contribute to the luminance map. After the selection stage, the contributing rays are sorted per pixel. The resolution of the luminance maps is set at 32x32 or at 128x128. Equation 2.4 is applied and the luminance value for each pixel is calculated. If a sufficient number of rays is traced, the luminance map should be identical to the one found using reverse ray tracing.

In figure 2.6 the luminance map generated by the commercial reverse ray tracing module is shown. As expected the luminance values in each zone are uniform except at the edges of a zone. This is because a pixel can be located on top of the boundary between two zones and a mean luminance value is found. A cross section of the luminance map was created to examine the absolute luminance values and transitions from one zone to another, this is shown in figure 2.7. The absolute luminance values correspond to the theoretical luminance values calculated by equation 2.9. The width of the transition region between zones is determined by the resolution of the luminance map; a higher resolution will result in sharper transitions.

Figure 2.6 – Left: Normalized luminance map generated with the reverse ray tracing module from TracePro® (resolution: 128x128 pixels). Right: Magnified part of the luminance map.

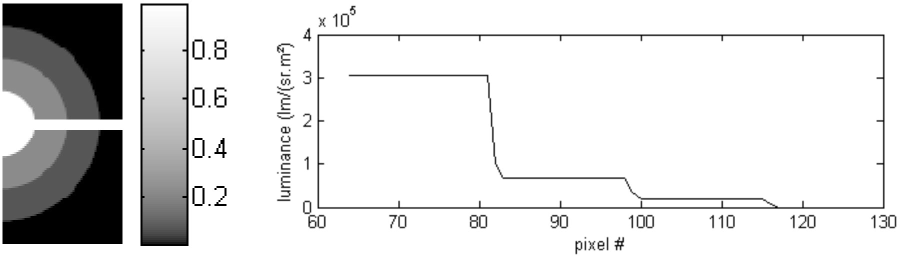

Figure 2.7 –Left: The horizontal cross section represented by the white line drawn onto the luminance map. Right: The cross section of the simulated luminance map.

The luminance maps generated with the brute force forward ray tracing technique are shown in figure 2.8 and 2.9 for a resolution of 128x128 and 32x32 pixels respectively. As can be seen these luminance maps are not entirely identical. It is clear that a lower resolution gives rise to a less resolved yet more uniform luminance map because more rays will be binned into one pixel. Note that for both luminance maps slightly different values are found for adjacent pixels within one zone; which in theory should all have the same luminance value.

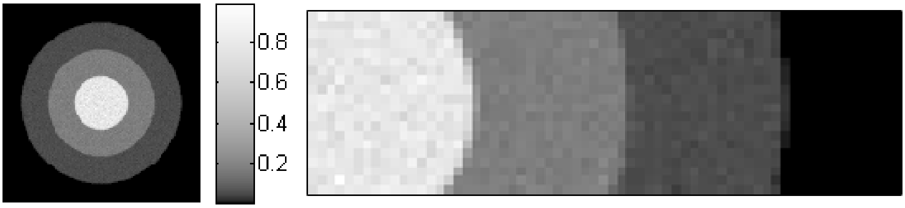

Figure 2.8 – Left: Normalized luminance map generated using brute force forward ray tracing ($\alpha = 1.5°$, resolution: 128x128 pixels). Right: Magnified part of the luminance map.

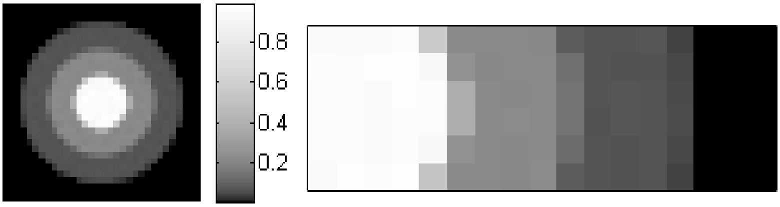

Figure 2.9 – Left: Normalized luminance map generated using brute force forward ray tracing ($\alpha = 1.5°$, resolution: 32x32 pixels). Right: Magnified part of the luminance map.

The effect of running the forward ray tracing simulation multiple times with different seeds is shown in figure 2.10. The use of more rays clearly results in an improved correspondence with the target luminance values.

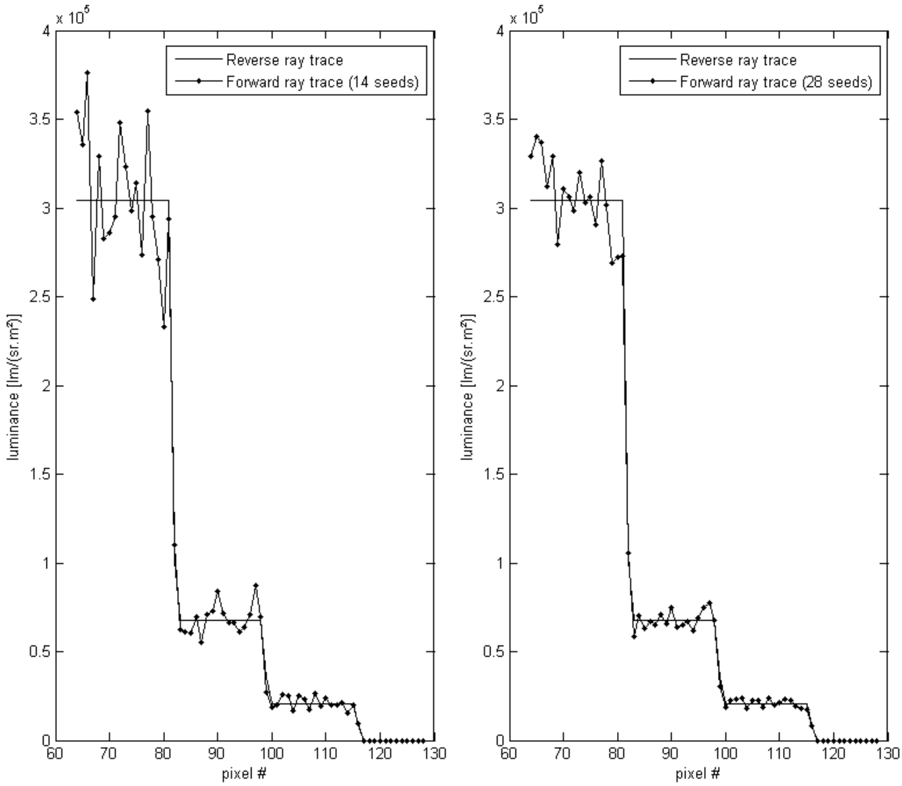

Figure 2.10 – Cross section of the luminance map ($\alpha = 1.5°$, resolution: 128x128 pixels) with 14 seeds = 700 000 000 rays (left) and 28 seeds = 1 400 000 000 rays (right).

2.3.3 Applying digital enhancement techniques

To improve the generated luminance maps, the filters discussed in section 2.2.2 were applied. The same cross sections as presented in figure 2.10 are shown in figure 2.11 after applying the digital filters. When applying the averaging 5x5 filter, more uniformity is created but sharp edges are blurred. A weighted averaging filter as presented in figure 2.3, performs slightly better at the edges but blurring still occurs. The selective averaging filter, incorporating a boolean matrix with $\gamma = 0.2$ and a mask where each pixel has the same weight, brings more uniformity and causes less blurring at the sharp edges. Setting the γ value at 0.2 causes pixels with luminance values that differ less than 20% from the current pixel to be discarded. This is an acceptable percentage as the luminance values change drastically from one zone to another. A selective weighted averaging filter ($\gamma = 0.2$) was also applied. However, this resulted in less uniformity in the areas with a predefined constant luminance.

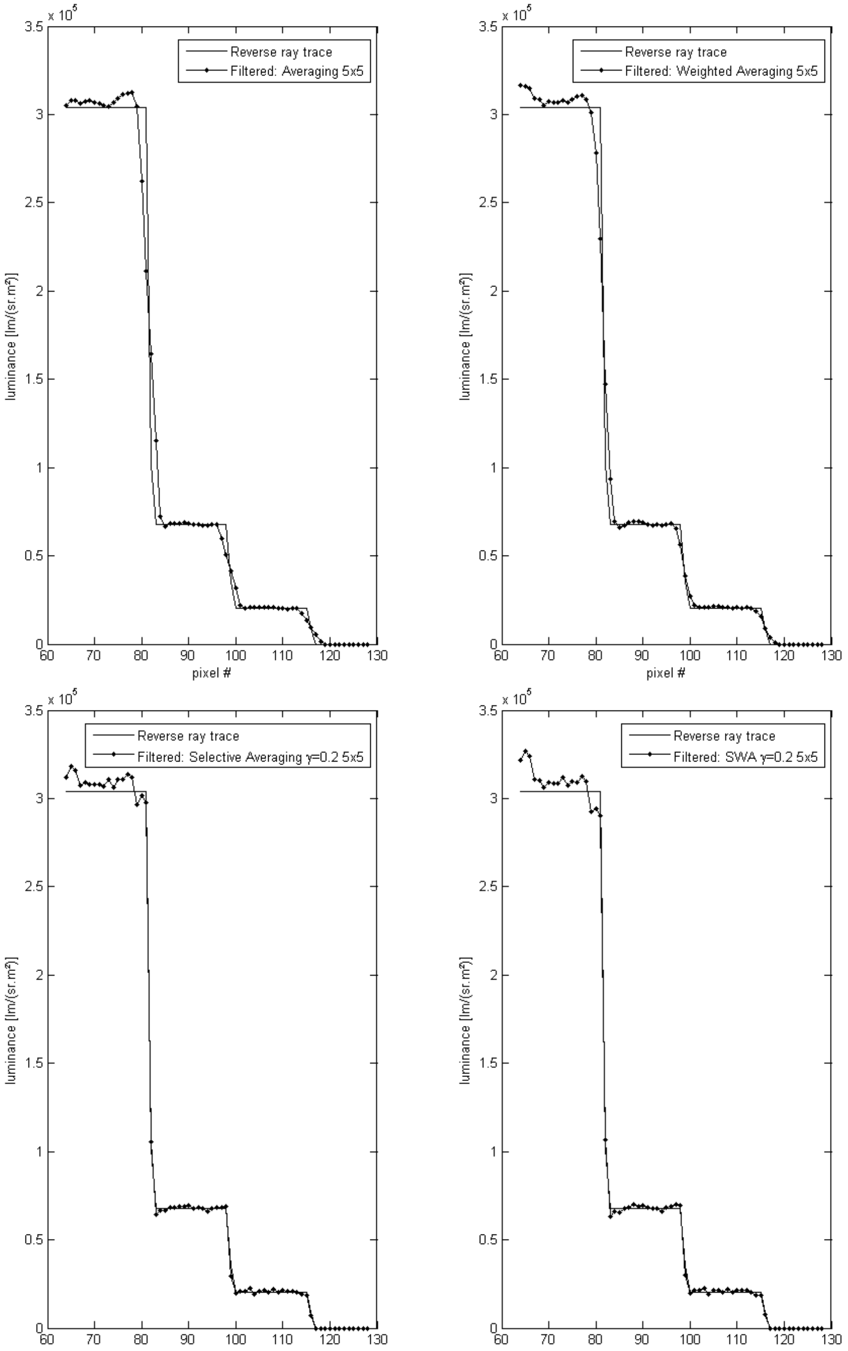

Figure 2.11 – Applying digital enhancement filters to luminance maps obtained with the brute force ray tracing technique. Cross sections of the maps for several filters are shown: averaging 5x5 filter (top left), weighted averaging 5x5 filter (top right), selective averaging $\gamma = 0.2$ - 5x5 filter (bottom left) and selective weighted averaging $\gamma = 0.2$ - 5x5 filter (bottom right).

In this experiment the best results are obtained using a selective averaging filter. It introduces uniformity in the regions predicted by the commercial reverse ray tracing module while conserving the sharp edges in the image. However, luminance maps of real world luminaires may have a completely different structure. It is expected that when no large areas of constant luminance are present a selective weighted averaging filter is more appropriate.

2.4 Conclusions

In this chapter a feasibility study of a brute-force forward ray tracing approach to generate luminance distributions of ray files is presented.

A simple light source model constructed of one circular and two ring shaped lambertian emitters with different luminance was used as test source. A good agreement was found between the forward and reverse ray tracing techniques when digital enhancement techniques in the spatial domain were applied. However, a large amount of rays are necessary to obtain a good correspondence. If the approach would be used in real world simulations of luminaires, then each time the geometry or optical properties of the luminaire are changed during the virtual prototyping stage a new ray trace and corresponding ray collecting surface has to be made in order to generate the luminance maps. This, in combination with the large amount of rays that need to be traced, makes the approach quite cumbersome to use.

On the other hand, the forward ray tracing approach exhibits some advantages over the traditional reverse ray tracing techniques implemented in commercial ray tracing software packages. Indeed, the forward approach offers the possibility to generate luminance maps for optical systems including sources modeled as ray files. Furthermore, once the entire forward ray tracing process has been completed, luminance distributions can be generated for any observer position on an interactive basis.

A more suitable approach would be to construct a surface source model from the ray file data which in turn can be sampled by tracing rays from the observers position towards the light source (i.e. reverse ray tracing). This could be achieved by adding an additional surface that envelops the starting positions of all rays in the ray file. This surface can then be divided into smaller surfaces each having a different luminous intensity distribution based on the direction of the rays that intersect this surface. In this way the original source, modeled by the ray file, could be approximated by a multitude of non-physical surface sources. This would allow luminance maps to be simulated by the standard reverse ray tracing technique. Such models are discussed in chapter 3.

Chapter 3

Simulating luminance distributions from ray files through sampling and geometric modeling

3.1 Introduction

In chapter 2 we presented a brute-force ray tracing approach which was able to generate quite accurate luminance distributions of a light source modeled by a ray file. A large amount of rays in combination with digital enhancement filters however had to be used to reach an adequate result. To overcome these drawbacks, a method to sample the ray file to allow the use of reverse ray tracing is presented in this chapter.

An interesting approach described in literature is to generate a multitude of point sources each with a specified LID by sampling the ray file [Mas et al., 2008]. Triangular meshes can be defined, with each vertex of the mesh having a particular LID. An important limitation of this method is that off-the-shelf available ray tracers are not capable of sampling the triangular meshes as an interpolation between the LIDs of the vertices is not supported [Mas et al., 2008]. Furthermore, while this method yields good results when simulating illuminance distributions, it is not investigated whether the method can accurately predict luminance maps.

In this chapter, another method of sampling a ray file is presented. The method can be used in conjunction with any optical ray tracing software without the need to adapt the ray tracer algorithms as long as the ray tracer supports surface sources which are defined through a LID. To validate the presented sampling method, near-field goniophotometer measurements of two planar light sources were performed. From these measurement data, ray files were extracted and the sampling method was applied in order to obtain a set of surface sources. This approach was validated by comparing measured luminance images with simulated luminance images. Afterwards, the method is altered to accommodate for hemispherically shaped light sources. A good agreement was found, validating the presented method.

3.2 Planar light sources

3.2.1 Introduction

A planar light source with a lambertian LID and a planar light source with a more complex asymmetric LID have been chosen as test sources. At first, the near-field light distribution of both sources is measured with a near-field goniophotometer. From these data, ray files are extracted, which in turn are sampled according to the method as described in section 3.2.2, resulting in a set of LIDs. These LIDs are imported in TracePro® and assigned to surfaces, creating a set of surface sources. Luminance maps of both light sources as seen from different viewing angles are simulated and compared with experimental luminance distributions. In both cases, an excellent agreement is found between the simulated and measured luminance distributions.

3.2.2 Methodology

The near-field measurements are performed with a commercial near-field goniophotometer from TechnoTeam - (RiGo801 for small light sources with a diameter < 30mm), as described in chapter 1. A maximum of 10^9 rays can be generated from near-field data measured with this device. The center and the light emitting surface of the light source under investigation are aligned respectively with the origin of the coordinate system XYZ and the XY plane of the near-field goniophotometer.

The following algorithm is performed to generate a set of surface sources by sampling the ray file of a planar light source.

1. Generate a ray file from the measured near-field data with the maximum number of rays (10^9). Determine the starting position (x_r,y_r,z_r) of each ray by finding the intersection of each ray direction $\mathbf{d}(a,b,c)$ and a user defined bounding surface from which all rays should start. The user defined bounding surface is assumed to be a planar surface located in the XY plane. The direction $\mathbf{d}$ and luminous flux Φ_r of each ray are determined by the near-field goniophotometer measurement.

2. Divide the bounding surface into equal area square pixels P(i,j) with a resolution Δd.

3. Select each ray and determine the pixel P(i,j) from which this ray originates by evaluating the start position of the ray (i.e. (x_r,y_r,z_r)). Add the luminous flux of the ray to the pixel flux $\Phi_{P(i,j)}$.

4. Calculate a luminous intensity distribution (LID) for each pixel P(i,j) as follows:
   a. For each ray emitted from P(i,j), calculate the spherical angles (θ_r,φ_r), with θ_r the polar angle between $\mathbf{d}(a,b,c)$ and the surface normal (Z-axis) and φ_r the azimuthal angle between $\mathbf{d}(a,b,0)$ and the X-axis.

   b. Create bins $B_{\theta,\varphi}$ according to a specified $\Delta\theta$ and $\Delta\varphi$. For the first iteration, set $\Delta\theta$ to 30° and $\Delta\varphi$ to 90°. The $\Delta\theta$=30° setting results in 4 bins for the polar direction with central directions 0°, 30°, 60° and 82.5° for the range R_θ = [0°,15°[, [15°,45°[, [45°,75°[and [75°,90°[, respectively. The $\Delta\varphi$=90° setting results in 4 bins with a central direction of φ = 0°, 90°, 180° and 270°, for the range R_φ = [-45°,45°[, [45°,135°[, [135°,225°[and [225°,-45°[, respectively. A graphical representation of the angular binning is shown in figure 3.1.

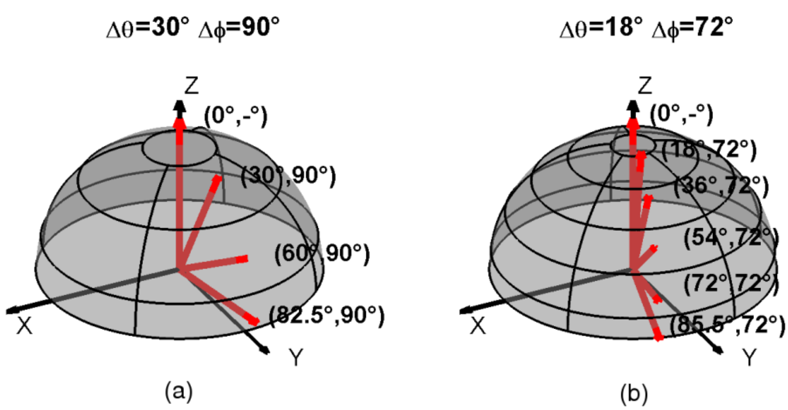

Figure 3.1 – Representation of the angular binning in the XYZ coordinate system consisting of bin boundaries (solid lines) and central bin directions (red lines). (a) angular binning during the first iteration for which $\Delta\theta$ equals 30° and $\Delta\varphi$ equals 90°. (b) angular binning during the second iteration, after step 4.h, for which $\Delta\theta$ equals 18° and $\Delta\varphi$ equals 72°.

   c. Calculate the solid angle $\Omega_{B_{\theta,\varphi}}$ [sr] for each bin $B_{\theta,\varphi}$ as expressed by equation 3.1:

$$\Omega_{B_{\theta,\varphi}} = \Delta\varphi \cdot \left[\cos(\min\left[R_\theta\right]) - \cos(\max\left[R_\theta\right])\right] \tag{3.1}$$

d. Evaluate the angles θ_r and φ_r for each ray emitted from pixel P(i,j) and add the flux of the ray, Φ_r, to the flux of the respective bin $B_{\theta,\varphi}$ resulting in the total flux $\Phi_{B_{\theta,\varphi}}$.

e. Calculate the intensities $I_{\theta,\varphi}$ emitted towards the central directions of each bin $B_{\theta,\varphi}$ as $I_{\theta,\varphi} = \Phi_{B_{\theta,\varphi}} / \Omega_{B_{\theta,\varphi}}$ [lm/sr]. Pad with a 0 intensity for direction θ=90°.

f. Integrate the intensity distribution towards a luminous flux $\Phi_{\mathrm{Int,P}(i,j)}$ [lm] as expressed by equation 3.2:

$$\Phi_{\mathrm{Int,P}(i,j)} = \sum_{\theta(k)}\sum_{\varphi(l)} \frac{I_{\theta(k),\varphi(l)} + I_{\theta(k+1),\varphi(l)}}{2} \left[\cos(\theta(k)) - \cos(\theta(k+1))\right]\Delta\varphi \quad (3.2)$$

g. Calculate the percentage error E[%], between $\Phi_{\mathrm{P}(i,j)}$ and $\Phi_{\mathrm{Int,P}(i,j)}$ expressed by equation 3.3:

$$E = \frac{\left|\Phi_{\mathrm{Int,P}(i,j)} - \Phi_{\mathrm{P}(i,j)}\right|}{\Phi_{\mathrm{P}(i,j)}} \quad (3.3)$$

h. If the percentage error is larger than a predefined threshold go back to step 4.b while decreasing the values for $\Delta\theta$ and $\Delta\varphi$ with 1°. Care should be taken that the adjusted $\Delta\theta$ and $\Delta\varphi$ values result in an integer number of bins. Repeat this until either the predefined threshold or a predefined minimum value for $\Delta\theta$ and $\Delta\varphi$ is reached. A minimum value of 1° for both $\Delta\theta$ and $\Delta\varphi$ is used resulting in a maximum number of bins of 360x90 = 32 400. The angular binning during the first iteration and second iteration is displayed in figure 3.1 (a) and figure 3.1 (b), respectively.

i. Write the calculated intensity distribution for each pixel to a file which can be imported and interpreted by the ray tracer. A local x-axis which corresponds with the C0 plane of the LID is aligned with the global X-axis of the ray tracer and defined for each pixel. By defining such a local x-axis, the asymmetric LIDs can be sampled correctly when rays are traced from the observer point of view towards each surface source.

A flowchart of the presented algorithm is shown in figure 3.2.

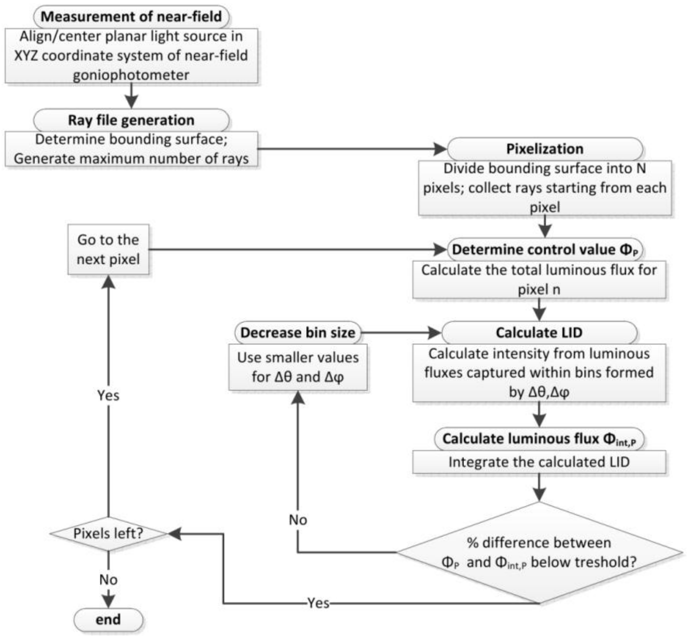

Figure 3.2 – Flowchart of the algorithm used to measure, process and sample a ray file of a planar light source into a set of surface sources.

A gridded (θ,φ) parameterization was chosen to determine the intensity distribution of each pixel/surface source. Other parameterization schemes such as non-gridded parameterization, geodesic dome parameterizations, etc. could be integrated in the presented algorithm. However, the commercial ray tracer used to validate our approach only accepts intensity distributions with a gridded (θ,φ) parameterization. This parameterization method was kept flexible, through the use of the percentage error parameter in order to make sure that the sampled radiation distributions are accurate while limiting the amount of information that needs to be stored. For example, it was observed that a lambertian pattern could easily be modeled with very few (θ,φ) parameters while a highly peaked radiation pattern required more (θ,φ) parameters in order to capture the subtle differences.

3.2.3 Experimental validation

To validate the presented method, two practical examples are discussed. In both cases, a remote phosphor LED module (RPLED) [Hoelen et al., 2008; Xicato, 2013], i.e., a light source with lambertian emission, is selected. This source emits light from a circular planar area with diameter 23 mm. The first practical example consist of only the naked RPLED which exhibits a symmetrical (lambertian) radiation pattern. The second practical example is created by adding a brightness enhancement film (BEF) on top of the remote phosphor plate, resulting in an asymmetric radiation pattern emitted by the source.

3.2.3.1 Example 1: symmetric planar light source

First, the near-field light distribution of the RPLED is measured with a near-field goniophotometer (RiGo801), by moving the camera and the photometer to various points on an imaginary hemisphere with an angular resolution of 0.5° for both the polar and azimuthal direction. This measurement results in a .ttr file, which is a proprietary file format from the manufacturer. A ray file containing the maximum amount of rays that can be generated (10^9) is created from this .ttr file. Less rays could be used as input for the sampling algorithm, however this would also mean that less information is available and as such the subsequently generated luminance distributions would also become less accurate.

Next, this ray file is processed and sampled with Matlab according to the presented algorithm. The spatial resolution of the square pixels in which the ray file is divided, is set to 1 mm. As a result, 437 luminous intensity distributions are created. Less LIDs are created than expected (23^2=529), as pixels where no rays originate from are not taken into account. The total required disk space for these 437 LIDs is around 30MB, i.e., only 1/830 of the disk space required for the original ray file. These LIDs are imported in TracePro® and applied to square surfaces with a width and length of 1 mm.

Luminance maps, each calculated from a different observer position, are simulated by tracing rays starting from the viewpoint of the observer towards the set of surface sources. Each luminance map has a width and length equal to 23 mm and is divided into pixels with a width and length of 1 mm. For each pixel in the luminance map, 10^3 rays are traced. The observer position is expressed in spherical coordinates (θ_o,φ_o), while the distance between the observer and center surface remains 1 000 mm. In total, 4 luminance maps for an observer position of (θ_o,φ_o)=(0°,0°), (θ_o,φ_o)=(30°,0°), (θ_o,φ_o)=(60°,0°) and (θ_o,φ_o)=(80°,0°) are simulated; φ_o is equal for all observer positions as the light source emits symmetrical. For each of these positions, a luminance map is also measured with the luminance camera of the near-field goniophotometer. To allow for a visual comparison between the measured and simulated luminance maps, the spatial resolution of the experimental luminance map is set to be the same as the resolution of the simulated luminance map.

The results are shown in figure 3.3, including a figure presenting a percentage difference image, *Diff*, calculated as:

$$Diff = \left| L_s - L_m \right| \cdot \left(\frac{2}{L_s + L_m} \right) \cdot 100 \tag{3.4}$$

with L_m and L_s the luminance value of each pixel in the measured and simulated luminance distribution respectively.

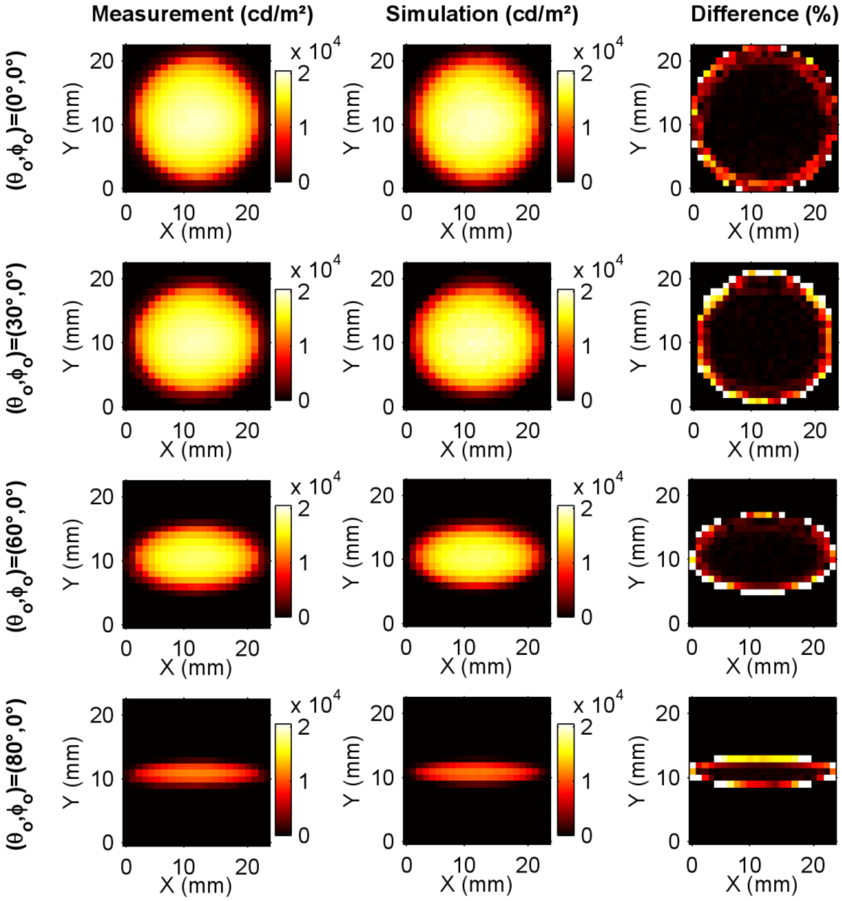

Figure 3.3 – Comparison between the measured (left column) and simulated (middle column) luminance maps for the observer positions: (θ_o,φ_o)=(0°,0°), (θ_o,φ_o)=(30°,0°), (θ_o,φ_o)=(60°,0°) and (θ_o,φ_o)=(80°,0°) of an RPLED module. Right column: percentage difference images between the measured and simulated luminance maps.

As can be seen, a very good agreement is found. The larger differences at the edges of the light source originate from pixel discretization and small mismatches between the alignment of the light source during the measurement of the luminance map and the measurement of the ray file. Another reason for these differences is found in the original ray file where fewer rays start from the outer edge of the source compared to the central area. As a result the ray file will be less accurate for pixels located at the outer edge.

Apart from a visual assessment of the quality of the simulated luminance maps, the differences between simulated and measured luminance distributions are quantified by calculating both the normalized cross correlation ratio (NCC) [Lewis, 1995], a method for template matching, and the normalized root-mean-squared error (NRMSE) between the measured and simulated luminance maps. The NCC and NRMSE are defined by equation 3.5 and 3.6, respectively:

$$NCC = \frac{\sum_{X,Y}\left[(L_m(X,Y)-\overline{L}_m)(L_s(X,Y)-\overline{L}_s)\right]}{\left[\sum_{X,Y}(L_m(X,Y)-\overline{L}_m)^2\sum_{X,Y}(L_s(X,Y)-\overline{L}_s)^2\right]^{1/2}} \tag{3.5}$$

$$NRMSE = \frac{\sum_{X,Y}\sqrt{\left[L_s(X,Y)-L_m(X,Y)\right]^2}}{\max(L_s,L_m)N} \tag{3.6}$$

with $\overline{L}_m$ and $\overline{L}_s$ the mean values of the respective luminance map, X and Y the pixel coordinates and N the number of pixels of the luminance map. The NCC value can range from 0 to 100%, with 0% meaning no correlation at all, while 100% implying a perfect match between the relative shape of the luminance maps. Note that this value only gives a measure of similarity [Gesù and Starovoitov, 1999]. Therefore, it is necessary to calculate both the NCC value and the NRMSE value, as the latter takes into account the absolute differences of the luminance maps. The calculated NCC and NRMSE values for each observer position are presented in table 3.1.

Table 3.1: Comparison between the simulated and measured luminance maps of the RPLED. Normalized cross correlation ratio (NCC) and normalized root-mean-squared error (NRMSE) calculated for different observer positions.

Observer position (θ_o,φ_o)	**NCC(%)**	**NRMS(%)**
(0°, 0°)	99.7	2.8
(30°, 0°)	99.6	3.5
(60°, 0°)	99.7	2.8
(80°, 0°)	99.3	3.1

As expected from the visual comparison of the luminance maps, an excellent agreement is found as the NCC values are larger than 99% while the NRMSE values are low. To put the differences at the outer edge in perspective, a horizontal cross section of the simulated and measured luminance map for an observer position of (θ_o,φ_o)=(0°,0°) at Y = 11 mm is shown in figure 3.4. Here the differences at the edges appear to be very low in comparison to the maximum luminance values obtained in the center near X = 12 mm.

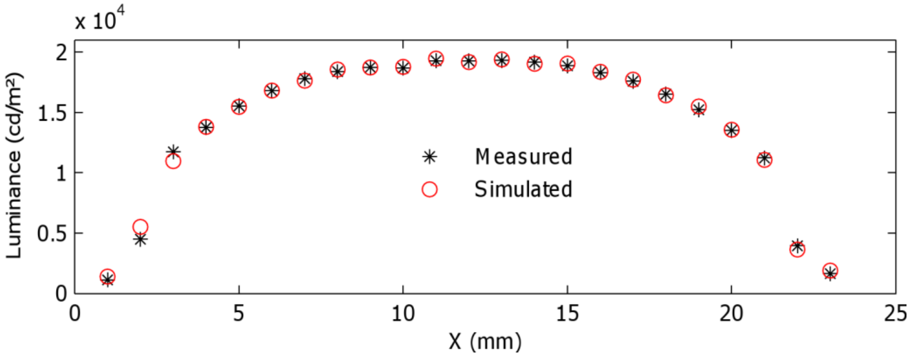

Figure 3.4 – Horizontal cross section for (θ_o,φ_o)=(0°,0°) at Y = 11 mm for the measured (star) and simulated (circle) luminance map of the RPLED.

3.2.3.2 Example 2: asymmetric planar light source

To verify that the presented method also works for individual asymmetric surface sources, a brightness enhancement film (BEF) [3M, 2013] with a thickness of 1 mm was added on top of the remote phosphor plate of the RPLED module. This film consists of a linear prismatic structure which reflects and refracts incident light to enhance the light output within a specific viewing cone, a technique often used in LCD backlights. Again, the near-field of the RPLED module, now in combination with the brightness enhancement film, was measured with the near-field goniophotometer. A ray file was generated from the measured data and processed/sampled according to the presented method using the same settings (pixel resolution = 1 mm). Luminance maps are simulated for the same observer positions as in the first case, but in addition luminance maps are also simulated for the observer positions (θ_o,φ_o)=(0°,90°), (θ_o,φ_o)=(30°,90°), (θ_o,φ_o)=(60°,90°) and (θ_o,φ_o)=(80°,90°). Luminance maps for these observer positions are also experimentally determined with the near-field goniophotometer, and compared with the simulated luminance maps through percentage difference images. The results are shown in figure 3.5 and figure 3.6 for the observer positioned at a 0° and 90° azimuthal direction, respectively.

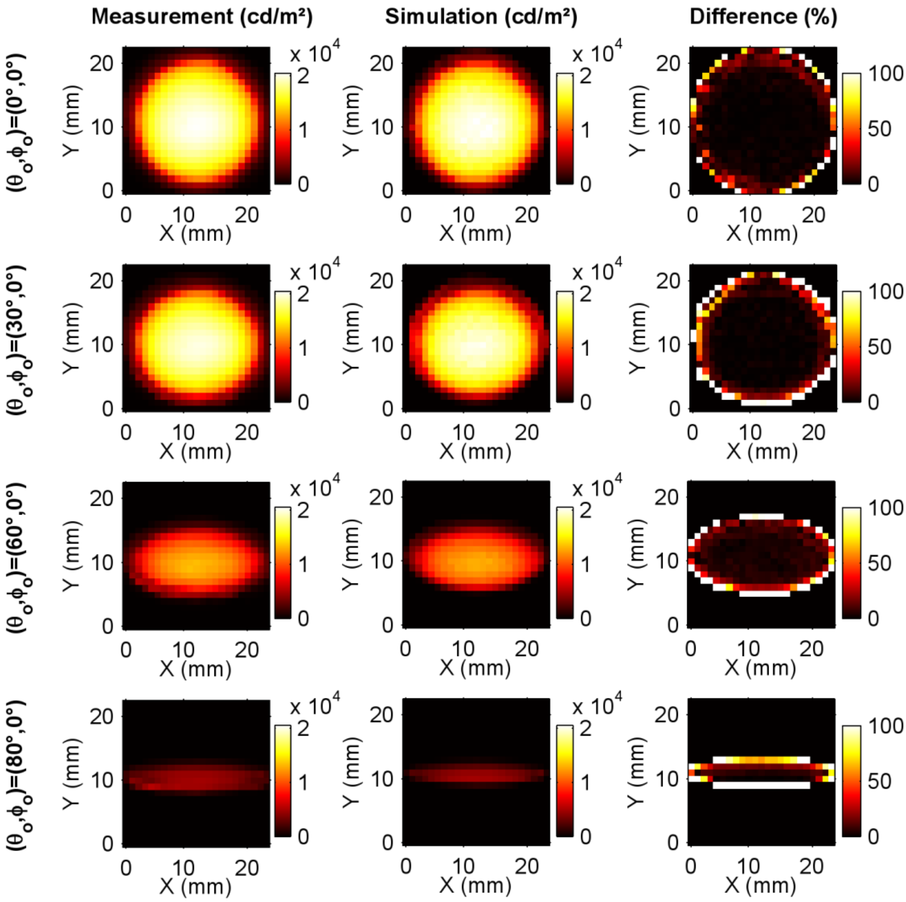

Figure 3.5 – Comparison between the measured (left column) and simulated (middle column) luminance maps for the observer positions: (θ_o,φ_o)=(0°,0°), (θ_o,φ_o)=(30°,0°), (θ_o,φ_o)=(60°,0°) and (θ_o,φ_o)=(80°,0°) of an RPLED module in combination with a BEF. Right column: percentage difference images between the measured and simulated luminance maps.

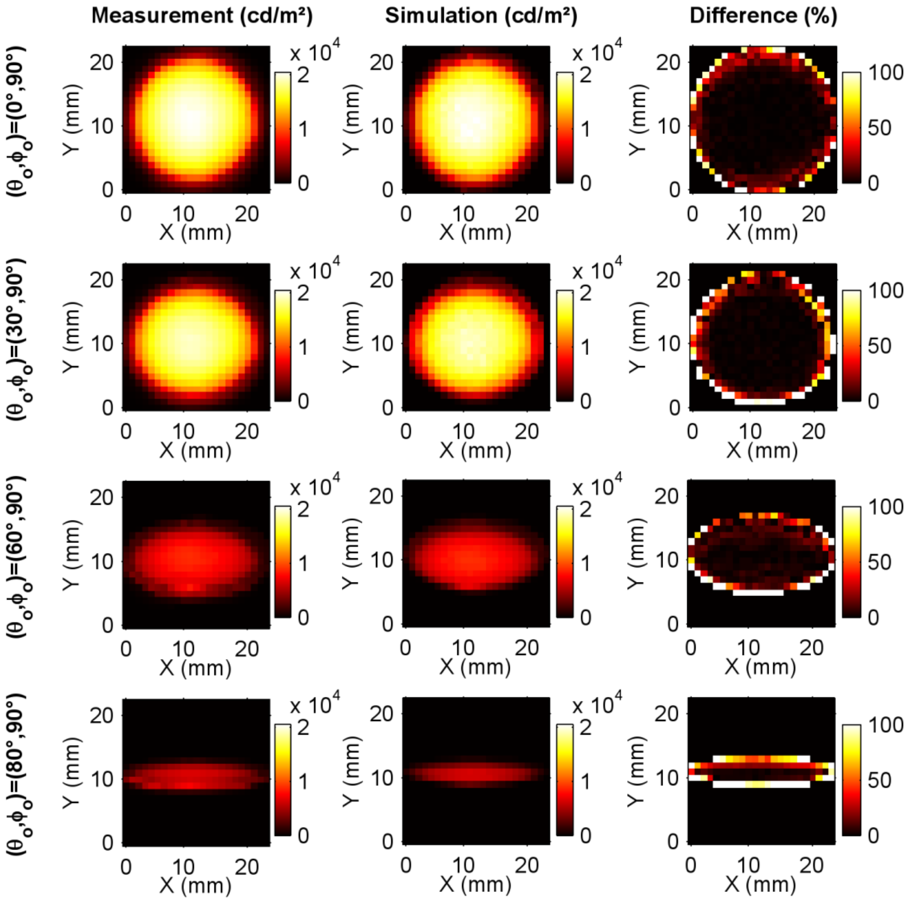

Figure 3.6 – Comparison between the measured (left column) and simulated (middle column) luminance maps for the observer positions: (θ_o,φ_o)=(0°,90°), (θ_o,φ_o)=(30°,90°), (θ_o,φ_o)=(60°,90°) and (θ_o,φ_o)=(80°,90°) of an RPLED module in combination with a BEF. Right column: percentage difference images between the measured and simulated luminance maps.

A good agreement between measured and simulated luminance maps is again found for almost all observer positions. However, from these figures, the effect of the brightness enhancement film is not clearly visible. The cross section of the luminance map for an observer position (θ_o,φ_o)=(60°,0°) and for an observer position (θ_o,φ_o)=(60°,90°), as shown in figure 3.7, clearly illustrates the impact of the film.

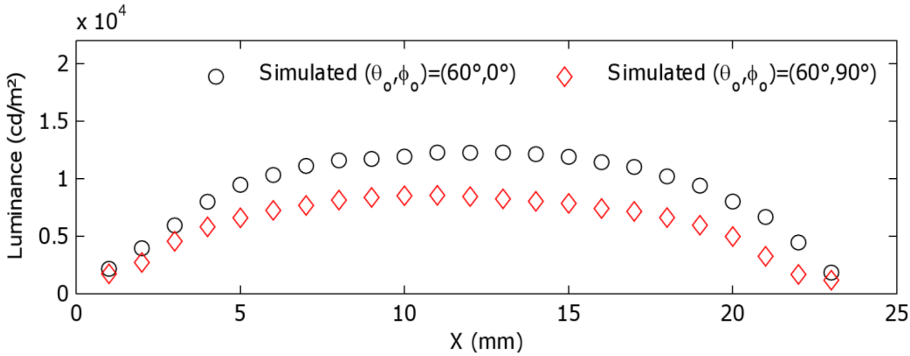

Figure 3.7 – Comparison of a horizontal cross-section of the simulated luminance map for the observer positions (θ_o,φ_o)=(60°,0°) and (θ_o,φ_o)=(60°,90°) of an RPLED module in combination with a BEF.

NCC and NRMSE values are calculated for each observer position and presented in table 3.2. The agreement for observers at large polar angles (near grazing) is clearly not as good compared to the results obtained without applying the BEF (table 3.1). The reason for this mismatch between simulated and measured luminance images for near grazing angles is due to the fact that the side surfaces of the 1 mm thick brightness enhancement film also emits light – an effect which is not included in the simulations as the light source is modeled as a planar source.

Table 3.2. Comparison between the simulated and measured luminance maps of the RPLED with BEF. Normalized cross correlation ratio (NCC) and normalized root-mean-squared error (NRMSE) calculated for different observer positions.

	Δ*d* = 1 mm		**Δ*d* = 0.5 mm**	
Observer position (θ_o,φ_o)	***NCC (%)***	***NRMSE (%)***	***NCC (%)***	***NRMSE (%)***
(0°, 0°)	99.8	2.3	99.6	3.3
(30°, 0°)	99.3	4.3	99	5.1
(60°, 0°)	98.5	6.3	98	6.9
(80°, 0°)	86.8	12.5	76.5	11.9
(0°, 90°)	99.8	2.7	99.5	3.6
(30°, 90°)	99.4	4.1	99.1	5
(60°, 90°)	97.7	7.4	96.7	8
(80°, 90°)	89.1	11.2	84.4	12.3

Due to the structured surface created by the BEF, it can be interesting to investigate the effect of the use of smaller surface sources. Surface sources with a resolution of Δd = 0.5 mm are generated from the ray file. Similarly, luminance maps are simulated for the various observer positions and compared with the measured luminance maps, resulting in a second set of NCC and NRMSE values as displayed in table 3.2.

In analogy with the visual comparison, the NCC and NRMSE values indicate again a good agreement between the simulated and measured luminance maps, but the NCC and NRMSE values for the observer positions $(\theta_o,\varphi_o)=(80°,0°)$ and $(\theta_o,\varphi_o)=(80°,90°)$ are again worse than for the other observer positions, but are still acceptable. Surprisingly, the NCC and NRMSE values for these grazing angles become lower respectively higher when changing the resolution of the individual surface sources from 1 mm to 0.5 mm. Indeed, as the size of the surface sources becomes smaller, the luminance values are averaged out over a smaller area. This results in a higher detail but consequently the mismatches at the sides of the brightness enhancement film become more and more important.

3.2.4 Predefined threshold

Finally, the sampling requirements of the presented algorithm are investigated. While the pixel size determines the spatial sampling, the predefined threshold, as described in the algorithm in step 4.h, controls the angular sampling. The influence of the latter on the overall model quality of the light source is investigated. To this end, several models of both the RPLED and RPLED with BEF are created with different predefined thresholds. One could now simulate several luminance distributions and compare these to measured luminance distributions. However, this approach is impractical as this would need to be done for every possible observer position. Instead, the analysis of the overall quality of the model of the light source is performed on the complete LID emitted by the model. As such, each surface source is attributed a number of rays in order to generate a total of 10^6 forward rays, while the number of rays attributed to each surface source is weighted with the emitted luminous flux of the surface source in question to the total emitted luminous flux of the whole model. Next, a ray file, also containing 10^6 rays, is generated from the original proprietary .ttr file. LIDs of each model and the ray file are simulated and compared by evaluating the NCC and NRMSE values which can be calculated by replacing the spatial coordinates and corresponding luminance values of equation 3.5 and equation 3.6 with spherical coordinates and corresponding intensity values [Chien et al., 2007; Sun et al, 2006] respectively. The results are displayed in figure 3.8 and figure 3.9.

In both figures, a large predefined threshold causes little or no change in the overall quality of the model. As the threshold becomes lower, more bins will be needed to accurately describe each LID of a pixel, and as such specific characteristics of the LID can be captured and the overall quality of the model improves (i.e. lower NRMSE and higher NCC values). However, as the predefined threshold becomes even smaller the overall quality decreases as overfitting of the LIDs occurs. This overfitting results from the lack of rays in a single bin. The optimal predefined threshold is located where the NCC and NRMSE reach a maximum and minimum, respectively. These are however not global maxima and minima, but rather one should look for a maximum NCC and a NRMSE which is clearly lower than the NRMSE for other predefined thresholds. For the RPLED and RPLED with a BEF, this point is located at 2.1% and 0.021%, respectively. As the RPLED with a BEF is less symmetric compared to the RPLED, a lower predefined threshold and as a consequence more angular bins are needed to accurately characterize the light source. A similar method can also be used to investigate the spatial sampling requirements in order to find the optimal spatial binning (i.e. pixel resolution).

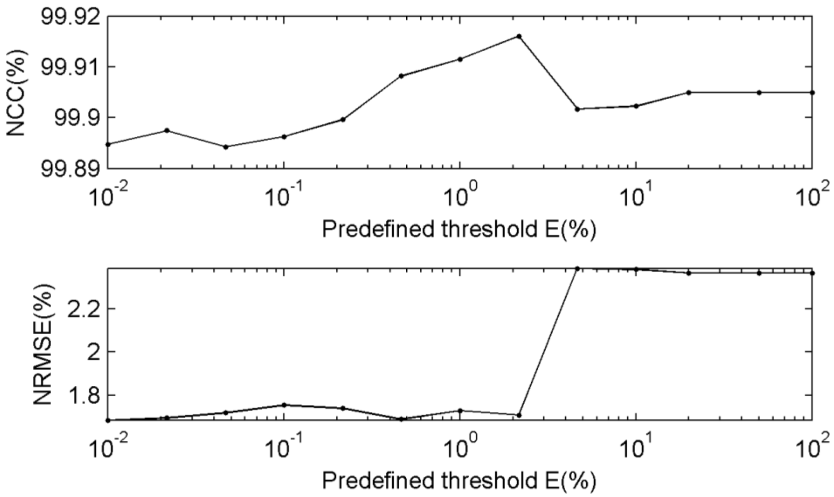

Figure 3.8 – NCC and NRMSE evaluation of the generated LIDs of the RPLED for various predefined thresholds E. The optimal point is located at 2.1%.

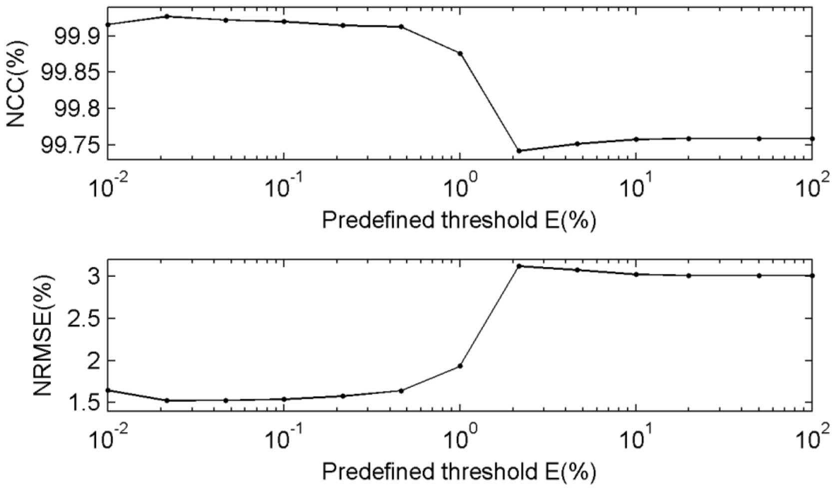

Figure 3.9 – NCC and NRMSE evaluation of the generated LIDs of the RPLED with a BEF for various predefined thresholds E. The optimal point is located at 0.021%.

3.3 Hemispherical light sources

3.3.1 Introduction

While the method presented in section 3.2 works very well for planar light sources it is not capable of characterizing curved light sources. LEDs for example have a planar die, from which light is emitted, often in combination with hemispherical primary optics (i.e. lens). As such, reflections or light scattered from imperfections in the lens cannot be reproduced in simulated luminance images when the source is modeled as a planar structure. An example of these reflections and scattering within the primary optics of an LED is displayed in figure 3.10.

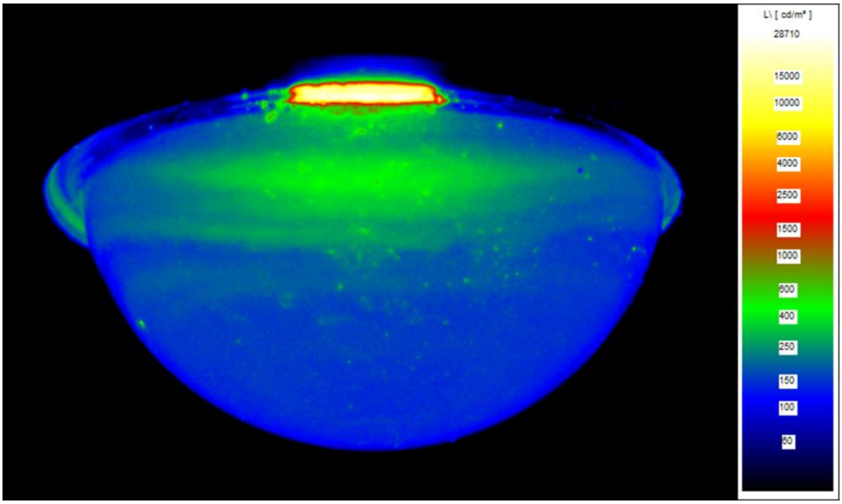

Figure 3.10 – A false color high-dynamic range luminance distribution of a Cree X-RE LED Lamp as seen from 70° away from the normal of the die surface.

To enable simulations of luminance distributions from such a light source characterized by a ray file, the sampling algorithm for planar light sources is adjusted along with the geometry of the virtual model of the light source. A validation of the presented method is again performed by comparing measured luminance distributions with simulated luminance distributions of an LED featuring primary hemispherically shaped optics. A good agreement was obtained, thus validating the presented method.

3.3.2 Methodology

The same approach as discussed in section 3.2 is used for hemispherically shaped light sources. The key difference is the geometrical modeling and the calculations of the LIDs of each pixel. The geometry of these hemispherically shaped light sources can be separated into two parts. First, a planar structure is defined as described in section 3.2. This planar structure lies in the same plane as the die of the LED under consideration. Next, a hemispherical surface is defined which is outside but as close as possible to the outer surface of the primary optics. This hemispherical surface is divided into equal area pixels as described extensively in literature [Gringerton and Yepez, 1992]. As such, a closed surface is formed, which would not be possible by simply dividing a hemispherical surface into flat pixels. The inputs for the algorithm are: the radius of the hemispherical surface and the number of parallels in which the surface should be divided. Figure 3.11 (a) and (b) show such an equal area pixelated hemispherical surface along with a planar structure oriented in a global XYZ coordinate system.

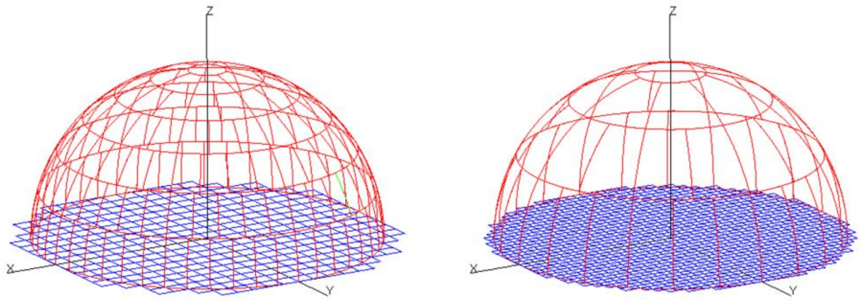

(a) (b)

Figure 3.11 –Geometric model of a hemispherically shaped light source (radius = 2.5mm) featuring equal area pixels on a hemispherical surface in combination with pixels on a planar surface. (a): planar pixel resolution of 0.25mm with 169 spherical pixels. (b): planar pixel resolution of 0.125mm with 49 spherical pixels.

Before the LIDs of the planar pixels and spherical pixels can be calculated, the .ttr proprietary format is converted to a ray file containing the maximum number of rays (10^9). The user defined bounding surface for this conversion is the measurement sphere (the imaginary sphere on which the camera and photometer is positioned during the measurement). Next, the rays in this large ray file are calculated back towards the intersection point of the spherical surface and the planar surface. As such, the large ray file is separated into two ray files; one containing all the rays that only intersect the spherical surface and one containing all the rays that intersect both the planar and hemispherical surface with exclusion of the rays that only intersect the spherical surface. The ray file characterizing the planar surface can then be pixelated and sampled according to the presented method in section 3.2. The rays characterizing the spherical surface are grouped into spherical pixels by evaluating their direction and testing them against the boundaries of each spherical pixel.

The sampling of the rays of each spherical pixel into an LID differs significantly from the sampling of the planar pixels. While the local x-axis of the LIDs of the planar pixels were aligned with the global X-axis making the calculations of each LID relatively straightforward, the LIDs of the spherical pixels need to be calculated relative to a local coordinate system ($xyz_{SP(i)}$) that changes for each point on the spherical surface. To this end, a local coordinate system with its origin located in the central direction of each spherical pixel SP(i) is defined. This difference in local coordinate system of each spherical pixel relative to the global XYZ coordinate system is illustrated in figure 3.12.

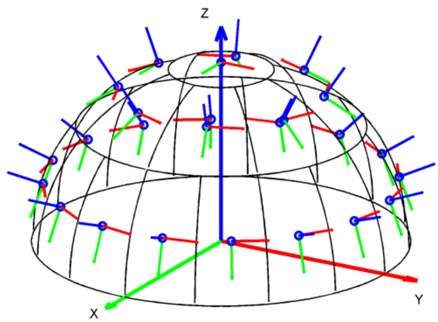

Figure 3.12 –Illustration of the different local coordinate systems, $xyz_{SP(i)}$, defined for each spherical pixel SP(i) compared to the global XYZ coordinate system. The local/global x/X, y/Y and z/Z axis are displayed in green, red and blue respectively.

These local coordinate systems, $xyz_{SP(i)}$, are defined for each spherical pixel SP(i) as follows: first, a local z-axis is defined as a unit vector $\mathbf{z}_{SP(i)}$ which is normal to the spherical surface and which goes through the center of each spherical pixel. Next, a unit vector $\mathbf{zprojXY}_{SP(i)}$ is defined as the projection of $\mathbf{z}_{SP(i)}$ on the global XY plane. A local y-axis, perpendicular to $\mathbf{z}_{SP(i)}$ and $\mathbf{zprojXY}_{SP(i)}$, is then defined as the unit vector $\mathbf{y}_{SP(i)}$ obtained from the vector product $\mathbf{z}_{SP(i)}$ x $\mathbf{zprojXY}_{SP(i)}$. Finally the local coordinate system is completed by a local x-axis defined by the unit vector $\mathbf{x}_{SP(i)}$ found from the vector product $\mathbf{y}_{SP(i)}$ x $\mathbf{z}_{SP(i)}$.

With the local coordinate system defined, the spherical coordinates (θ_r,φ_r) of each ray relative to the local coordinate system can be calculated. θ_r can now be determined for each ray by calculating the angle between the direction of the ray $\mathbf{d}(a,b,c)$ and the local z-axis $\mathbf{z}_{SP(i)}$ to which the ray belongs. Note that $\mathbf{d}(a,b,c)$ is still expressed relative to the global coordinate system XYZ and as such φ_r cannot be calculated as the angle between $\mathbf{d}(a,b,0)$ and the local $\mathbf{x}_{SP(i)}$. The relation between each ray direction $\mathbf{d}$ and the local coordinate system defined by $\mathbf{x}_{SP(i)}$, $\mathbf{y}_{SP(i)}$ and $\mathbf{z}_{SP(i)}$ is expressed as follows:

$$\begin{cases} \boldsymbol{x}_{SP(i)}.\boldsymbol{d} = |\boldsymbol{x}_{SP(i)}||\boldsymbol{d}|\cos(\theta_x) \\ \boldsymbol{y}_{SP(i)}.\boldsymbol{d} = |\boldsymbol{y}_{SP(i)}||\boldsymbol{d}|\cos(\theta_y) \\ \boldsymbol{z}_{SP(i)}.\boldsymbol{d} = |\boldsymbol{z}_{SP(i)}||\boldsymbol{d}|\cos(\theta_z) \end{cases} \tag{3.7}$$

As such, the ray direction $\mathbf{d}$ can now be expressed relative to the local coordinate system:

$$\boldsymbol{d} = |\boldsymbol{d}|\cos(\theta_x)\boldsymbol{x}_{\mathrm{SP(i)}} + |\boldsymbol{d}|\cos(\theta_y)\boldsymbol{y}_{\mathrm{SP(i)}} + |\boldsymbol{d}|\cos(\theta_z)\boldsymbol{z}_{\mathrm{SP(i)}} \tag{3.8}$$

The spherical angle φ_r relative to the local coordinate system can now be defined as the angle between the projection of vector **d** onto the $\mathbf{x}_{\mathrm{SP(i)}}\mathbf{y}_{\mathrm{SP(i)}}$ plane and the unit vector $\mathbf{x}_{\mathrm{SP(i)}}$.

With the spherical coordinates (θ_r,φ_r) calculated of each ray relative to the local coordinate system, the sampling method as presented in section 3.2 can be maintained. Note that in the ray tracer the local x-axis also needs to be defined correctly for each spherical pixel to ensure that the C0 plane of each LID corresponds to the pixel orientation of each surface source.

3.3.3 Experimental validation

To validate the presented method, a practical example of a hemispherically shaped light source (Luxeon Rebel LED [Philips, 2013]) is selected. The near-field light distribution of the LED was measured and a ray file containing 10^9 rays was generated. This ray file was processed and sampled according to the algorithm presented in section 3.3.2. The planar pixel resolution was set to 0.125 mm, resulting in 368 planar pixels, while the hemispherical surface with radius 1.264 mm was divided into 961 pixels. Again, several models were created with different predefined flux thresholds to determine the optimal angular binning for each LID of each pixel. The resulting LID from each model was compared by calculating the NCC and NRMSE value with the LID of the ray file. The result of this comparison is shown in figure 3.13.

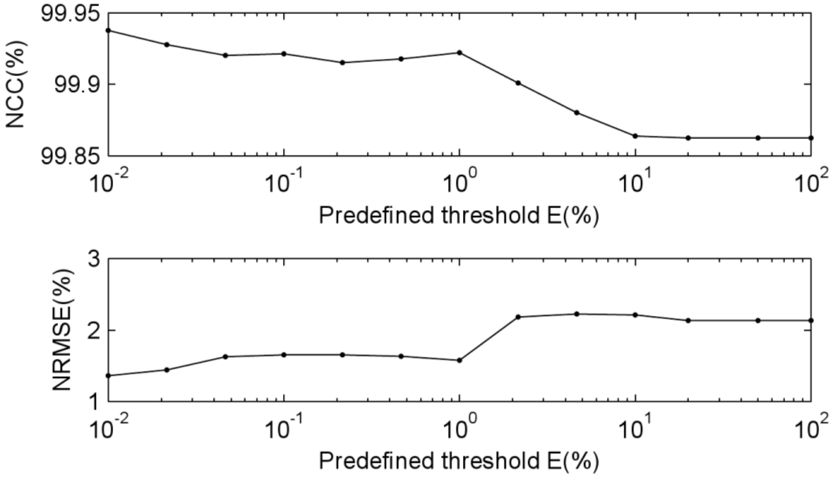

Figure 3.13 – NCC and NRMSE evaluation of the generated LIDs of the LED for various predefined thresholds E. The optimal point, i.e. the maximum and minimum for NCC and NRMSE, is located at 0.01%.

Similar to the results discussed in section 3.2.4, the NCC and NRMSE values respectively become higher and lower as the predefined threshold decreases. However, unlike the previous results no overfitting occurs even for the smallest predefined flux threshold under consideration. As such, the model generated with the lowest predefined threshold is considered to be the best. The model could be further improved by dividing both the planar and hemispherical surface into more pixels. However, as more pixels are defined, more LIDs and corresponding surface sources need to be defined in the ray tracer. It was found though, that the commercial ray tracer used during this research was not able to cope with such a large amount of surface sources without an excessive increase in ray tracing time. For example, one luminance distribution of a model containing ~2000 surface sources can easily amount to a ray trace of 7 hours and above on an Intel® Core™ i7-3770 Processor. In addition, the required time to perform the calculations is proportional to the number of surface sources defined in the model. This is mainly due to the specific implementation of the ray tracing algorithm for luminance distributions in the ray tracer as it calculates a single luminance distribution per active light source (i.e. one light source is set to be active while all other light sources are disabled). This is repeated for all light sources in the model and afterwards a mean luminance distribution can be calculated, resulting in the final luminance distribution of all light sources present in the model.

With the model of the light source fully defined, luminance distributions can be simulated. Each luminance map has a width and height equal to 2.5 mm and is divided into pixels with a width and height of 0.05 mm. For each pixel in the luminance map, 10^3 rays are traced. The observer position is expressed in spherical coordinates (θ_o,φ_o), while the distance between the observer and center surface remains 1 000 mm. Luminance maps for the observer positions (θ_o,φ_o) = (0°,0°), (30°,0°), (60°,0°) and (90°,0°) were simulated and are shown in figure 3.14 along with the measured luminance distributions of the LED and a difference image which is calculated as given by equation 3.4. A good visual agreement is obtained, although similar to the luminance distributions simulated for planar light sources, the differences between measured and simulated luminance distributions become larger as the observer position θ_o increases. It becomes however very clear that this type of light source cannot be simulated using only a planar surface structure as this would result in a completely dark luminance map for large observation angles.

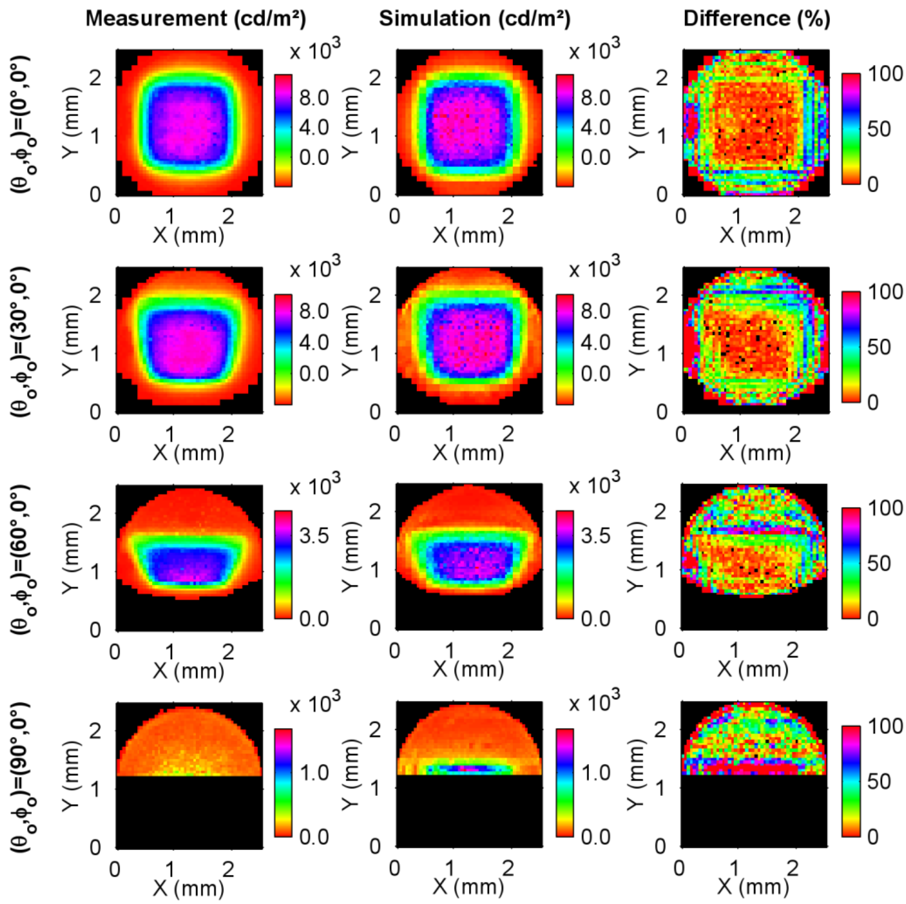

Figure 3.14 – Comparison between the measured (left column) and simulated (middle column) luminance maps for the observer positions: (θ_o,φ_o)=(0°,0°), (θ_o,φ_o)=(30°,0°), (θ_o,φ_o)=(60°,0°) and (θ_o,φ_o)=(90°,0°) of a LED. Right column: percentage difference images between the measured and simulated luminance maps.

A quantitative comparison between the simulated and measured luminance maps is performed by calculating the NCC and NRMSE values as given by equation 3.5 and 3.6, which are presented in table 3.3. A good quantitative agreement is found for all simulated luminance maps. Even though the NCC value for the observer position (90°, 0°) is clearly lower than for the other observer positions, the value is still satisfactory.

Table 3.3. Comparison between the simulated and measured luminance maps of the LED. Normalized cross correlation ratio (NCC) and normalized root-mean-squared error (NRMSE) calculated for different observer positions of the measured and simulated luminance map.

	Δ*d* = 0.125 mm 961 spherical pixels	
Observer position (θ_o,φ_o)	***NCC (%)***	***NRMSE (%)***
(0°, 0°)	99.0	5.2
(30°, 0°)	97.9	7.3
(60°, 0°)	97.9	5.6
(90°, 0°)	74.9	8.9

Vertical cross sections of the luminance maps for each of the observer positions were created as shown in figure 3.15. These cross sections again show that there is a good correspondence between the measured and simulated luminance distributions, except at larger viewing angles (towards (θ_o,φ_o)= 90°,0°).

One of the reasons for the low correspondence at large viewing angles might originate from the fact that the original ray file was measured using a luminance camera which uses the same integration time for every position. As the absolute peak luminance value as seen from an observer position (θ_o,φ_o)= (0°,0°) is around 14 times higher than the absolute luminance value as seen from the observer position (θ_o,φ_o)= (90°,0°), a much lower signal will be present at these larger viewing positions. This also implies a less accurate representation of the light distribution (i.e. ray file) as seen from these positions and thus a less accurate model will be obtained. On the other hand, the measured luminance distributions, to which the comparison is made, were captured using various integration times resulting in high dynamic range luminance distributions.

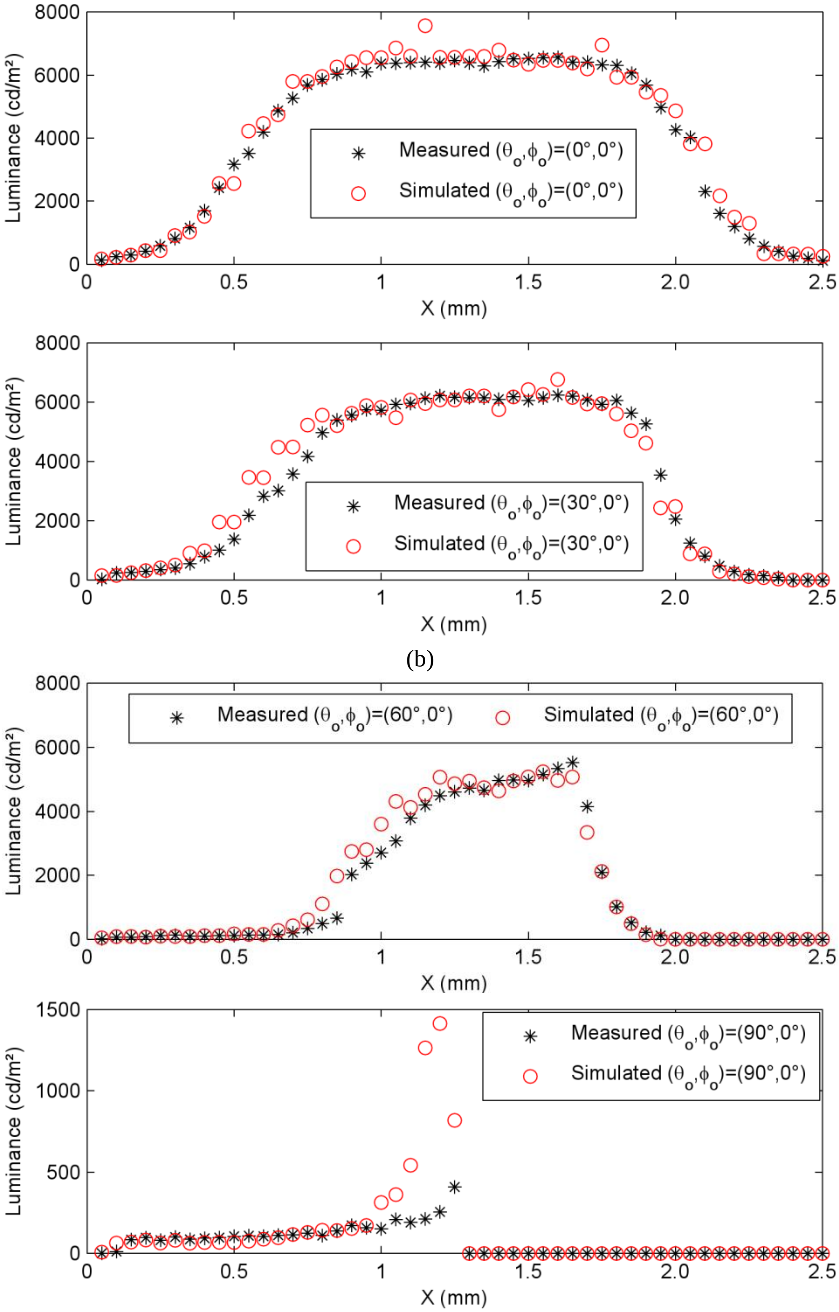

Figure 3.15 – Vertical cross section at the horizontal center of the the measured (stars) and simulated (circles) luminance maps for the observer positions: (θ_o,φ_o)=(0°,0°), (θ_o,φ_o)=(30°,0°), (θ_o,φ_o)=(60°,0°) and (θ_o,φ_o)=(90°,0°) of a LED.

The light source model can not only be used to simulate luminance distributions but offers also a valuable approach during the development stage of a luminaire. A specific lens designed to transform the original emitted luminous intensity distribution of the LED to a very narrow beam was positioned in close proximity of the light source (figure 3.16).

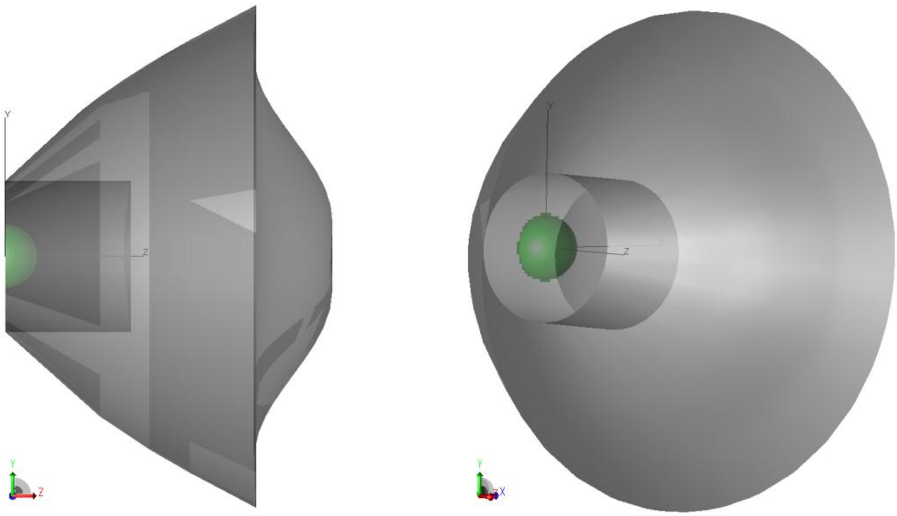

(a) (b)

Figure 3.16 – Illustration of the lens in combination with the light source model of the LED, oriented in the YZ plane (a) and a 3D view (b).

The lens was created by an iterative hill climbing optimization algorithm [Burke and Kendall, 2005] implemented in Scheme (TracePro's embedded scripting language). Although, the ray tracer contains an off-the-shelf optimization package, our own implementation of an optimization algorithm was used as this offered more freedom to adjust optimization parameters. The material of the lens was defined as glass (BK7-Schott) with a refractive index of 1.51 and an absorption coefficient of $0.2\,\mathrm{m}^{-1}$. The merit function for the optimization algorithm was defined as the incident flux on a circular surface (radius of 15mm) in front of the lens at a distance of 131mm from the light source model, divided by the total emitted flux by the light source. As such, both the directionality and efficiency of the lens is optimized to create a beam with a full width of $2\mathrm{x}\tan^{-1}(15/131)\approx 13°$. During the optimization process the ray file of the LED was used as light source.

Afterwards, the luminous intensity distributions obtained from the ray file/lens approach and from the hemispherical light source model/lens approach are compared. In addition as a third option, a square surface source, with approximately the same size as the die of the LED, was defined with a lambertian intensity distribution which, when integrated, results in the same total luminous flux as the ray file. In this way, the need to accurately model a light source during the design of such an optical system can be illustrated. The results of this comparison are shown in figure 3.17.

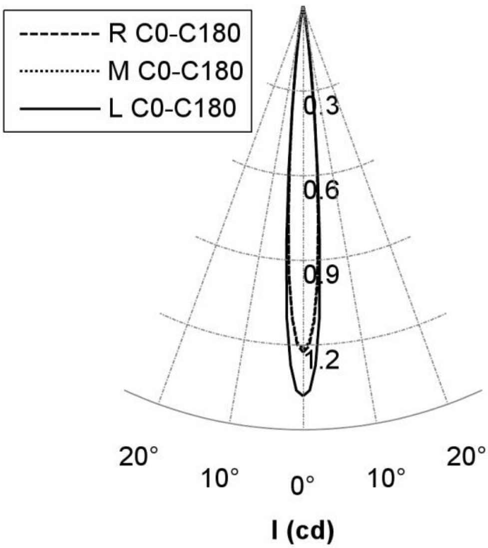

Figure 3.17 – Luminous intensity distribution of the ray file/lens (R), hemispherical light source model/lens (M) and lambertian square surface source/lens (L) combination in the C0-C180 plane. Note that R and M are highly similar and thus coincide in the figure.

From figure 3.17 it becomes clear that both the ray file as the hemispherical light source model are equally accurate for the design of such a lens as the resulting luminous intensity distribution can be considered to be equal. The lambertian surface source model however, is not able to capture all the necessary details of the light source, which is clearly visible as the resulting LID shows a significant difference compared to LID of the ray file/lens combination.

3.4 Conclusions

In this chapter, an innovative method to sample ray files of planar and hemispherical light sources into a set of LIDs is presented. These LIDs can easily be imported in any ray tracing software and applied to surfaces in order to create a set of surface sources. This state-of-the-art contribution enables the simulation of luminance maps which are of high importance when predicting the discomfort glare or contrast of virtual prototypes of optical systems, while maintaining the high accuracy offered by a ray file.

Two practical examples, one for a planar source and one for a planar source with a hemispherical dome, are discussed in order to validate the algorithm. Experimental luminance images were compared to simulated luminance images. In both examples a good agreement was obtained, validating the method for both planar and non-planar light sources. The sampling method also has the benefit of drastically reducing disk space requirements to characterize the near-field of a light source. In addition, the light source model created with the presented method is able to generate as many rays as necessary compared to ray files which always have a fixed amount of rays upon creation. Finally, it was shown that the generated models can also be used for the optical design of optics located in close proximity of the light source.

The method can be further expanded to allow other geometries such as a cylinder which would be ideally suited to model high intensity discharge lamps and compact fluorescent lamps as these typically have a cylindrical light emitting surface.

Chapter 4

Impact of the bidirectional scattering distribution function on intensity and luminance distributions of luminaires

Not only the light source of a luminaire, but also the materials surrounding the light source play an important role in shaping the intensity and luminance distribution of the luminaire. Therefore, as an optical designer it is necessary to know to what extent the reflectance and/or transmittance properties of the surrounding material should be modeled in order to enable accurate simulations of the luminous intensity distribution and/or the luminance distributions. BRDF data can be modeled in different ways, ranging from simple predefined functions to detailed tabulated data.

In this chapter we investigate the impact of the accuracy of the implemented reflectance data on ray tracing simulations. In section 4.1 the impact of the model applied to a diffuse reflecting material on simulated luminance distributions and LIDs is discussed. The same analysis is also performed for a material exhibiting a strong specular component (section 4.2).

4.1 Diffuse materials

4.1.1 Introduction

Highly reflective diffuse materials are used very frequently in LED luminaires, especially when the output of individual LED packages is to be combined in an optical mixing chamber, such as in the remote phosphor concept [Hoelen et al, 2008]. The role of the optical mixing chamber is important as it causes light emitted by an array of LEDs to be homogenized both angularly and spatially before it reaches a remote phosphor plate [Narendran, 2005a; Narendran 2005b] while maintaining high system efficiencies. Such a highly reflective diffuse material which is already being used in commercial illumination systems is the material Microcellular PolyEthylene Terephthalate (MCPET). According to the manufacturers datasheet, the material has a total reflectance of 99% and a diffuse reflectance of 96% [American Furukawa Inc., 2008].

The Bidirectional Reflectance Distribution Function (BRDF) is used to describe the amount of light scattered by a surface as the direction of illumination and/or viewing is changed. In this section, we investigate the influence of the implemented BRDF model of the MCPET material on simulated luminance distributions of an illumination system that incorporates the highly reflective diffuse material. Three distinct models were implemented. First, a simple model for a perfect diffuser was created based on the total reflectance measured with an integrating sphere. Second, a diffuse/specular reflectance model was defined by combining the integrated sphere measurement with specular reflectance measurements obtained from a goniospectrophotometer [Leloup et al., 2008]. Finally, a third model was created as a table containing all experimental BRDF data.

To compare a luminance map generated by a ray tracer to a luminance map measured by a luminance camera, a prototype of a cylindrical optical mixing chamber was constructed out of MCPET. A model of this prototype was created in TracePro® and the different BRDF models were implemented to model the optical scattering from the chamber walls. For each BRDF model, luminance maps of the optical mixing chamber were simulated and compared with a measured luminance image. Similarly, the LID calculated from these ray trace models were compared with the experimental LID obtained with a near-field goniophotometer (RiGO 801 – TechnoTeam) [Bredemeier et al., 2007; CIE TC-2-62, 2010].

4.1.2 Experimental set-up

A cylindrical optical mixing chamber with diameter 43 mm and height 21.4 mm was created out of a 1 mm thick sheet of MCPET material. Four circular holes with diameter 5 mm were drilled in the baseplate of the cavity. The same geometry was also modeled in the ray tracer. Next, a remote phosphor LED module (RPLED) [Xicato, 2013] was positioned behind the baseplate in order to create four uniform and lambertian emitting light sources. The edges of the 4 circular holes in the baseplate were painted black. This was done because the optical properties of the holes cannot be determined experimentally as the process of drilling the holes changes the optical properties of the material’s surface. By painting the edges of the hole black, it can be modeled as a perfect absorber in the ray tracer. The prototype is presented in figure 4.1.

Figure 4.1 – Prototyped cylindrical mixing chamber constructed out of MCPET including 4 uniform lambertian light sources created by partially covering a remote phosphor LED module with an MCPET baseplate.

The RPLED module was powered with a current of 10 mA. Luminous flux measurements revealed that each circular light source emits 0.96 lm. A RPLED module was chosen as primary light source as it has a uniform exitance and emits lambertian at each point across the light emitting surface. This facilitates the modeling of the four distinct light sources in the ray tracer as lambertian surface sources, each emitting 500 000 rays. Furthermore, this enables and facilitates the simulation of a luminance map, as a uniform exitance is assumed. A well-defined LID of the light source allows for the application of importance sampling [Dutré et al., 2006]. A first simulation revealed that with this geometry and light sources, 40% of the emitted light was incident on the inner surfaces of the module and indeed a suitable mixing chamber was constructed.

4.1.3 MCPET BRDF measurement and modeling

4.1.3.1 Diffuse BRDF model

A completely diffuse model, $BRDF_{diff}$, implies that the BRDF value is constant for every incident direction (θ_i, ϕ_i) and scatter direction (θ_s, ϕ_s). The total spectral reflectance, $R_{total}(\lambda)$ of the MCPET material was determined with an integrating sphere based spectrophotometer (Hunterlab – UltraScan Pro) and is shown in figure 4.2 along with the relative spectrum emitted by the RPLED module.

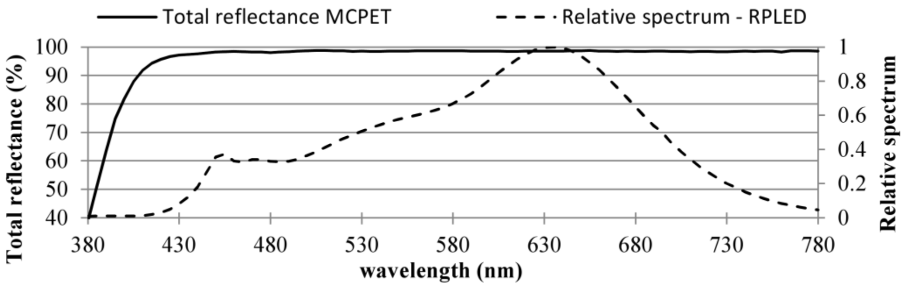

Figure 4.2 – Total reflectance of MCPET (solid line) and the relative spectrum of the RPLED module (dashed line) across the visual region.

From figure 4.2, it becomes clear that the variation of the total spectral reflectance over the LED emission wavelength interval can be neglected. This is a tremendous advantage during ray tracing simulations as only one wavelength will need to be traced and/or analyzed. To this end, the total reflectance (R_{total}) of MCPET is calculated as a mean value weighted by the relative spectrum of the RPLED module, and equals 98.4% (absorbance of 1.6%). The BRDF value for a completely diffuse material is calculated as:

$$q = \frac{R_{total}}{\pi}\left[\frac{1}{\text{sr}}\right] \tag{4.1}$$

and becomes 0.313 sr^{-1}.

4.1.3.2 Diffuse/Specular BRDF model

A diffuse/specular BRDF model, $\text{BRDF}_{\text{diff/spec}}$, requires more measurements but offers a more accurate description of the real BRDF. Spectral specular reflectance measurements were performed using a goniospectrophotometer [Leloup et al., 2008], discussed in section 1.3.2, in which the MCPET sheet is positioned under an incident angle θ_i ranging from near normal incidence to near grazing angle. The spectral specular reflectance values, $R_{\text{spec}}(\lambda,\theta_i)$, are again weighted with the spectrum of the RPLED module and are called $R_{\text{spec}}(\theta_i)$. The values of R_{spec} are plotted and displayed for the incident angles θ_i = 5°, 25°, 45°, 60°, 70° and 80° in figure 4.3. The values are combined with R_{total} in order to create a diffuse/specular BRDF model. For each incident angle, a corresponding diffuse BRDF component can be calculated as follows:

$$q_{diff} = \frac{R_{total} - R_{\text{spec}}(\theta_i)}{\pi}\left[\frac{1}{\text{sr}}\right] \tag{4.2}$$

These BRDF values remain constant for every scatter direction (θ_s, ϕ_s) but change with the incident angle θ_i as R_{spec} also changes with the incident angle. This correlation is also shown in figure 4.3.

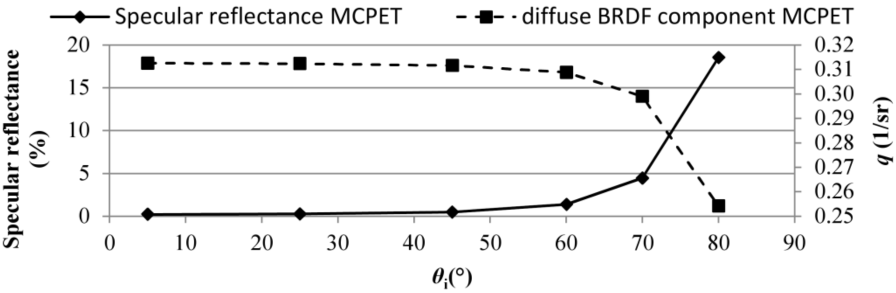

Figure 4.3 – Specular reflectance values of MCPET (solid line) and diffuse BRDF component (dashed line) for the incident angles 5°, 25°, 45°, 60°, 70° and 80°.

4.1.3.3 Tabular BRDF model

The final approach, BRDF_{tab},which is also the most accurate representation of the real BRDF, is formulated in the ray tracer as a lookup table. Scattered flux measurements at scatter angles (θ_s, ϕ_s), located in the plane of incidence (Π_1) and in a plane Π_2 perpendicular to the plane of incidence and through the specular direction, were performed for the incident angles θ_i = 5°, 25°, 45°, 60°, 70° and 80° using the goniospectrophotometer. The corresponding BRDF values are calculated according to equation 1.2 and weighted with the spectrum emitted by the RPLED module. The BRDFs measured in the planes Π_1 and Π_2 are shown in figure 4.4.a and 4.4.b respectively. If necessary, the ray tracing software will automatically perform a linear interpolation between the values in the lookup table for any $(\theta_i, \phi_i, \theta_s, \phi_s)$ combination not present in the table. Appendix A discusses the theoretical background of the coordinate systems used during the conversion process of BRDF measurements to the tabular BRDF model. The algorithm and practical implementation of this conversion process is discussed in appendix B.

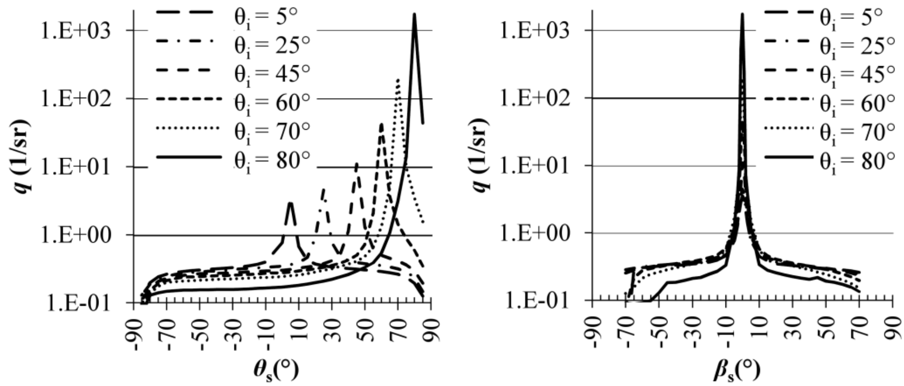

(a) (b)

Figure 4.4 – (a) Measured BRDF of MCPET in the plane of incidence. (b) measured BRDF of MCPET in a plane perpendicular to the plane of incidence and through the specular direction. θ_s defines the angular offset of each scatter direction to the normal in the plane of incidence; β_s defines the angle to the specular direction in the perpendicular plane.

4.1.4 Experimental validation

The geometry of the optical mixing chamber, the characteristics and the position of the 4 light sources, and the optical properties of the MCPET material were used as input data in the ray tracing software. A luminance map for an observer positioned at an angle of 55° away from the direction perpendicular to the baseplate of the mixing chamber was calculated. This angle was chosen specifically as none of the four separate light sources can be viewed directly. As the focus of these experiments lies on the effect of the BRDF modeling on simulated luminance maps; the light sources are implemented as lambertian surface sources. This way, the LID can be sampled and the luminance maps can be calculated through the use of reverse ray tracing. The luminance image is composed of 125x250 pixels of 0.2 mm width located in a plane perpendicular to the viewing direction and through the center of the aperture of the cavity. For each pixel 1000 rays were traced from the observer point of view towards the optical mixing chamber. Luminance map calculations were performed with each of the 3 different BRDF models applied to the surfaces of the optical mixing chamber. Furthermore, a high dynamic range luminance image was captured using a luminance camera of a near-field goniophotometer [Bredemeier et al., 2007] positioned at exactly the same observer position. Figure 4.5 shows an overview of the luminance images for each BRDF approach (figure 4.5.a – 4.5.c), together with the measured luminance image (figure 4.5.d).

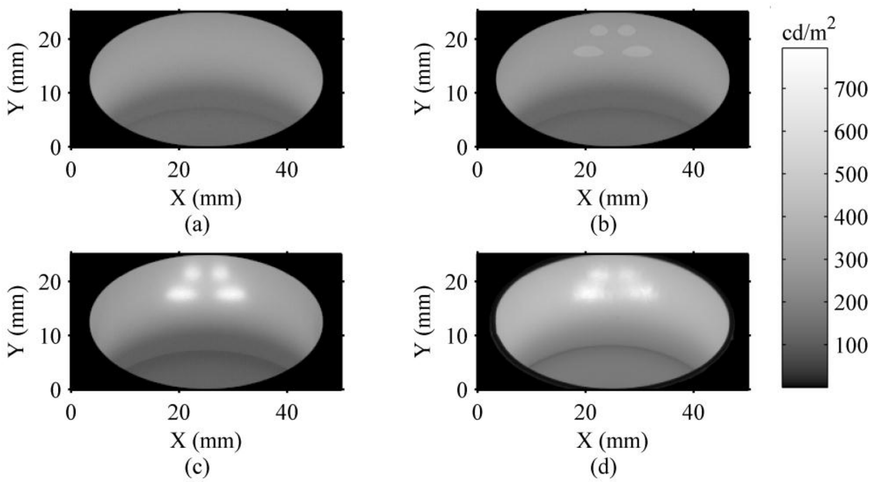

Figure 4.5 – Grayscale luminance images of the optical mixing chamber with the observer position at 55° away from the direction perpendicular to the base plate. (a), (b) and (c) are simulated luminance images obtained with $BRDF_{diff}$, $BRDF_{diff/spec}$ and $BRDF_{tab}$ applied to the surface of the optical mixing chamber, respectively. (d) Measured luminance image of the prototyped optical mixing chamber.

The experimental luminance image contains 4 highlights, each originating from one of the circular light sources in the cavity. In figure 4.5.a however, no highlights can be distinguished. This is to be expected as the surfaces of the cavity are modeled using the completely diffuse $BRDF_{diff}$ approach. On the other hand, the simulated luminance image obtained with the $BRDF_{diff/spec}$ approach does contain 4 distinct highlights. Yet, these highlights have very sharp edges much unlike the blurred highlights found in the measured luminance image. These sharp edges originate from the diffuse/specular modeling approach, as the non-diffuse component in this model is scattered only into one single direction (i.e. the specular direction). When the $BRDF_{tab}$ model is applied to the mixing chamber surfaces, as seen in figure 4.5.c, a much better resemblance with the measured luminance image is obtained. Due to a wider angular scattering around the specular reflection direction (cf. figure 4.4), the reflected highlights now become also blurred. A clear difference between the peak luminance value of the highlights is also visible for the $BRDF_{diff/spec}$ and $BRDF_{tab}$ approach, the latter showing a high resemblance with the peak luminance values of the measured luminance image.

NCC and NRMSE values are used in a similar way as in section 3.2.3 to quantitatively compare luminance distributions. For each luminance image, a particular region around the specular highlights was extracted as illustrated in figure 4.6. NCC, NRMSE, maximum and mean values of these regions were calculated and are displayed in table 4.1. Additionally, the uniformity ratio U of each region around the specular highlights ranging from Y=15 to 23 mm and X=15 to 35 mm is calculated as the ratio of the minimum value to the mean value and is listed in table 1.

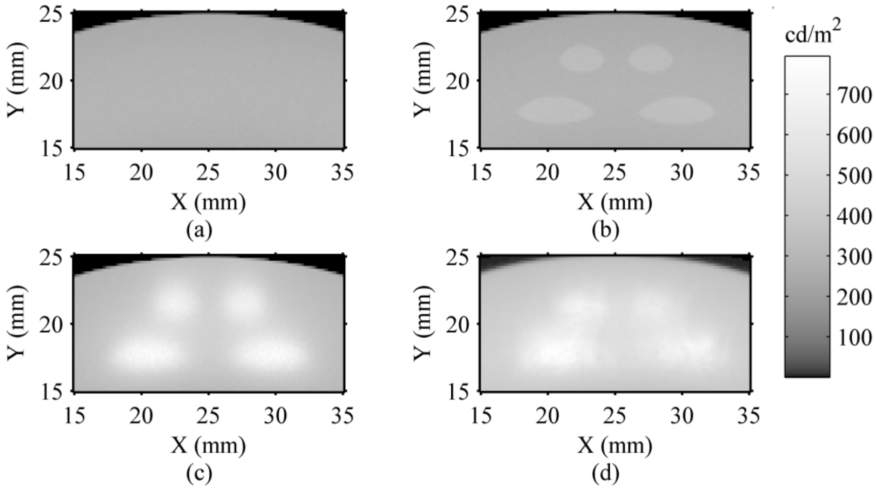

Figure 4.6 – Extracted region of the grayscale luminance images of the optical mixing chamber that include specular highlights at an observer position of 55° away from the direction perpendicular to the base plate. (a), (b) and (c) are simulated luminance images obtained with $BRDF_{diff}$, $BRDF_{diff/spec}$ and $BRDF_{tab}$ respectively applied to the surfaces of the optical mixing chamber. (d) Measured luminance image of the prototyped optical mixing chamber.

Table 4.1: Validation of the simulated luminance maps of the virtual model with the three different BRDF models compared to the luminance image of the prototyped optical mixing chamber expressed by means of the calculated NCC, NRMSE, maximum, mean and uniformity values of the region around the specular highlights.

Near-field	**NCC (%)**	**NRMSE (%)**	**Max (cd/m²)**	**Mean (cd/m²)**	**U**
Measurement	-	-	794	470	0.68
$BRDF_{diff}$	80.07	28.32	309	265	0.87
$BRDF_{diff/spec}$	86.96	27.54	356	268	0.85
$BRDF_{tab}$	94.61	9.14	783	416	0.65

As expected from the visual inspection of the luminance images (figure 4.6.a to 4.6.d), the NCC and NRMSE values respectively increase and decrease when the representation of the BRDF of the MCPET material becomes more accurate. The best result is achieved when attributing the most accurate, yet most time consuming, BRDF model ($BRDF_{tab}$) to the surface of the optical mixing chamber. With a value of 95% for NCC and 9% for NRMSE, the simulation results can be classified as very successful. Note that the uniformity ratio of $BRDF_{tab}$ is highly similar to the uniformity ratio of the measured luminance map while this is not the case for the luminance map obtained with the $BRDF_{diff}$ and $BRDF_{diff/spec}$ model. This illustrates the strength of simulation software in predicting luminance maps when accurate input data are available. Deviations from perfect validation might originate from the fact that the prototyped mixing chamber is not an exact replica of the virtual model, as slight deviations of the geometry can occur. Also note that around 32% of the emitted light is directly incident on the vertical edges of the circular holes in the baseplate which are painted black, and thus still reflect some light, whereas in the simulations they are modeled as perfect absorbers. This is further discussed in section 4.2.5.

It might seem strange that even though the scattered luminous flux in the specular direction remains the same for both the $BRDF_{tab}$ and $BRDF_{diff/spec}$ model, an important difference in peak luminance value is observed (table 4.1). A possible reason might be found in the fact that the spatially extended light sources are located in the proximity of the surfaces of the cavity. Due to this, light emitted from the source going towards a point on the wall of the cavity will hit this point under different incident angles. Furthermore, the $BRDF_{tab}$ model scatters a portion of the incident light towards a wide angular range around the specular component (near-specular reflection, r'''), while the $BRDF_{diff/spec}$ model does not contain this contribution. As a result, the highlights obtained with the $BRDF_{diff/spec}$ approach originate almost exclusively from a specular reflection component (r'). However, the highlights obtained with the $BRDF_{tab}$ approach originate from the specular reflection component together with an important near-specular reflection contribution. A schematic of this is presented in figure 4.7.

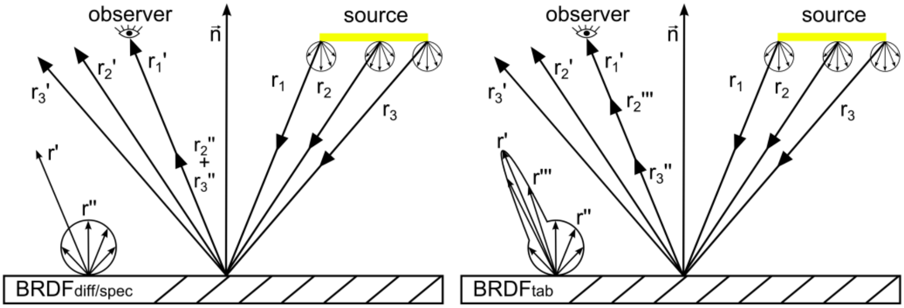

Figure 4.7 – Schematic representation of the luminance contribution caused by specular (r'), diffuse (r'') and near-specular (r''') reflection with the $BRDF_{diff/spec}$ (left) and $BRDF_{tab}$ (right) model applied to a surface in proximity to a spatially extended light source.

One can ask the question whether the accuracy of the BRDF modeling also has a large impact on the LID of the optical mixing chamber. As such, simulations of the luminous intensity distribution (LID) were performed with each of the BRDF models applied to the surfaces of the mixing chamber. The LID of the prototyped mixing chamber was also determined with a near-field goniophotometer. Cross sections of the LID were made at the C0-C180 and C45-C225 planes, which are defined as shown in figure 4.8.

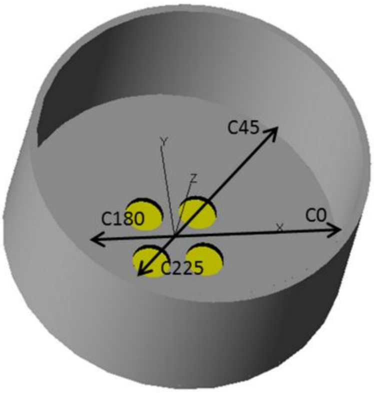

Figure 4.8 – Virtual model of the optical mixing chamber showing the orientation of the C0-C180 and C45-C225 planes.

A very good agreement between the simulated and measured LID is achieved as can be seen in figure 4.9, regardless of the BRDF model that is applied to the surfaces of the optical mixing chamber. It seems that the required accuracy level of the BRDF data for predicting far field intensity distributions is much less stringent than for predicting luminance maps. Indeed, if the specular reflection component is small compared to the total reflectance, far field calculations are rather insensitive to any particular spatial variation of luminance. Moreover, the intensity within one direction can be considered as a spatial integration of the luminance as viewed from that direction. As a consequence, particular spatial variations will be cancelled out and the intensity distribution will become similar as long as the same amount of power is emitted into that direction.

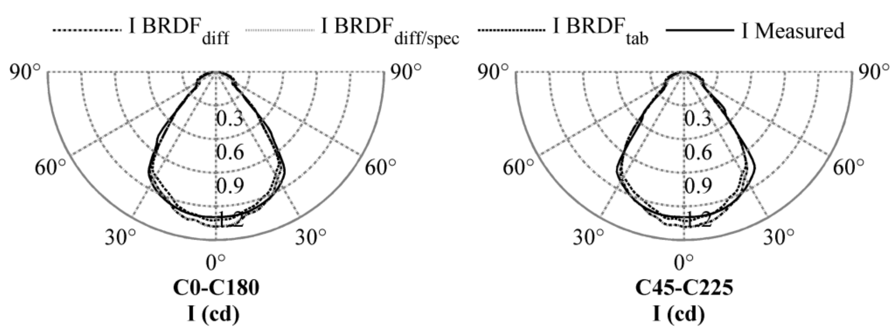

Figure 4.9 – Validation of the LID of the virtual model when applying the 3 different BRDF models and as measured (full line). Left: C0-C180 plane, Right: C45-C225 plane.

4.2 Specular materials

4.2.1 Introduction

While section 4.1 discussed the impact of highly diffuse reflective materials on simulated luminance distributions and luminous intensity distributions, this section discusses the impact of highly specular reflective materials on both quantities. As such, both limiting cases of reflective behavior are discussed. First the MCPET material was treated to exhibit a strong specular reflection component. Next, two distinct BRDF models were created from goniospectrophotometer measurements; a diffuse/specular model and a model containing tabulated measured BRDF values. Afterwards, measured and simulated luminance distributions of an optical mixing chamber were compared.

4.2.2 Experiment set-up

The same geometry as the optical mixing chamber and light source as presented in section 4.1.2 was adopted. However, in order to obtain a material that exhibits a strong specular reflection, the MPET material, shown in figure 4.10.a was coated with a high gloss white paint.

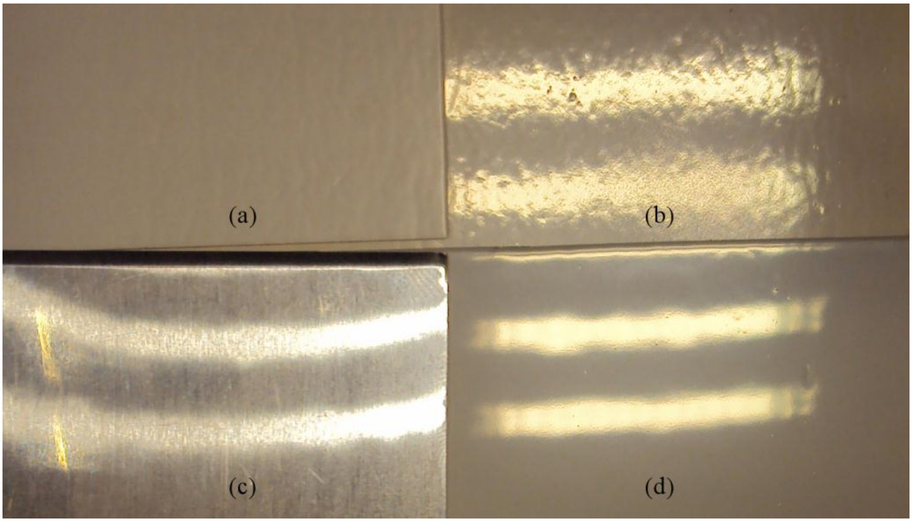

Figure 4.10 – Reflected image of 2 light sources on various materials. (a) MCPET, (b) MCPET coated with a high gloss paint, (c) aluminum coated MCPET, (d) aluminum coated MCPET with an additional high gloss paint coating.

As can be seen from figure 4.10.b the paint coated MCPET shows a higher near-specular reflectance but not really a true specular reflectance as the reflected image

is somewhat distorted. This is caused by the original surface roughness which is still present after coating the MPET material. A variant of the MPET material which is coated with an aluminum layer, has a smoother, though, structured surface. Due to this structured surface a distorted reflected image is created, as is shown in figure 4.10.c. To eliminate this distortion the glossy paint was applied as coating to the aluminum coated MPET material, from now on referred to as gloss painted MCPET (GPMCPET). As a result a near-perfect specular reflectance is obtained as can be seen in figure 4.10.d. The advantage of this material is that it can still be shaped similar to the geometry of the optical mixing chamber presented in section 4.1.2 while exhibiting a strong specular reflectance.
The wall surface of the circular holes in the baseplate of the optical mixing chamber was again painted black as the optical properties of these surfaces cannot be determined experimentally.

4.2.3 High gloss painted aluminium MCPET BRDF measurement and modeling

The GPMCPET material contains a strong specular reflection component. For this reason, the BRDF model presented in section 4.1.3 (complete diffuse reflection) is not implemented. The BRDF models $BRDF_{diff/spec}$ and $BRDF_{tab}$ however were implemented as these offer capabilities of representing specular components.

4.2.3.1 Diffuse/Specular BRDF model

Similar to the regular MCPET material, the total spectral reflectance, $R_{total}(\lambda)$, of the gloss painted MCPET (GPMCPET) material was determined in a sphere based spectrophotometer and is shown in figure 4.11 along with the relative spectrum emitted by the RPLED module.

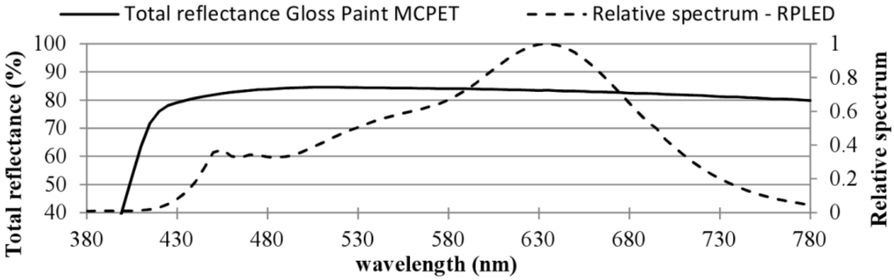

Figure 4.11 – Total reflectance of GPMCPET (solid line) and the relative spectrum of the RPLED module (dashed line) across the visual region.

Again the total reflectance can be considered to be wavelength independent as no abnormal variations of the reflectance occur across the LED emission wavelength region. As such the total reflectance (R_{total}) is again calculated as a mean value weighted by the relative spectrum of the RPLED module, and equals 83.2% (absorbance of 16.8%).

To complete the diffuse/specular model, $BRDF_{diff/spec}$, spectral specular reflectance measurements were performed and the diffuse BRDF component was calculated according to equation 4.2. The measured and calculated, specular and diffuse component, respectively, of the model for various incident angles are shown in figure 4.12.

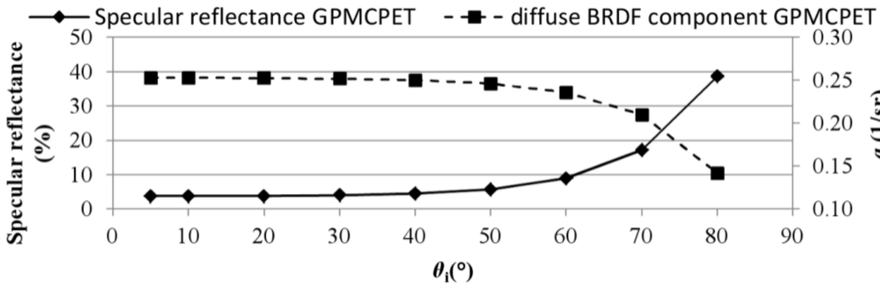

Figure 4.12 – Specular reflectance values of GPMCPET (solid line) and diffuse BRDF component (dashed line) for the incident angles 5°, 10°, 20°, 30°, 40°, 50°, 60°, 70° and 80°.

4.2.3.2 Tabular BRDF model

In order to create the tabular model, $BRDF_{tab}$, scattered flux measurements were performed at scatter angles (θ_s, ϕ_s) located in the plane of incidence (Π_1) and in a plane Π_2 perpendicular to the plane of incidence and through the specular direction, for the incident angles θ_i = 10°, 40°, 60° and 80° using the goniospectrophotometer. The corresponding BRDF values are calculated according to equation 1.2 and weighted with the spectrum emitted by the RPLED module. The BRDF measured in the planes Π_1 and Π_2 are shown in figure 4.13.a and 4.13.b respectively. The tabulated BRDF model based on the BRDF measurements is created as discussed in appendix B.

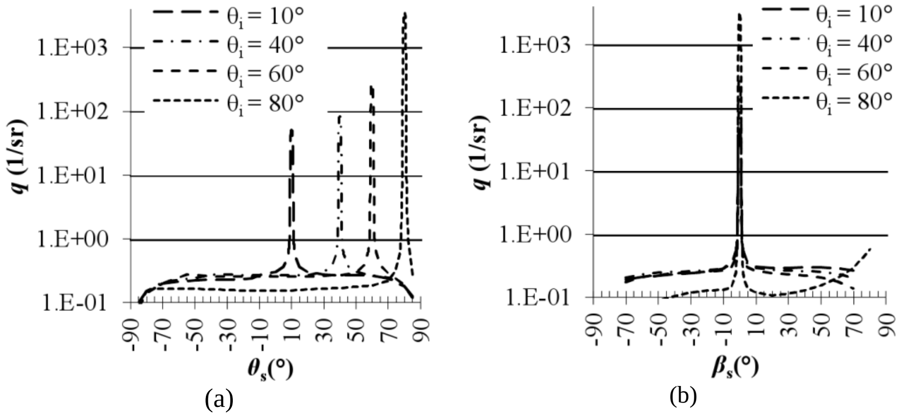

Figure 4.13 – (a): Measured BRDF of GPMCPET in the plane of incidence. (b): measured BRDF of MCPET in a plane perpendicular to the plane of incidence and through the specular direction. θ_s defines the angular offset of each scatter direction to the normal in the plane of incidence; β_s defines the angle to the specular direction in the perpendicular plane.

4.2.4 Experimental validation

Similar to the experimental validation performed in section 4.1.4, luminance distributions were simulated for an observer position 55° away from the normal of the baseplate of the optical mixing chamber with the $BRDF_{diff/spec}$ and the $BRDF_{tab}$ model applied to the surfaces of the mixing chamber. These simulated luminance distributions are visually compared to the measured luminance distribution, as shown in figure 4.14. At a first glance, both models seem to yield comparable results. The highlights present in the luminance distribution simulated when the $BRDF_{diff/spec}$ model is applied, seem to have a sharper edge as opposed to when the $BRDF_{tab}$ model is employed. This difference becomes clearer when a region around the highlights is extracted as shown in figure 4.15. From this figure, it becomes clear that the edges of the highlights with the $BRDF_{diff/spec}$ model in place resemble the highlights of the measured luminance map. Surprisingly, the edges of the highlights with the $BRDF_{tab}$ model however are much smoother. Somehow, this was to be expected as the measured BRDF of the GPMCPET also exhibits a specular reflectance which was broader than expected from a pure specular behavior. Consequently, the highlights will also be spread out, causing a smoothing effect on the edges. It has been observed that this apparent angular broadening of the specular peak is an artifact due to convolution effects caused by the measurement instrument itself. In chapter 5 this issue is discussed in more detail.

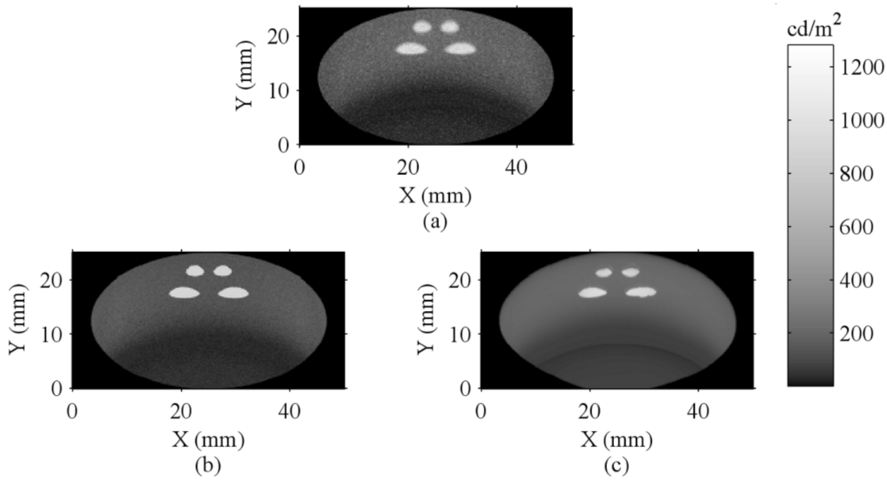

Figure 4.14 – Grayscale luminance images of the optical mixing chamber with the observer position at 55° away from the direction perpendicular to the base plate. (a) and (b) are simulated luminance images obtained with $BRDF_{tab}$ and $BRDF_{diff/spec}$ applied to the surfaces of the optical mixing chamber, respectively. (c) Measured luminance image of the prototyped optical mixing chamber.

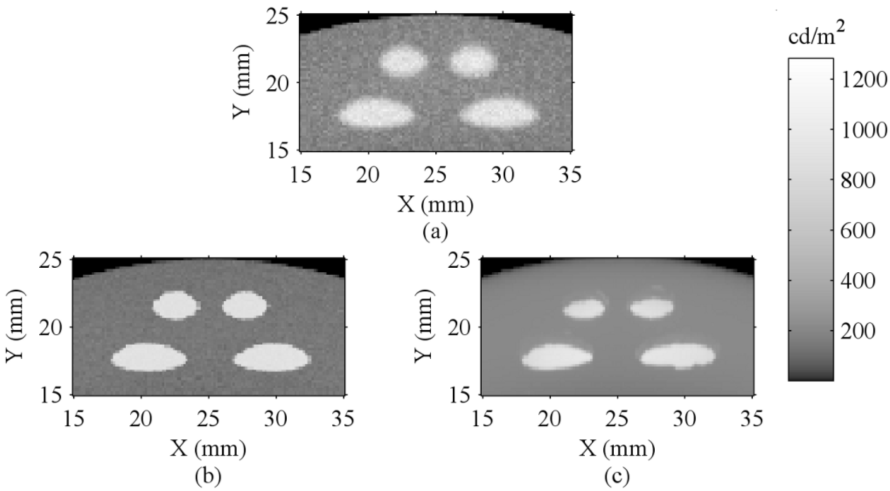

Figure 4.15 – Extracted region of the grayscale luminance images of the optical mixing chamber that include specular highlights at an observer position of 55° away from the direction perpendicular to the base plate. (a) and (b) are simulated luminance images obtained with $BRDF_{tab}$ and $BRDF_{diff/spec}$ respectively applied to the surfaces of the optical mixing chamber. (c) Measured luminance image of the prototyped optical mixing chamber.

A quantitative validation is again performed using the calculated NCC and NRMSE values between the simulated and measured luminance distribution. These calculations are performed on the extracted region around the highlights. The resulting NCC and NRMSE values, and the maximum and mean values of the extracted regions are listed in table 4.2.

Table 4.2: Validation of the simulated luminance maps of the virtual model with the two different BRDF models compared to the luminance image of the prototyped optical mixing chamber expressed by means of the calculated NCC, NRMSE, maximum and mean values of the region around the specular highlights.

Near-field	**NCC (%)**	**NRMSE (%)**	**Max (cd/m²)**	**Mean (cd/m²)**
Measurement	-	-	961	260
$BRDF_{diff/spec}$	88.7	12.8	937	233
$BRDF_{tab}$	89.3	9.5	1140	288

While the NCC and NRMSE values for both models are highly similar and indicate a good correspondence with the measured luminance image, a clear difference is present for the maximum and mean values. While the maximum luminance for the $BRDF_{tab}$ model differs ~18% to the measured maximum, this difference is only ~2.5% for the $BRDF_{diff/spec}$ model. At the same time the mean values for both models differ ~10% to the mean measured value. Taking this into account, it can be concluded that the $BRDF_{diff/spec}$ model is the most accurate description of the surface scattering of the GPMCPET material. Again, deviations from a perfect validation might originate from the fact that the prototyped mixing chamber is not an exact replica of the virtual model, as slight deviations of the geometry can occur. This is even more important with materials exhibiting a specular reflection component as clear, sharp images are formed on the surfaces of the optical mixing chamber, while with more diffuse reflecting materials more details will be lost.

Luminous intensity distributions were simulated with each of the BRDF models applied to the surface of the mixing chamber and compared to the measured LID. As can be seen from figure 4.16, all LIDs resemble each other closely. This was to be expected as the mean luminance values displayed in table 4.2 also showed a high similarity and the luminous intensity towards a single direction can be considered as the spatial integration of the luminance as viewed from that direction.

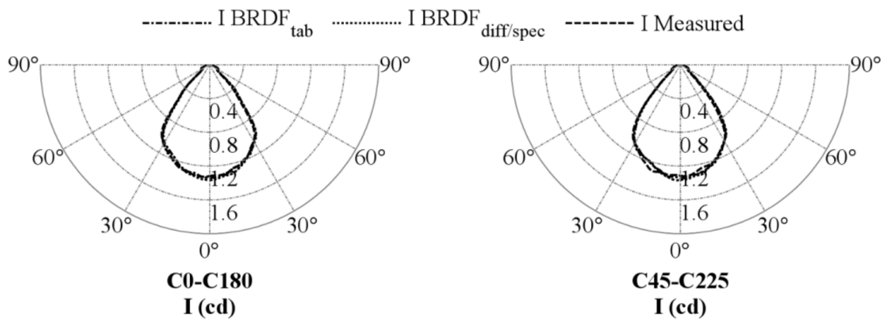

Figure 4.16 – Validation of the LID of the virtual model when applying the 2 different BRDF models and as measured (dashed line). Left: C0-C180 plane, Right: C45-C225 plane.

4.2.5 Final remark

As mentioned earlier, the circular edges of the holes in the base plate of the optical mixing chambers were painted black. This was done, to minimize the effect of light interaction with these surfaces as their optical scattering can't be determined experimentally (i.e. drilling the holes changes the surface scattering behavior).

To highlight the impact of these surfaces, luminance distributions of the optical mixing chamber constructed from the aluminum coated MCPET with the wall surface of the circular holes untreated and painted black, respectively, were measured, as is shown in figure 4.17.

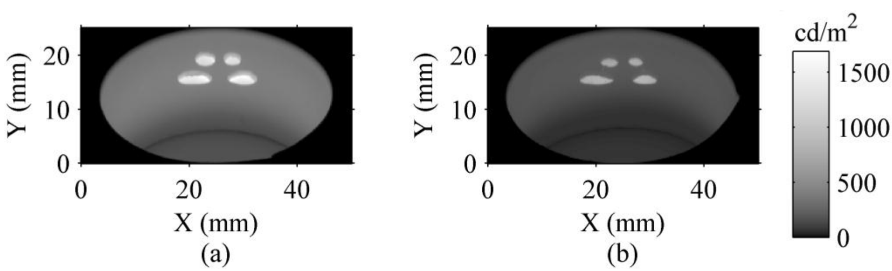

Figure 4.17 – Measured grayscale luminance images of the optical mixing chamber constructed from aluminum coated MCPET with the observer position at 55° away from the direction perpendicular to the base plate, with the wall surface of the circular holes left untreated (a) and painted black (b).

A significant difference between both luminance images is found. The maximum luminance value equals 1690 cd/m² and 858 cd/m² when the wall surface of the circular holes were untreated or painted black respectively. Similarly, the average luminance value equals 226 cd/m² and 96 cd/m² respectively. This indeed shows that such details are important and should be taken into account as discussed in section 4.1.2 and 4.1.4.

4.3 Conclusions

In this chapter it was investigated to what extent the Bidirectional Reflectance Distribution Function (BRDF) of a strongly diffuse and a strongly specular reflective material should be measured and/or modeled in order to accurately simulate far field intensity distributions and near field luminance distributions. The study was based on ray tracing simulations of an optical mixing chamber obtained with a commercially available diffuse reflective material and a high gloss painted reflective material. Various models of the BRDF of each material were considered, characterized by increasing complexity, amount of required input data and measuring time.

Comparison between the simulated and the experimental luminous intensity distribution (LID) showed a high correlation regardless of the BRDF model being applied to the surfaces of the optical mixing chamber for both materials. Indeed, in this configuration, the grade of detail of the description of the specular reflection component does not have a large impact on far field calculations.
However, for the highly diffuse material, the modeling accuracy and elaboration of the specular reflection component, which becomes more prominent for larger angles of incidence, does have an important impact and determines strongly the predictive power of the simulated luminance maps. Although these results were obtained for one particular mixing chamber, the results highlight the importance to model the BRDF accurately even for highly diffuse materials. On the other hand, the model based on the tabulated BRDF values, which was found to be the best model to characterize the highly diffuse material, is sensitive to the accuracy of the measurements. It has been observed that the experimental specular reflection component was angularly wider than expected from a pure specular behavior and consequently the luminance distributions are smoothed/blurred. This angular broadening can be attributed to the finite constraints posed on the tabulated BRDF values to create the BRDF model and to the impact of the instrument function on the BRDF measurements of specular reflecting materials (convolution effect). The latter is further discussed in chapter 5 and a method is presented to minimize these convolution effects.

Keeping these observations in mind, a reduction of the required input data and accordingly the amount of required measurements can be achieved if we know in advance which quantity has to be simulated during simulations of optical systems. If only the LID is of interest then relatively few measurements are necessary to construct a simple BRDF model which is adequate to predict LIDs. On the other hand, more elaborate BRDF measurements and modeling are essential if a high accuracy of the luminance images is required. This is especially important when quantities such as uniformity, contrast and discomfort glare are to be derived from luminance maps.

Chapter 5

Bayesian deconvolution method applied to theoretical and experimental Bidirectional Transmittance Distribution Functions

As discussed in the previous chapters, the reliability of the virtual prototype is strongly dependent on the accuracy of the input data such as the emission characteristics of the light source and the scattering properties of the optical components (reflectors, filters and diffusers). These scattering properties are characterized by the bidirectional scatter distribution function (BSDF). Experimental determination of the BSDF of the materials is however very sensitive to the characteristics of the measuring instrument, i.e., the dimensions of the illumination spot, the detector aperture, etc [Stover, 1995]. These instrumental characteristics are reflected in the instrument function. In order to eliminate the influence of the instrument function the use of a Bayesian deconvolution technique is proposed. A suitable stopping rule for the iterative deconvolution algorithm is presented. The deconvolution method is validated using Monte Carlo ray tracing software by simulating a BSDF measurement instrument and a virtual sample with a known bidirectional transmittance distribution function (BTDF). The Bayesian deconvolution technique is applied to experimental BTDF data of holographic diffusers, which exhibit a symmetrical angular broadening under normal incident irradiation. In addition, the effect of applying deconvolved experimental BTDF data on simulations of luminance maps is illustrated.

5.1 Introduction

Serious efforts have been made to develop accurate and efficient BSDF measurement devices. However, in lack of any standardization, different optical designs have been proposed, each optimized for a specific parameter such as the measurement time, spatial coverage, absolute measurement capability, etc. The intrinsic optical features of each device are reflected in the instrument function, which is obtained by scanning the incident light beam in absence of any sample. The resulting experimental BSDF values can be considered as a convolution of the correct BSDF with the instrument function [Stover, 1995]. In practice, this does not only result in reduced peak values and an angular broadening of the BSDF, it also becomes nearly impossible to compare the BSDF values of the same sample obtained with different measurement devices.

Eliminating the influence of the instrument function on the measured BSDF would be beneficial to domains where accurate BSDF data are necessary. Among others, these include: photorealistic rendering [Li et al., 2006], characterizing ground surfaces for remote sensing [Combes et al., 2007], material appearance characterization [Leloup et al., 2012], luminaire design, etc.

The optical components of luminaires often exhibit macrostructures (e.g. a hammerscale reflector) with a spatial periodicity in the range of 5 mm or even more. In order to obtain a relevant average BSDF value for this kind of surface, a wide illumination area on the sample must be used. If absolute BSDF values are to be measured, a large detector aperture cannot be avoided. As a consequence, the instrument function becomes angularly wider and the convolution effect becomes particularly important.

To limit the effect of the instrument function, without physically altering the optical design of the measurement device, a deconvolution can be applied to the measured BSDF. A matrix-based deconvolution applied to theoretical BSDF data has been proposed by Ferrero et al. [Ferrero et al., 2011]. In ideal conditions, this deconvolution procedure perfectly recovers the true BSDF from the theoretical data. However, when noise is present, the matrix-based deconvolution introduces noise artifacts and negative BSDF values in the deconvolved BSDF. Therefore, the matrix-based method seems not suitable for the deconvolution of experimental data.

A Bayesian deconvolution method [Bishop, 2007; Richardson, 1972] which does not suffer from the drawbacks encountered with the matrix-based deconvolution is proposed in this thesis. The Bayesian deconvolution algorithm is typically used in image analysis to eliminate blur caused by camera movement [Fergus et al., 2006; Joshi et al., 2010], and to enhance the resolution and accuracy of imaging devices [Bertero et al., 2009; Bowsher et al., 1996]. Recently, the technique was also employed to enhance the accuracy of measured spectra [Eichstädt et al., 2013; Gardner, 2013].

In a first step, the goniospectroradiometer developed at the Light&Lighting Laboratory [Leloup et al., 2008] is modeled in ray tracing software. A validation of the model is achieved by comparing the experimental instrument function with the instrument function of the simulation model. Next, the experimental BTDF of a virtual sample with a known BTDF is simulated. The Bayesian deconvolution method is then applied to recover the original data. The iterative deconvolution algorithm is optimized through the introduction and validation of an early stopping rule [Llacer and Veklerov, 1991; Llacer and Veklerov, 1989]. Afterwards, the approach is applied to real experimental BTDF data of holographic diffusers which exhibit a symmetrical angular broadening under normal incident irradiation. These diffusers become more and more important in modern luminaire design and are often used to limit discomfort glare. Finally, the impact of applying the deconvolution technique is illustrated on a simulated luminance map of a luminaire incorporating one of these holographic diffusers.

5.2 Bidirectional Scatter Distribution Function

$BSDF_{\mathrm{e}}$, as a ratio of infinitesimals, can never be measured directly. Real measurements involve non-zero intervals of the parameters, and hence can yield only average values over those intervals [Nicodemus et al., 1977]. To determine $BSDF_{\mathrm{e}}$ of opaque, translucent or transparent materials from measurement data, the American Society for Testing and Materials (ASTM) has proposed the following practical formula [ASTM E2387, 2005]:

$$BSDF_{\mathrm{e}} = \frac{\Phi_{\mathrm{e},\lambda,\mathrm{s}}}{\Phi_{\mathrm{e},\lambda,\mathrm{i}}\Omega_{\mathrm{s}}\left|\cos\theta_{\mathrm{s}}\right|}\left[\frac{1}{\mathrm{sr.nm}}\right] \qquad (5.1)$$

with $\Phi_{\mathrm{e},\lambda,\mathrm{s}}$ and $\Phi_{\mathrm{e},\lambda,\mathrm{i}}$ the scattered radiant flux towards the detector and the incident radiant flux on the sample, respectively, Ω_{s} being the solid angle of the detector aperture.

As the practical formula indicates, one major source of convolution can be identified as the detector aperture convolution (i.e. averaging over Ω_{s}). This averaging will result in a decrease of the peak value of the signal being measured. Another source of convolution is the finite size of the incident light beam which; in combination with the finite solid angle of the detector, will result in an angular broadening of the signal being measured.

5.3 Bayesian deconvolution

Any measurement of a scattered power W undergoes a convolution with the instrument function S of the measurement device. An ideal measurement device has a unit impulse function as instrument function. Any deviation of the instrument function from the unit impulse function results in a convolved signal H, denoted by $H = W * S$, with $*$ the convolution operator.

A Bayesian deconvolution relies on the theorem of Bayes and can be expanded into a nonnegative constrained iterative deconvolution algorithm, often referred to as the Richardson-Lucy algorithm (RL) [Richardson, 1972]. The nonnegative constraint ensures that the deconvolved signal always remains positive, which is a desired feature when deconvolving BSDF measurements. If no noise is present in the measured signal H and in the measured instrument function S, this algorithm will converge and will return the original signal W correctly. However when noise is present in H and S, which is always the case when using experimental data, the algorithm will converge to a solution W' which exhibits noise artifacts. In image processing, these artifacts are referred to as “ringing” [Shan et al., 2008; Yuan et al., 2007]. To prevent this type of overfitting, an early stopping rule [Llacer and Veklerov, 1991; Llacer and Veklerov, 1989] for the iterative deconvolution algorithm has to be implemented.

It should be noted that the Bayesian deconvolution method is not directly applied to $BSDF_{\mathrm{e}}$ but to $\Phi_{\mathrm{e},\lambda,\mathrm{s}}$ data. Afterwards, the BSDF is calculated using equation 5.1 and scaled to ensure energy conservation. This scaling factor is found by ensuring that the Total Integrated Scatter (TIS) [Stover, 1995] with or without deconvolution remains the same, with the TIS of a symmetric BSDF (symmetry around the normal of the sample) defined by:

$$\mathrm{TIS} = 2\pi \int_{\theta_{\mathrm{s}}=0}^{\pi/2} BSDF(\theta_{\mathrm{s}}) \cos(\theta_{\mathrm{s}}) \sin(\theta_{\mathrm{s}})\ \mathrm{d}\theta_{\mathrm{s}} \tag{5.2}$$

5.4 Bayesian deconvolution applied to simulated BTDF data

5.4.1 Modeling a BSDF measurement device

In experimental conditions, it is impossible to know to what extent the deconvolved BSDF resembles the “true” BSDF of the material. Therefore simulating a BSDF measurement allows for a comparison between the target BSDF and the deconvolved BSDF.

In this chapter, the sample has been illuminated with a circular collimated light bundle with a diameter of 14 mm. Characterizing the 14 mm wide collimated light bundle with an infinitesimally small detector aperture would result in a unit pulse centered around $\theta_{\mathrm{s}} = 0°$ with a width of $\arctan(14/886) \approx 0.9°$, i.e., the incident light beam convolution. Inversely, using a very narrow incident laser beam measured with the 25.4 mm wide circular detector aperture would result in a unit pulse centered around $\theta_s = 0°$ with a width of $\arctan(25/886) \approx 1.6°$, i.e., the detector aperture convolution. In result, the final instrument function of the device is mainly the convolution of both the light beam and detector aperture convolution.

A model of the measurement device described in section 1.3.2, was implemented in TracePro®. The model consists of a light source modeled as a collimated grid source represented by 10^6 rays with a wavelength of 550 nm randomly distributed over a circular area with a diameter of 14 mm. The detector aperture is modeled as a circular surface with a diameter of 25 mm located at a distance of 886 mm from the sample. A simulated instrument function ($Ssim$) was compared with the experimentally determined instrument function of the BSDF measurement device ($Sdev$). Both have been obtained by literally or virtually scanning the illuminating light beam in one plane using an angular step of 0.1°, which is small enough to sample the instrument function correctly. A good resemblance between the simulated and measured instrument function is achieved, as can be seen in figure 5.1.

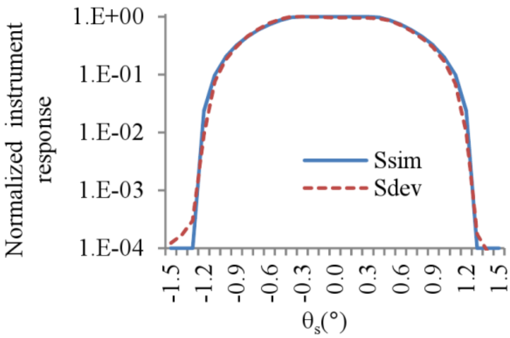

Figure 5.1 – Normalized measured ($Sdev$ - dashed line) and simulated ($Ssim$ - solid line) instrument function, obtained with an angular step of 0.1°.

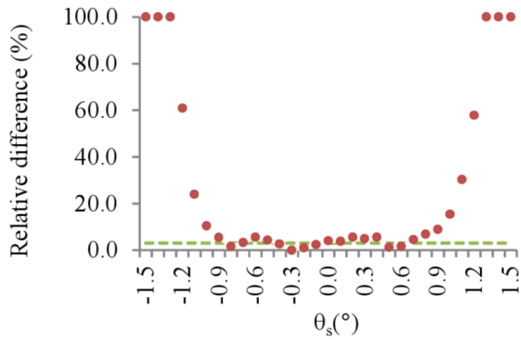

Figure 5.2 – Relative difference between $Sdev$ and $Ssim$ (dots) and uncertainty budget of the experimental BSDF measurement setup (dashed line).

Figure 5.2 displays the relative difference, $Diff_{rel}$, between $Sdev$ and $Ssim$ as calculated by:

$$Diff_{rel} = \frac{|\,Sdev - Ssim\,|}{max(Sdev, Ssim)} \tag{5.3}$$

As the light beam in the experimental setup is not perfectly collimated, a relative difference of up to 100% is present at the edges of the instrument function. However, around the center of the instrument function an acceptable relative difference is found compared to the uncertainty budget of the BSDF measurement device which is around 3%. The varying relative differences in this region occur as the uniformity of the light beam in the experimental setup is not perfect compared to the simulated light beam. In general a good agreement is found, validating the measurement device ray tracing model.

5.4.2 Defining virtual BTDFs

As a next step, a virtual sample was introduced into the model of the measurement instrument. A series of theoretical BTDFs, characterized by different values for the Full Width at Half Maximum (FWHM), under normal incident lighting based on the Phong model [Dutré et al., 2006; Phong, 1975] were assigned to this sample. To this end, the Phong model, originating from computer graphics and typically used in reflection, was extended to transmission. The BTDFs are symmetric around the regular transmission direction and have a TIS of 1. Three specific BTDFs (W_{SD1}, W_{SD2} and W_{SD3}) are implemented described as:

$$BSDF_{\mathrm{e}} = B \cdot \cos^{n}(\theta_{\mathrm{s}}) \left[\frac{1}{\mathrm{sr}} \right] \quad (5.4)$$

with $n > 0$ a parameter which controls the FWHM. B is a scaling factor to ensure that the TIS equals 1 and can be calculated as given by:

$$\begin{aligned} B &= \left[2\pi \int_{\theta_{\mathrm{s}}=0}^{\pi/2} \cos^{n}(\theta_{\mathrm{s}}) \cos(\theta_{\mathrm{s}}) \sin(\theta_{\mathrm{s}}) \mathrm{d}\theta_{\mathrm{s}} \right]^{-1} \\ &= \frac{1 + n/2}{\pi} \end{aligned} \quad (5.5)$$

If n increases, the FWHM will decrease and B will increase. The parameters for W_{SD1}, W_{SD2} and W_{SD3} are given in table 5.1.

Table 5.1: BTDF model parameters for the modified Phong model of 3 virtual diffusers SD1, SD2 and SD3. B denotes a scaling factor to ensure a TIS of 1, while *n* denotes an exponent determining the FWHM.

BTDF	B	n	FWHM(°)
W_{SD1}	598.9	3761	2.2
W_{SD2}	2897.6	18 204	1
W_{SD3}	11 589	72 815	0.5

To evaluate the performance of the RL algorithm on more complex functions, a fourth BTDF (W_{SD4}) was defined by combining three Gaussian functions:

$$\begin{aligned} W_{\mathrm{SD4}}(\theta_{\mathrm{s}}) &= BSDF_{\mathrm{e},\lambda}(\theta_{\mathrm{s}}) \\ &= \frac{596.08}{\cos(\theta_{\mathrm{s}})} \{ \exp(-2(\theta_{\mathrm{s}} 180/\pi)^{2}) + \frac{1}{2} \exp(-8\left[(\theta_{\mathrm{s}} 180/\pi) - 2\right]^{2}) \\ &+ \frac{1}{2} \exp(-8\left[(\theta_{\mathrm{s}} 180/\pi) + 2\right]^{2}) \} \end{aligned} \quad (5.6)$$

The parameters of this function are chosen to ensure a partial overlapping of the three Gaussian functions and to obtain a TIS of 1.

5.4.3 Deconvolving the simulated BTDFs

The 4 virtual samples (SD1 to SD4) were introduced into the virtual instrument. A collimated incident beam perpendicular to the sample was adopted and the flux received by the detector aperture was simulated. In the simulation, an angular range of detector positions (θ_s) was considered with an angular step of 0.1°. For each angular position, a collimated beam consisting of 10^6 rays was simulated. These rays interact with the sample surface upon intersection according to the defined BTDF. The scattered incident flux captured by the detector is stored for each angular position, from which an experimental BTDF is calculated according to equation 5.1, and which is described as H_{SD1} to H_{SD4}.

Afterwards, the RL algorithm is applied to H_{SD1} to H_{SD4} using the simulated instrument function and applying 10^4 iterations *i*. As can be seen from figure 5.3, the impact of the instrument function is more important for very sharp BTDFs. Furthermore, the deconvolved BTDFs $W'_{SD1}(i=10^4)$ to $W'_{SD4}(i=10^4)$ are distorted with respect to the target values W_{SD1} to W_{SD4}, respectively. The distortion seems to be dependent on the shape of the BTDF. It was also observed that distortions become more prominent when using more iterations because of statistical noise present in both the Monte-Carlo ray tracing simulations of the instrument function and H_{SD1} to H_{SD4}.

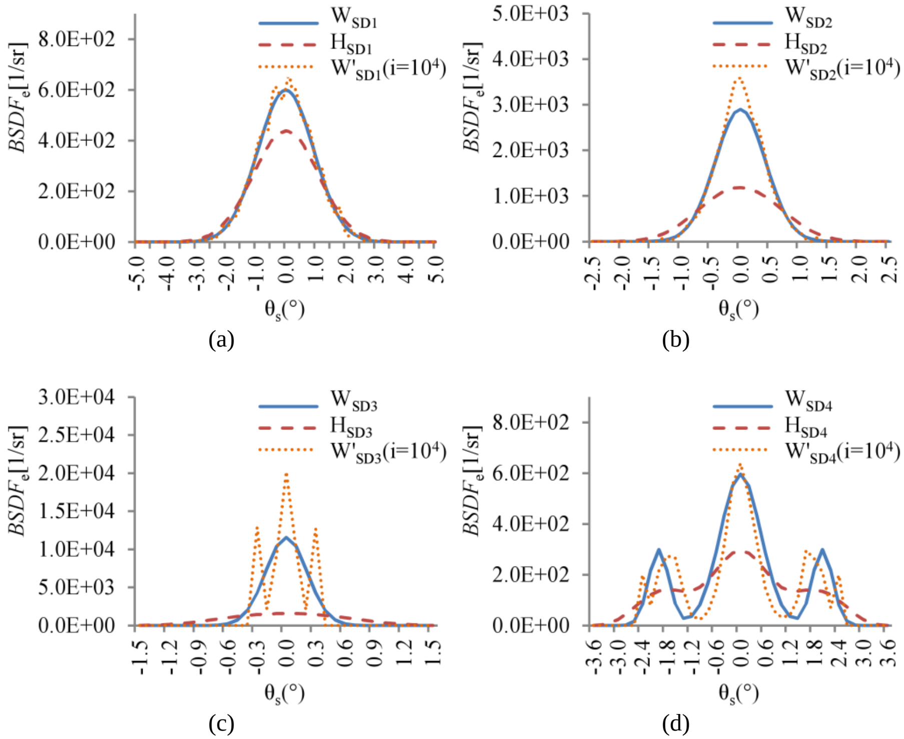

Figure 5.3 – The theoretical BTDF W (solid line), the simulated BTDF H (dashed line) and the deconvolved BTDF $W'(i=10^4)$ (dotted line) at 550 nm after 10 000 iterations for sample SD1 (a), SD2 (b), SD3 (c) and SD4 (d).

5.4.4 Early stopping rule

To counter the effect of distortion dominating the deconvolved BTDF, an early stopping rule is implemented which aborts the iterative algorithm at a certain iteration. The stopping rule is based on an error function $E(i)$ given by:

$$E(i) = \left[\frac{1}{N} \sum_{t=1}^{N} \left(\frac{Hc_t(i) - H}{Hc_t(i)} \right)^2 \right]^{1/2} \tag{5.7}$$

with N the number of data points in the convolved signal, $Hc_t(i) = W'(i) * Ssim$, which is the result of the convolution of the deconvolved signal $W'(i)$ at each iteration i and the simulated instrument function $Ssim$. As the error function does not use the target signal W it can also be applied to the experimental data where W is not known. Basically $E(i)$ is a weighted root mean square deviation (RMSD) between $Hc_t(i)$ and H. Figure 5.4 displays the normalized error functions for H_{SD1} to H_{SD4} for iterations 1 to 200. The last iteration for which $E(i)$ exhibits a minimum and before disturbances from noise amplifications become present, is chosen as the best stopping iteration. The best stopping iteration i for the BTDFs H_{SD1} to H_{SD4} are 3, 14, 56 and 43 respectively.

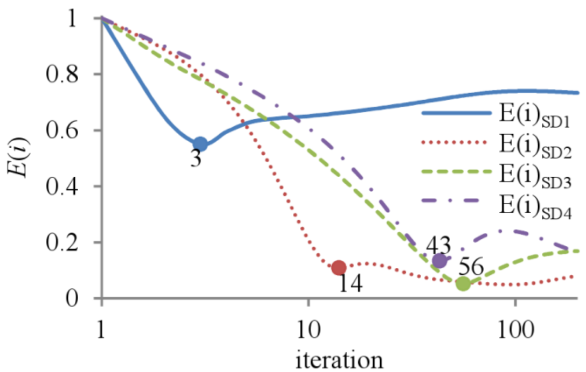

Figure 5.4 – Normalized error function $E(i)$ evaluated for iteration 1 to 200 for BTDF H_{SD1} to H_{SD4}. The best stopping iteration of $E(i)_{SD1}$ to $E(i)_{SD4}$ is 3, 14, 56 and 43, respectively.

The effect of applying this early stopping rule can be seen in figure 5.5. With the implemented stopping rule, the deconvolved BTDFs $W'_{SD1(i=3)}$, $W'_{SD2(i=14)}$, $W'_{SD3(i=56)}$ and $W'_{SD4(i=43)}$ show a much higher resemblance to the target values of W_{SD1} to W_{SD4}, respectively. This shows that the deconvolution method with inclusion of the stopping algorithm is able to successfully correct for the impact of the instrument function. The small deviations which are still present are inevitable because the deconvolution algorithm is unable to perform a perfect reconstruction due to statistical noise in the data generated by the Monte-Carlo ray tracing simulations.

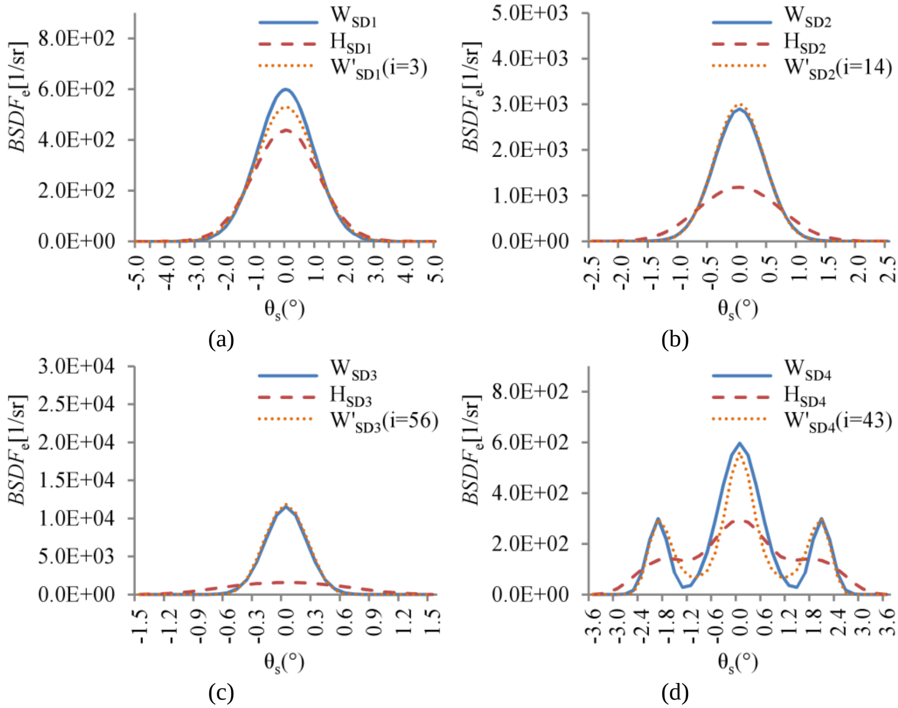

Figure 5.5 – The theoretical BTDF W (solid line), the simulated BTDF H (dashed line) and the deconvolved BTDF $W'(i)$ (dotted line) at 550 nm for sample SD1 (a), SD2 (b), SD3 (c) and SD4 (d), after 3, 14, 56 and 43, iterations respectively.

5.5 Bayesian deconvolution applied to experimental BTDF data

So far, the RL algorithm and the implemented stopping rule have only been applied to simulated data. Real BTDF measurements were performed on 2 holographic diffusers [Sheng, 2006] designed to broaden a collimated beam of light and marked as a 0.5° and a 5° diffuser, respectively. These diffusers have become very popular in luminaire design because of their high transmission efficiencies and the ability to diffuse light in a controlled way. The 0.5° diffuser exhibits a very narrow symmetrical angular broadening (0.5° FWHM) compared to the instrument function (FWHM ≈ 1.8°) while the 5° diffuser has a wider symmetrical angular broadening (5° FWHM).

BTDF measurements of both holographic diffusers illuminated by a circular collimated normal incident beam (diameter 14 mm) were performed with several detector aperture sizes, denoted as d*x* with *x* the numerical detector aperture diameter in mm. The angular step of the BTDF measurements was 0.1°. The instrument function for each detector aperture size, d25 to d16, was also measured with an angular step of 0.1°. The corresponding normalized instrument functions S_{d25} to S_{d16} are shown in figure 5.6.

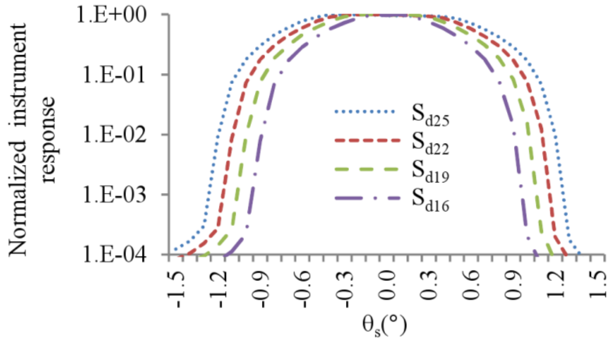

Figure 5.6 – Normalized instrument functions S_{d25} to S_{d16} for each detector aperture size, d25 to d16, measured with an angular step of 0.1°.

The measured BTDFs were deconvolved using the RL algorithm with the early stopping rule and the corresponding instrument function.

5.5.1 Holographic diffuser 0.5°

The deconvolved BTDF and non-deconvolved BTDF (perpendicular incident light) for the 0.5° diffuser, denoted by $W'_{0.5d25}$ to $W'_{0.5d16}$ and $H_{0.5d25}$ to $H_{0.5d16}$ respectively, are presented in figure 5.7. After deconvolution, the average peak values have become much higher (up to 166% increase). Theoretically, the real BTDF values of a material must be independent of the detector aperture and instrument function. To this extent, the variation of the peak BTDF values and FWHM values has been evaluated by the coefficient of variation (CV), defined by:

$$CV = \frac{100}{\bar{x}}\left[\frac{1}{N-1}\sum_{i=1}^{N}(x_i-\bar{x})^2\right]^{1/2} \tag{5.8}$$

with x a dataset with N values and $\bar{x}$ the mean value of dataset x.

The CV of the 4 peak values from the non-deconvolved BTDFs equals 24% while this becomes 6% after deconvolution. Likewise, the CV of the 4 FWHM values from the non-deconvolved BTDFs equals 15% while this decreases to 5% after deconvolution. These are excellent results bearing in mind that the total uncertainty budget of the measurement device can amount up to 2.4%. Furthermore, the sample had to be realigned after every measurement to measure the instrument function.
This study illustrates the importance of correcting the experimental values, especially when the results obtained with several measuring instruments are compared.

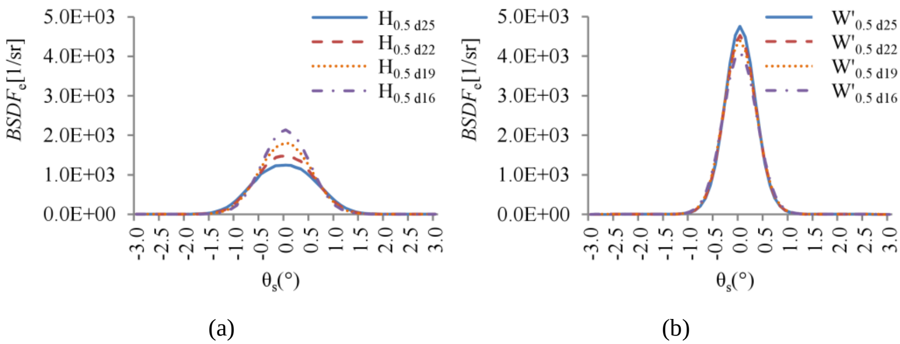

Figure 5.7 – (a) Measured BTDF $H_{0.5d25}$ to $H_{0.5d16}$ at wavelength 550 nm and (b) deconvolved BTDF $W'_{0.5d25}$ to $W'_{0.5d16}$ at wavelength 550 nm of a 0.5° diffuser.

To obtain the best stopping iteration, the previously described error function *E(i)* was evaluated at iteration 1 to 200 and is plotted in a normalized form in figure 5.8 for each of the detector aperture sizes. The best stopping iteration is 23, 16, 11 and 7, for d25 to d16, respectively. Analysis of the error functions reveal that all error functions resemble each other with the only exception being the minima which are being shifted towards a lower iteration number as the detector aperture size decreases. Indeed as the detector size decreases, the instrument function becomes narrower. This results in less convolution effects and in turn, less iterations are necessary to reconstruct the original signal.

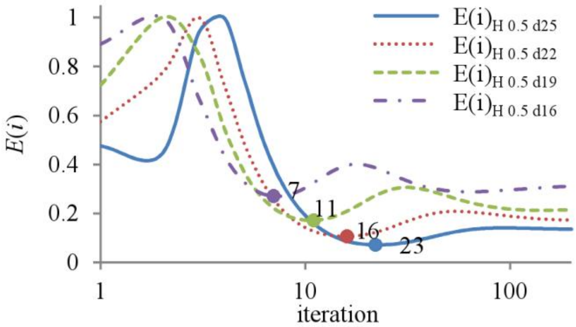

Figure 5.8 – Normalized error function *E(i)* evaluated for iteration 1 to 200 of the deconvolution algorithm applied to the measured BTDFs $H_{0.5d25}$ to $H_{0.5d16}$. The best stopping iteration of $E(i)_{H0.5d25}$ to $E(i)_{H0.5d16}$ is 23, 16, 11 and 7, respectively.

5.5.2 Holographic diffuser 5°

Similar to the 0.5° diffuser, BTDF measurements under normal incident light of the 5° diffuser were performed with the 4 different detector apertures (H_{5d25} to H_{5d16}). The resulting deconvolved BTDFs (W'_{5d25} to W'_{5d16}) are presented in figure 5.9. As expected, performing a deconvolution on the measured BTDFs becomes less relevant as the angular width of the instrument functions is relatively narrow compared to the angular width of the BTDF. This becomes also evident from the error function as it exhibits a minimum at the first iteration for the d16, d19 and d22 detector sizes and at the second iteration for the d25 detector size. Indeed, as the instrument function becomes angularly wider, a deconvolution procedure becomes necessary [Ferrero et al., 2011].

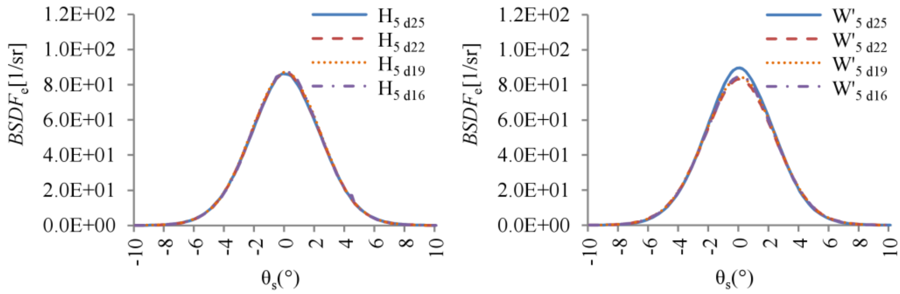

(a) (b)

Figure 5.9 – Measured BTDF H_{5d25} to H_{5d16} at wavelength 550 nm (a) and deconvolved BTDF W'_{5d25} to W'_{5d16} at wavelength 550 nm (b) of a 5° diffuser.

5.6 Impact on luminance distributions

If the BSDF would contain a pure specular component, as it was the case for the reflecting material presented in section 4.2, a deconvolution would not be possible. An infinite amount of iterations would be necessary to obtain an impulse function. Moreover, as the signal is discretized this is not possible due to the finite angular step resolution of the measured signal. Therefore, in order to demonstrate the importance of using deconvolved BTDF data in luminance simulations, a simple luminaire which incorporates the 0.5° diffuser has been modeled as shown in figure 5.10. The luminaire consists of a LED inside a parabolic reflector, covered by the diffuser. The LED is modeled as a square lambertian emitting surface source with a luminous flux of 30 lm positioned at the focus of the parabolic reflector. The inner surface of the parabolic reflector is an 80% specular reflecting surface. A thin plate representing the 0.5° diffuser is positioned on top of the parabolic reflector.

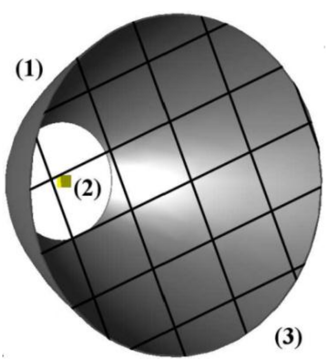

Figure 5.10 – 3D model of a simple luminaire which includes a holographic diffuser. (1) parabolic reflector, (2) square lambertian emitting surface source and (3) thin plate representing the 0.5° diffuser positioned on top of the parabolic reflector (square hatch pattern).

The luminance distribution is generated for an observer positioned at a distance of 2.0 m from the luminaire, on the central axis of the luminaire. The luminance map grid is composed of 100 by 100 square pixels of 0.2 mm width. For each pixel, 10^4 rays from the observer's position towards the luminance map grid are traced. Luminance distributions of the luminaire are simulated using both the non-deconvolved BTDF $H_{0.5d25}$ and the deconvolved BTDF $W'_{0.5d25}$. The simulated luminance distributions are denoted as L_H and L_W, respectively, and are visualized in figure 5.11.

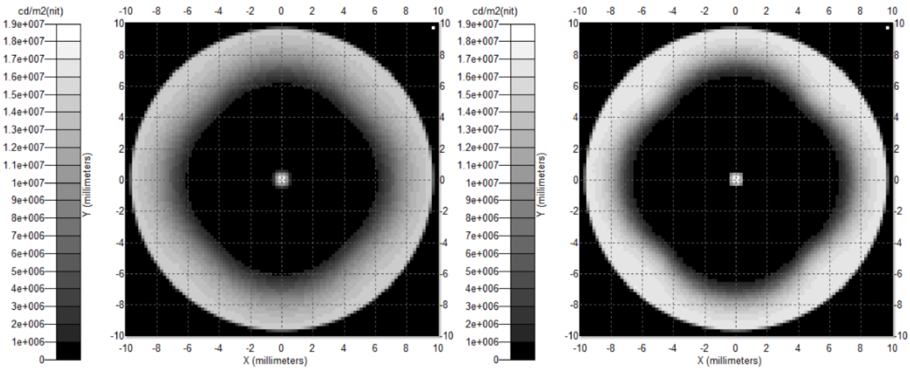

(a) (b)

Figure 5.11 – Grayscale luminance maps of a luminaire which incorporates a 0.5° diffuser using $H_{0.5d25}$ (a) and the deconvolved values $W'_{0.5d25}$ (b) as BTDF.

The effect of using the deconvolved data is visually perceptible: one can perceive the luminance map L_H as a blurred version of the luminance map L_W. Numerically, maximum and average luminance values of $1.69\times10^{7}\,(\text{cd.m}^{-2})$ and $4.71\times10^{6}\,(\text{cd.m}^{-2})$, respectively, are obtained with the non-deconvolved data L_H. These values are clearly lower (8% and 9% respectively) than the values obtained from L_W.

5.7 Conclusions

Experimental determination of the BSDF of a material can be largely influenced by the instrument function of the measurement device. This can have a serious impact on the accuracy of the experimental BSDF, especially for near specular materials showing a low angular scattering compared to the angular width of the instrument function.

In this chapter, a method based on an iterative Bayesian deconvolution algorithm combined with an early stopping rule has been presented. This approach has been validated using Monte Carlo simulations in which a BTDF measurement of a virtual diffuser with known BTDF was simulated. As a practical example, the method was also applied to experimental BTDF measurements of holographic diffusers. By varying the detector aperture, the impact of 4 different instrument functions was investigated. As expected, both the peak and FWHM values of the experimental BTDFs were strongly dependent on the instrument function. After deconvolution, the impact of the instrument characteristics on the BTDF was drastically reduced. This indicates that deconvolution is indeed necessary in order to compare the BSDF of the same material, yet measured on different instruments. This is particularly important as long as BSDF measurements methods are not standardized and a wide variety of BSDF measurement instruments are being used.

Chapter 6

Conclusions

6.1 General conclusions

The need to investigate the luminance distributions of lit luminaires during the development stage is being acknowledged more and more by the industry as luminance maps of a luminaire can yield important information to the optical designer. Luminance distributions simulated during the development stage can predict the general appearance of the active luminaire and provide objective information to assess parameters such as contrast, uniformity and discomfort glare.
Indeed, discomfort glare evaluation should be based on luminance maps for luminaires showing a non-uniform luminance distribution.

Light sources can be characterized at best using ray files obtained with near-field goniophotometry. However, using the traditional ray tracing techniques, it is currently not possible to simulate luminance distributions of a luminaire incorporating such a light source description due to the nature of a ray file.

Two distinct methods were presented to enable the simulation of luminance distributions of light sources/luminaires described by a ray file.
First, a feasibility study of a brute-force forward ray tracing approach was presented. While being straightforward, this method requires large simulation times and the accuracy of the resulting luminance distributions is not that high. However, it was shown that digital enhancement techniques are able to increase the accuracy to some extent. The main drawback of the brute-force method is the huge amount of rays which have to be traced each time the design is changed in order to reflect these changes in the luminance distributions. However, this method has the advantage that once all the calculations are done, luminance distributions can be calculated for any observer position almost in real time.

The second method consists of the geometrical modeling of the light source and the sampling of the corresponding ray file into a set of luminous intensity distributions (LIDs). The generated LIDs can easily be imported in any ray tracing software and applied to surfaces in order to create a set of surface sources. This enables the simulation of luminance maps through the technique of reverse ray tracing (eye tracing), a feature which is almost always available in standard ray tracing software. The major advantage of this technique is that only a limited amount of rays have to

be traced in order to simulate accurate luminance maps. The ray file sampling method also has the benefit of drastically reducing disk space requirements to characterize the near-field of a light source. In addition, the light source model created with this method is able to generate as many rays as necessary compared to ray files which always have a fixed amount of rays upon creation.
This new method has been validated by the good agreement between measured and simulated luminance distributions for both planar and non-planar (hemispherical) light sources. Finally, it was shown that the generated models can also be used for the optical design of optics located in close proximity of the light source.

Not only the light source, but also the geometry and the optical properties of the materials surrounding the light source, influence the final luminance distributions of the whole optical system. A prototype of an optical mixing chamber was created in order to investigate the influence of the accuracy of the surface scattering properties on the resulting luminance distributions. Several input models were created based on both integrated reflectance and surface scattering measurements. Luminance distributions were simulated for each of the models and compared to experimental results. For materials that exhibit a large diffuse scattering component, it was found that even a relatively small specular component already drastically influences the luminance distribution. For such materials the best agreement between measured and simulated luminance distributions will be obtained if the surface scattering is modeled very accurately using tabulated scattering data. On the other hand, materials that exhibit a clear specular component are best modeled by explicitly defining this specular component apart from the other surface scattering characteristics. This is because BRDF values of specular materials can strongly be influenced by the instrument function of the measuring instrument.

Due to the lack of standardization of a surface scattering measurement device, a wide variety of measurement setups exist. As such, large variations in surface scattering data of the same sample obtained on different measurement devices are possible. They are mainly due to the impact of the instrument signature on the measured data. To limit the angular broadening due to the instrument signature, a deconvolution technique was applied. With this technique, scatter data are less contaminated by the particular measuring instrument and the quality of the data can be greatly improved The effect of the deconvolution was also reflected in the corresponding luminance distributions. It has become clear that this deconvolution should be considered when luminance distributions of luminaires that incorporate near specular materials are to be simulated.

In conclusion, the main contributions presented in this doctoral thesis to the state-of-the-art can be summarized as follows:

- It is now possible to simulate highly accurate luminance distributions of an optical system when the light source is characterized as a ray file – something which was simply not possible nor attempted before.

- It was shown that optical surface scattering of materials must be modeled as accurate as possible in order to enable the simulations of accurate luminance distributions, in contrast to the rather soft requirements when simulating luminous intensity distributions.

- For the first time, a deconvolution technique was successfully applied on both theoretical and experimental optical surface scattering data in order to reduce variations induced by the measurement device itself.

6.2 Future research

In this doctoral research, methods to simulate luminance distributions from ray files are presented. In addition, the impact of the BRDF of materials incorporated in luminaires on the simulated luminance distributions is investigated. However, there is room for improvement with regard to the ray tracing software used for optical design and especially on the metrology part concerning the measurement of ray files and BSDFs.

During this doctoral research, it has become clear that, even though computers nowadays have tremendous computing capacities, some practical limitations are imposed on the presented ray file sampling techniques. One of the biggest obstacles during ray tracing simulations remains the large simulation time needed when simulating luminance distributions of a light source/luminaire if a large amount of surface sources is used. As discussed in chapter 3, this is mainly due to the ray tracing algorithm implemented in the commercial ray tracer. Surprisingly, while the ray tracing algorithms in computer graphics evolve and become more and more refined and tuned to improve the speed of ray tracing, these innovations are often not implemented or lag behind in ray tracing packages used for optical design. For example, in computer graphics many of the ray tracing algorithms are no longer executed on the central processing units (CPUs) of a computer but distributed to a large number of graphical processing units (GPUs) where calculations are performed in parallel [Nickolls and Dally, 2010]. If this approach would be implemented in ray tracers for optical design, this could drastically reduce the required simulation time and allow for more complex and detailed models. As such, simulations that are now impractical could become feasible. To this end, an explorative study will be carried out at the Light&Lighting Laboratory during a Professional Bachelor thesis to investigate the possibilities of the Nvidia OptiX framework [Parker et al., 2010].

As briefly discussed in chapter 3, ray files measured using a near-field goniophotometer measurement device can exhibit deviations from the true light distribution due to the limited dynamic range of the camera. This is something which was already acknowledged by Ashdown [Ashdown, 1993]. During the doctoral research however, it was found that this dynamic range problem is not limited to the camera system alone. In fact, this problem becomes more dramatic as the camera captures relative luminance distributions. These luminance distributions are afterwards converted to absolute luminance distributions using a scaling factor obtained through the total luminous flux captured by a photometer as discussed in chapter 1. This photometer has a larger dynamic range than the camera and as such, the photometer might record illuminance values at positions where the camera does not or barely detect any signal. As a result, the scaling factor to convert the relative values to absolute luminance distributions will be wrong, which in turn results in an erroneous ray file.
A possible solution to this could be to measure the near-field repeatedly with different integration times. Afterwards these measurements can be combined by swapping saturated pixels from each relative luminance image with non-saturated pixels from another non-saturated relative luminance image. This would of course increase the amount of time needed to measure the near-field, however this would solve the dynamic range problem.

It must be noted that all simulations mentioned in this study were performed at only one wavelength. As such, no spectral or color information is available in the ray files and corresponding luminance distributions. In order to fully characterize a light source and simulate true luminance distributions including spectral information, it is necessary to enable the measurement of spectral ray files. Rykowski [Rykowski, 2011] describes several ways to obtain spectral ray files from near-field goniophotometer measurements by altering the near-field goniophotometer. One proposed solution is to attach a spectrometer in the far-field of the light source during a measurement scan. This allows angularly dependent spectral information to be included in the ray file. However to include spatially dependent spectral information in the ray file, the spectrum measured at each angular position must be combined with tristimulus near-field goniophotometer measurements (colorimetric camera).
The best approach however to perform spectral near-field goniophotometer measurements is to consider the use of a hyperspectral camera. While this was previously deemed impractical, because of the large integration times needed to

acquire a hyperspectral image [Rykowski, 2011], recently a state-of-the-art compact hyperspectral camera with very low integration times was presented [Geelen et al., 2013]. At this moment the hyperspectral camera operates in the wavelength region of 600 to 1000 nm although Geelen et al. are confident this can be altered without substantial efficiency loss to a region of around 400 to 800 nm. This would allow the measurement of spectral ray files of luminaires and light sources using a near-field goniophotometer setup by mounting the hyperspectral camera to the detector bench. Such a measurement setup would be ideally suited to generate spectral ray files from which true luminance distributions could be simulated that contain colorimetric information. To this end, the spectrum must be defined with a wavelength interval of 5nm over the region of 380 to 780nm [CIE 167, 2005]. Furthermore, the brightness of light emitting surfaces as perceived by humans is not only dependent on its luminance but also on its colorfulness or saturation, an effect referred to as the Helmholtz-Kohlrausch effect [Wyszecki and Stiles, 1982; Hunt, 1998]. At this moment a doctoral thesis that investigates the perceived brightness of self-luminous colors is being performed at the Light&Lighting Laboratory [Withouck et al., 2013]. When this research is combined with the sampling technique applied to spectral ray files it would become possible to accurately predict how bright a light source is perceived through ray tracing simulations.

While the absolute spectral BSDF measurement device available at the Light&Lighting Laboratory is very versatile, has a high dynamic range and can be adjusted with relative ease to accommodate for specific measurement requirements, some drawbacks do however arise when characterizing a full 3D BSDF. A full 3D scan of a BSDF at one angle of incidence is nearly impossible to realize as the integration times can become very large for near-grazing angles. One could sacrifice the high dynamic range and enforce a fixed integration time but this would result in a less accurate measurement especially for surfaces that exhibit a very low diffuse component. One solution to this might be to mount a photometer, with a baffle to limit the field of view, to the detector bench. While spectral information will be lost, the dynamic range of a photometer at a fixed integration time is already larger than the dynamic range of a CCD in combination with neutral density filters and various integration times. If the material under investigation does not exhibit strong spectral dependent scattering, such a measurement setup would be a practical alternative to measure a full 3D BSDF in a relatively short time. As more data points will be available, no elaborate interpolation scheme has to be defined in order to generate models that can be readily imported in ray tracers. The near-field goniophotometer could be used to perform such measurements, on condition that an external light source is added. A first attempt has been successfully realized.

Finally, the deconvolution technique, presented in chapter 5, was only applied to symmetrical BTDFs obtained under normal incident light. The same technique could also be used to deconvolve both asymmetrical BTDFs and BRDFs by expanding the bayesian deconvolution algorithm to two dimensions. In fact, as part of a European research project [EURAMET, 2013], the deconvolution approach will be applied to BSDFs of materials in order to study their visual appearance. Gloss perception of materials is not only determined by the specular reflectance value, but also by the haze and the distinctness-of-image (DOI). As these surface gloss attributes must be calculated from BRDF data for which a high angular resolution is needed [ASTM E430, 2011; ASTM D5767, 2004; Leloup, 2012], applying deconvolution methods might be very useful. Furthermore, during this project, round robin BRDF measurements of the same samples will be carried out at various national institutes, each having a different BSDF measurement setup. It is expected that the measured BRDFs will vary significantly depending on the instrument signature of each individual measurement device. The deconvolution approach will then be applied in order to minimize the effect of each instrument signature, and to obtain a higher correlation between the various measurements.

Appendix A

The following procedure discusses how to convert and import BSDF measurement data, obtained with the goniospectroradiometer developed at the Light&Lighting Laboratory for BSDF acquisition [Leloup et al., 2008], into the commercial ray tracing software package TracePro as a tabulated BSDF model. It describes the various coordinate systems encountered on the measurement equipment and in the ray tracer along with the conversion from the first towards the latter.

A BSDF measurement performed with the goniospectroradiometer at the Light&Lighting Laboratory [Leloup et al., 2008], results in two separate data files. One containing the incident radiant flux, $\Phi_{e,\lambda,i}$, and the other containing the scattered radiant fluxes, $\Phi_{e,\lambda,s}$, at various scatter angles (α,β) for the incident angles (γ,δ), both referenced in the global coordinate system (GCS) presented in figure A.1. These coordinates in the GCS determine respectively the position of both motors (rotation stage A and B) and the positioning of the sample (rotation stage C and D).

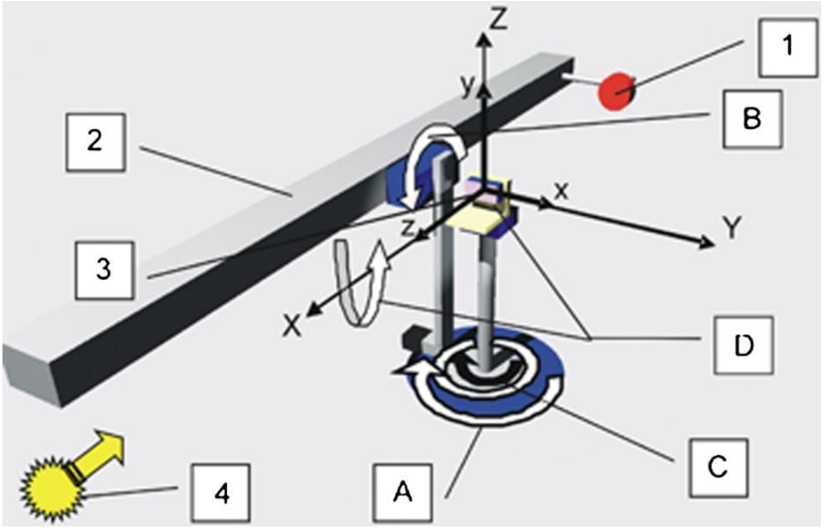

Figure A.1 – Representation of the initial (reference) position of the detector head (1), detector bench (2), and sample xyz coordinate system (SCS) (3) with respect to the global XYZ coordinate system (GCS). Also depicted are: the incident light direction (4) and the positive sense of rotation of the four rotation stages A, B, C, and D corresponding with the spherical coordinates relative to the GCS; α, β, γ and δ respectively.

In order to calculate the corresponding BSDF values, the detector coordinates expressed in the GCS, $(\alpha,\beta,\gamma,\delta)$, need to be converted to coordinates referenced to the sample coordinate system (SCS) denoted by $(\theta_{\mathrm{i}},\phi_{\mathrm{i}},\theta_{\mathrm{s}},\phi_{\mathrm{s}})$, with $(\theta_{\mathrm{i}},\phi_{\mathrm{i}})$ and $(\theta_{\mathrm{s}},\phi_{\mathrm{s}})$ the spherical coordinates indicating the direction of the radiation incident on the surface and the coordinates of the detector, respectively. In the SCS the local z-axis is aligned with the normal of the sample, the local x and y-axis are marked on the sample and form a right handed coordinate system. The GCS to SCS conversion is performed by equations A.1 and A.2 [Leloup et al., 2008] for the coordinates of the incident light and the detector positions respectively:

$$\boldsymbol{i} = \begin{pmatrix} \sin\gamma\cdot\cos\delta \\ -\sin\gamma\cdot\sin\delta \\ \cos\gamma \end{pmatrix} \tag{A.1}$$

$$\boldsymbol{d} = \begin{pmatrix} -\cos\alpha\cdot\cos\beta\cdot\sin\gamma\cdot\cos\delta+\sin\alpha\cdot\cos\beta\cdot\cos\gamma\cdot\cos\delta+\sin\beta\cdot\sin\delta \\ \cos\alpha\cdot\cos\beta\cdot\sin\gamma\cdot\sin\delta-\sin\alpha\cdot\cos\beta\cdot\cos\gamma\cdot\sin\delta+\sin\beta\cdot\cos\delta \\ -\cos\alpha\cdot\cos\beta\cdot\cos\gamma-\sin\alpha\cdot\cos\beta\cdot\sin\gamma \end{pmatrix} \tag{A.2}$$

With $\boldsymbol{i}$ and $\boldsymbol{d}$, representing the incident light direction and detector position, respectively as a vector expressed in cartesian coordinates with the components (i_x,i_y,i_z) and (d_x,d_y,d_z) respectively, relative to the SCS.

After the GCS to SCS conversion, $BSDF_{\mathrm{e}}$ values can be calculated as proposed by the American Society for Testing and Materials (ASTM) [ASTM E2387, 2005] using the practical formula:

$$BSDF_{\mathrm{e}} = \frac{\Phi_{\mathrm{e},\lambda,\mathrm{s}}}{\Phi_{\mathrm{e},\lambda,\mathrm{i}}\Omega_{\mathrm{s}}\left|\cos\theta_{\mathrm{s}}\right|}\left[\frac{1}{\mathrm{sr.nm}}\right] \tag{A.3}$$

with $\Phi_{\mathrm{e},\lambda,\mathrm{s}}$ and $\Phi_{\mathrm{e},\lambda,\mathrm{i}}$ the scattered radiant flux towards the detector and the incident radiant flux on the sample, respectively, Ω_{s} being the solid angle of the detector aperture.

In the commercial ray tracing software package, TracePro®, tabulated BSDF data is expressed in the “Harvey-Shack” coordinate system $(\theta_{\mathrm{i}},\phi_{\mathrm{i}},\beta_{\mathrm{sc}},\varphi_{sc})$ which finds it origin in the dissertation of Harvey and Shack [Harvey, 1976]. It was found that surface scattering, due to isotropic surface roughness of polished materials, is independent of the direction of incidence (shift-invariant) if expressed in direction cosines.
If a material exhibits isotropic surface scattering it can be modeled as a tabulated BSDF model which contains the $(\theta_{\mathrm{i}},\beta_{\mathrm{sc}},\varphi_{sc})$ coordinates with the corresponding

BSDF values. A simple test to determine whether the surface scattering is isotropic or anisotropic is to rotate the sample around its normal under a fixed angle of incidence θ_i. If the reflected and/or transmitted radiation pattern changes as the sample is rotated than the BSDF should be modeled as anisotropic, else it can be modeled as an isotropic tabulated BSDF model. The BSDF measurement apparatus designed by Harvey and Shack measured the BSDF directly at certain $(\beta_{sc}, \varphi_{sc})$ coordinates. However, the BSDF measurement device at the Light&Lighting laboratory measures the BSDF for various spherical coordinates by positioning the rotation stages A and B as shown in figure A.1. In order to import the measured BSDF into TracePro, a conversion from coordinates relative to the SCS towards the Harvey-Shack coordinate system is necessary.

Figure A.2 (a) and (b) displays the Harvey-Shack coordinate system used in TracePro to model isotropic surface scattering for a scatter direction **d** and a perpendicularly incident light direction **i**.

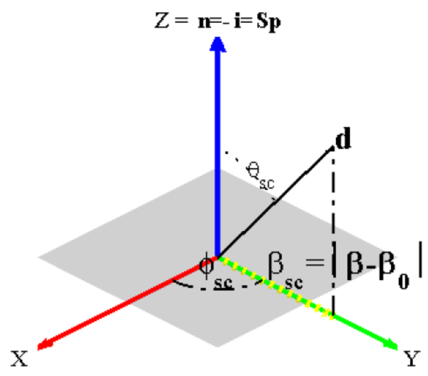

(a)

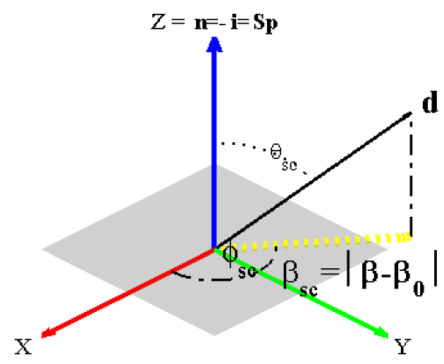

(b)

Figure A.2 – Representation of the Harvey-Shack $(\beta_{sc}, \varphi_{sc})$ coordinate system for isotropic surface scattering, with light perpendicularly incident on the sample surface. (a) and (b) show 2 different scatter directions **d** with their respective β_{sc} and φ_{sc} coordinates.

In the illustration above, the incident direction **i** is opposite to the normal of the sample (**n**), which is aligned with the SCS's Z-axis; as a consequence the specular direction **Sp** equals the Z-axis. All of the vectors **i**, **Sp** and **d** are unit vectors.
In this specific case, one could look at the Harvey-Shack coordinates $(\beta_{sc}, \varphi_{sc})$ as polar coordinates with the projection of the specular direction ($\boldsymbol{\beta_0}$) as origin, β_{sc} the length of the vector, $\boldsymbol{\beta_{sc}}$, formed by subtracting the projection of the scatter direction **d** onto the XY plane denoted by $\boldsymbol{\beta}$ with the vector $\boldsymbol{\beta_0}$, and φ_{sc} being the angle between the X-axis and $\boldsymbol{\beta}$.

For this particular case the β_{sc} and φ_{sc} values can be calculated as expressed in equation A.4 and A.5 respectively:

$$\beta_{\mathrm{sc}} = \sqrt{d_x^{\,2} + d_y^{\,2}} \tag{A.4}$$

$$\begin{aligned} \varphi_{sc} &= \cos^{-1}\left(\frac{\boldsymbol{X}\cdot\boldsymbol{\beta_{sc}}}{|\boldsymbol{X}||\boldsymbol{\beta_{sc}}|}\right) \\ &= \cos^{-1}\left(\frac{d_x}{\sqrt{d_x^{\,2}+d_y^{\,2}}}\right) \end{aligned} \tag{A.5}$$

With (d_X, $d_{Y,}$ d_Z), the cartesian components of of the scatter direction **d**. To ensure that φ_{sc} lies within the range [0°..360°[, equation A.5 is adjusted to take into account the sign of the y-component of $\boldsymbol{\beta_{sc}}$:

$$\varphi_{sc,0..360} = \begin{cases} \varphi_{sc} & \beta_{sc,y} \geq 0 \\ \varphi_{sc} + \pi & \beta_{sc,y} < 0 \end{cases} \tag{A.6}$$

A more general formulation of the Harvey-Shack coordinates $(\beta_{\mathrm{sc}}, \varphi_{sc})$, for a non-perpendicular incident light direction **i** and a scatter direction **d**, expressed with their respective cartesian components (i_x,i_y,i_z) and (d_x,d_y,d_z) in the SCS is derived below. A graphical representation of the Harvey-Shack coordinate system for non-perpendicular incident light is shown in figure A.3.

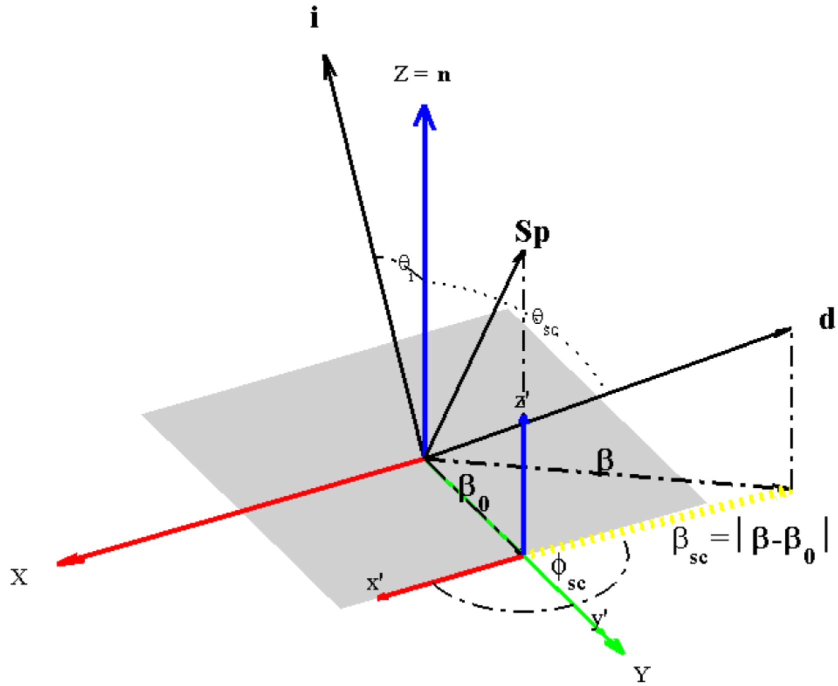

Figure A.3 – Representation of the Harvey-Shack $(\beta_{sc}, \varphi_{sc})$ coordinate system for isotropic surface scattering, with non- perpendicular incident light on the sample surface. The incident direction **i** is located in the ZY plane.

The general equation for β_{sc} for a non-perpendicular incident light direction **i** and scatter direction **d** can be derived as follows:

1) As the normal of the sample equals the Z-axis, the specular direction, Sp, can be calculated as displayed in equation A.7:

$$\mathbf{Sp} = \begin{bmatrix} -i_x & -i_y & i_z \end{bmatrix} \cdot \begin{bmatrix} e_X \\ e_Y \\ e_Z \end{bmatrix} \tag{A.7}$$

2) The projection of Sp and d onto the XY plane, denoted by $\boldsymbol{\beta}_0$ and $\boldsymbol{\beta}$ respectively, can be written as:

$$\boldsymbol{\beta_0} = \begin{bmatrix} -i_x & -i_y & i_z \end{bmatrix} \cdot \begin{bmatrix} e_X \\ e_Y \\ 0 \end{bmatrix}$$
$$\boldsymbol{\beta} = \begin{bmatrix} d_x & d_y & d_z \end{bmatrix} \cdot \begin{bmatrix} e_X \\ e_Y \\ 0 \end{bmatrix} \tag{A.8}$$

3) As β_{sc} equals the length of the vector formed by subtracting $\boldsymbol{\beta}$ from $\boldsymbol{\beta}_0$, it can be calculated as follows:

$$\begin{aligned}\boldsymbol{\beta_{sc}} &= \boldsymbol{\beta} - \boldsymbol{\beta_0} \\ &= \begin{bmatrix} d_x + i_x & d_y + i_y & d_z - i_z \end{bmatrix} \cdot \begin{bmatrix} e_X \\ e_Y \\ e_Z \end{bmatrix}\end{aligned} \tag{A.9}$$

$$\begin{aligned}\beta_{sc} &= \left|\boldsymbol{\beta_{sc}}\right| \\ &= \sqrt{\left(d_x + i_x\right)^2 + \left(d_y + i_y\right)^2}\end{aligned} \tag{A.10}$$

As both $\boldsymbol{\beta}$ and $\boldsymbol{\beta_0}$ are projections of unit vectors, β_{sc} will have a range of [0..2].

Generally speaking, the second coordinate, φ_{sc} is the angle between the vector $\boldsymbol{\beta}$ and a vector which is perpendicular to a plane formed by the incident direction and the normal of the sample. For incident light in the YZ plane as illustrated in figure A.3, this vector equals the SCS’s X-axis and equation A.6 could be used.
However, for an incident direction that does not lie in the YZ plane, a local coordinate sytem $\mathbf{x'y'z'}$ needs to be defined as shown in figure A.4.

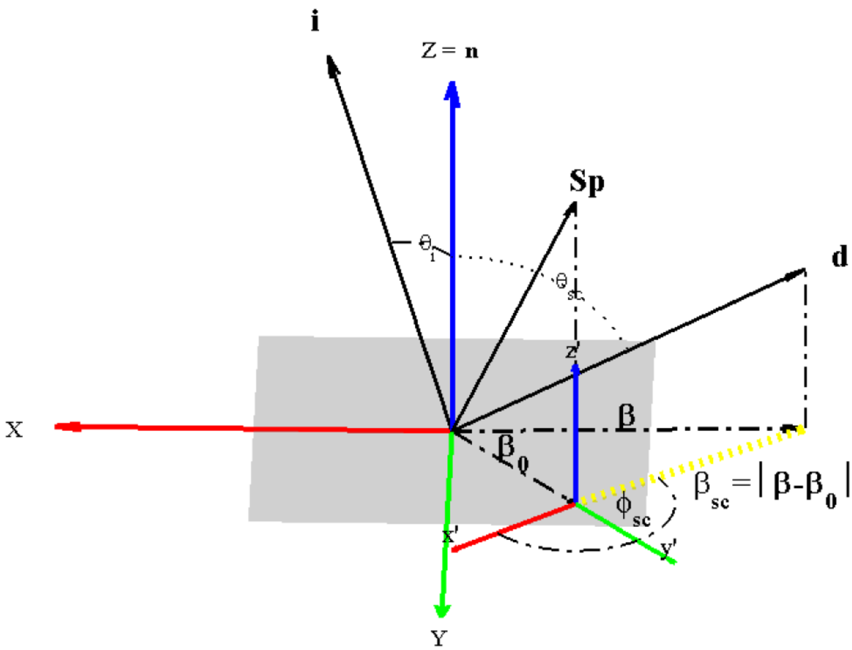

Figure A.4 – Representation of the Harvey-Shack $(\beta_{sc},\varphi_{sc})$ coordinate system for isotropic surface scattering, with non-perpendicular incident light on the sample surface. The incident direction **i** is not located in the YZ plane, therefore a local coordinate system $\mathbf{x'y'z'}$ is defined.

The angle φ_{sc} is now calculated as the angle between the local $\mathbf{x'}$ axis and the vector $\boldsymbol{\beta}_{sc}$. The calculations of φ_{sc} for a given incident direction **i** and a scatter direction **d** are as follows:

1) Create a local coordinate system, $\mathbf{x'y'z'}$, expressed in the global coordinate system XYZ as follows:

$$\begin{cases} \mathbf{z'} = \boldsymbol{Z} = \boldsymbol{n} \\ \mathbf{x'} = \mathbf{z'} \times \mathbf{i} \\ \mathbf{y'} = \mathbf{z'} \times \mathbf{x'} \end{cases} \tag{A.11}$$

which can be rewritten as:

$$\begin{cases} \mathbf{z'} = \begin{bmatrix} 0 & 0 & 1 \end{bmatrix} \cdot \begin{bmatrix} \mathbf{e_X} \\ \mathbf{e_Y} \\ \mathbf{e_Z} \end{bmatrix} \\ \mathbf{x'} = \begin{bmatrix} -i_y & i_x & 0 \end{bmatrix} \cdot \begin{bmatrix} \mathbf{e_X} \\ \mathbf{e_Y} \\ \mathbf{e_Z} \end{bmatrix} \\ \mathbf{y'} = \begin{bmatrix} -i_x & -i_y & 0 \end{bmatrix} \cdot \begin{bmatrix} \mathbf{e_X} \\ \mathbf{e_Y} \\ \mathbf{e_Z} \end{bmatrix} \end{cases} \tag{A.12}$$

After normalization to unit vectors this becomes:

$$\begin{cases} \mathbf{z'} = \begin{bmatrix} 0 & 0 & 1 \end{bmatrix} \cdot \begin{bmatrix} \mathbf{e_X} \\ \mathbf{e_Y} \\ \mathbf{e_Z} \end{bmatrix} \\ \mathbf{x'} = \begin{bmatrix} \dfrac{-i_y}{\sqrt{(i_x)^2 + (i_y)^2}} & \dfrac{i_x}{\sqrt{(i_x)^2 + (i_y)^2}} & 0 \end{bmatrix} \cdot \begin{bmatrix} \mathbf{e_X} \\ \mathbf{e_Y} \\ \mathbf{e_Z} \end{bmatrix} \\ \mathbf{y'} = \begin{bmatrix} \dfrac{-i_x}{\sqrt{(i_x)^2 + (i_y)^2}} & \dfrac{-i_y}{\sqrt{(i_x)^2 + (i_y)^2}} & 0 \end{bmatrix} \cdot \begin{bmatrix} \mathbf{e_X} \\ \mathbf{e_Y} \\ \mathbf{e_Z} \end{bmatrix} \end{cases} \tag{A.13}$$

2) $\boldsymbol{\beta}_{sc}$ can be expressed in the local coordinate system as follows:

$$\boldsymbol{\beta}_{sc'} \begin{cases} \beta_{sc,x'} = \left|\boldsymbol{\beta}_{sc}\right| \cdot \cos\left(\theta_{x'}\right) \\ \beta_{sc,y'} = \left|\boldsymbol{\beta}_{sc}\right| \cdot \cos\left(\theta_{y'}\right) \\ \beta_{sc,z'} = \left|\boldsymbol{\beta}_{sc}\right| \cdot \cos\left(\theta_{z'}\right) \end{cases} \tag{A.14}$$

with $\theta_{x'}$, $\theta_{y'}$ and $\theta_{z'}$ the angle between $\boldsymbol{\beta}_{sc}$ and $\mathbf{x'}$, $\mathbf{y'}$ and $\mathbf{z'}$, respectively. This expression can be rewritten as:

$$\boldsymbol{\beta_{sc'}} \begin{cases} \beta_{sc,x'} = \boldsymbol{\beta_{sc}} \cdot \mathbf{x'} = \dfrac{-i_y\left(d_x + i_x\right) + i_x\left(d_y + i_y\right)}{\sqrt{\left(i_x\right)^2 + \left(i_y\right)^2}} \\ \beta_{sc,y'} = \boldsymbol{\beta_{sc}} \cdot \mathbf{y'} = \dfrac{-i_x\left(d_x + i_x\right) - i_y\left(d_y + i_y\right)}{\sqrt{\left(i_x\right)^2 + \left(i_y\right)^2}} \\ \beta_{sc,z'} = \boldsymbol{\beta_{sc}} \cdot \mathbf{z'} = 0 \end{cases} \tag{A.15}$$

3) The φ_{sc} coordinate equals the angle between $\mathbf{x'}$ in local coordinates and $\boldsymbol{\beta_{sc'}}$, therefore φ_{sc} is calculated as:

$$\varphi_{sc} = \cos^{-1}\left(\frac{-i_y\left(d_x + i_x\right) + i_x\left(d_y + i_y\right)}{\sqrt{\left(d_x + i_x\right)^2 + \left(d_y + i_y\right)^2}\sqrt{\left(i_x\right)^2 + \left(i_y\right)^2}}\right) \tag{A.16}$$

4) To ensure that φ_{sc} has a range of [0°..360°[, the same adjustment as in equation A.6 is performed, this time however by taking into account the sign of the local y component of $\boldsymbol{\beta_{sc'}}$:

$$\varphi_{sc,0..360} = \begin{cases} \varphi_{sc} & \beta_{sc,y'} \geq 0 \\ \varphi_{sc} + \pi & \beta_{sc,y'} < 0 \end{cases} \tag{A.17}$$

In conclusion: for isotropic surface scattering under perpendicular incident light, the equations A.4 and A.6 must be used, for any other direction of incident light, equations A.10 and A.17 are necessary to calculate β_{sc} and $\varphi_{sc,0..360}$ respectively.

Appendix B

While Appendix A describes the coordinate systems and the various transformations, this section discusses a practical example of a BSDF measurement and the conversion to the Harvey-Shack coordinate system and tabulated values as defined in TracePro for an isotropic asymmetric surface scattering of a material that exhibits some symmetry around the specular direction. Such a material is the MicroCellular PolyEthylene Terephthalate (MCPET) [American Furukawa Inc., 2008].

First, scattered flux measurements of the MPET material are measured for an incident angle of 5° and 60°. As some form of symmetry is assumed around the specular direction, two scans are performed for each incident angle; one in the plane of incidence (Π_1) and one in a plane (Π_2) perpendicular to the plane of incidence and through the specular direction as shown in figure B.1.

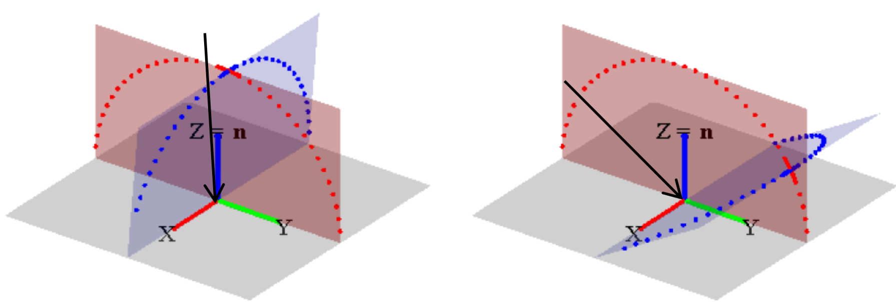

(a) (b)

Figure B.1 – Graphical representation of two scans performed with the BSDF measurement device by moving around rotation stage A and B. The angle of incidence (black arrow) equals 5° and 60° for (a) and (b) respectively. Red dots denote the measurement points at various detector positions in the plane of incidence Π_1, while blue dots represent those in a plane Π_2 which is perpendicular to the incident plane and through the specular direction.

Note the higher sampling density around the specular region and the absence of measurement points towards the light source direction as this would cause the detector bench onto which the detector is mounted to block the illuminating beam to be incident on the sample. Also note that in both Π_2 planes the measurement points do not go as far towards the sample surface as in plane Π_1 , this is caused by the inability to move the detector bench towards these directions due to construction of the sample holder base.

Next, absolute BRDF values are calculated from the measurements performed at each of the scatter directions according to equation A.3. The scatter directions are then converted to their respective Harvey-Shack coordinates $(\beta_{sc}, \varphi_{sc})$ according to equation A.10 and A.17. These coordinates are plotted in a cartesian coordinate system U, V with $U = \beta_{sc}\cos(\varphi_{sc})$ and $V = \beta_{sc}\sin(\varphi_{sc})$ as shown in figure B.1 (a) and (b) for the incident angles 5° and 60° respectively.

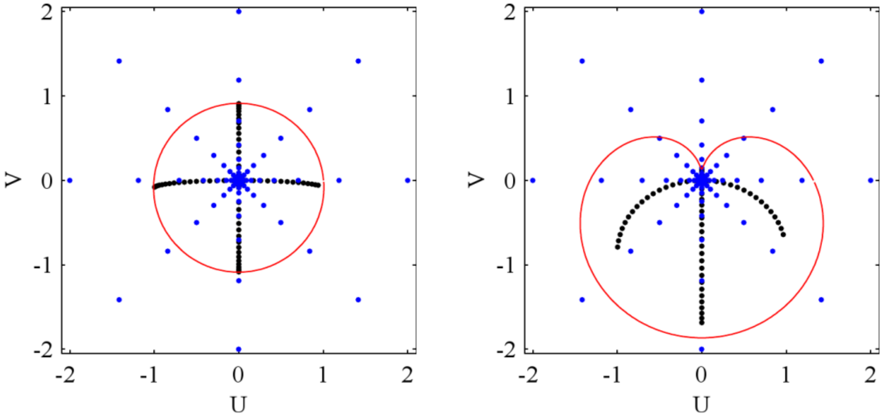

(a) (b)

Figure B.2 – Graphical representation of the (β_{sc}, φ_{sc}) coordinates expressed in a cartesian coordinate system (U, V) corresponding to the measured scatter directions (black dots), the scatter directions as needed in the gridded tabular Harvey-Shack model (blue dots) and the maximum range for which scatter directions in reflection are valid (area within the red line) for the incident angles of 5° and 60°, shown respectively in (a) and (b). The gridded (β_{sc}, φ_{sc}) coordinates (blue dots) are formed with 20 logarithmically spaced β_{sc} values in the range [0..2], and 8 linearly spaced φ_{sc} values in the range [0..360[.

In figure B.2 (a) and (b) the red line represents the maximum β_{sc} value for each φ_{sc} value for which a BRDF value is possible. Points outside the area enclosed by the red line have an undefined BRDF value as these points correspond to directions located at the other side of the sample (i.e. transmission directions). The β_{sc} value for a given φ_{sc} value and angle of incidence θ_i is calculated as followed:

$$\beta_{sc}^{\ 2} = |\boldsymbol{\beta}|^2 + |\boldsymbol{\beta_0}|^2 - 2|\boldsymbol{\beta}||\boldsymbol{\beta_0}|\cos(\frac{\pi}{2} - \varphi_{sc}) \quad \text{(B.1)}$$

As $|\boldsymbol{\beta}|$ equals to 1 for all scatter directions which are parallel to the sample surface, the maximum physically possible β_{sc} value, $\beta_{sc,max}$, is illustrated in figure B.3 and can be calculated as:

$$\beta_{sc,max} = \sqrt{1 + \sin(\theta_i)^2 - 2\sin(\theta_i)\cos(\frac{\pi}{2} - \varphi_{sc})} \qquad (B.2)$$

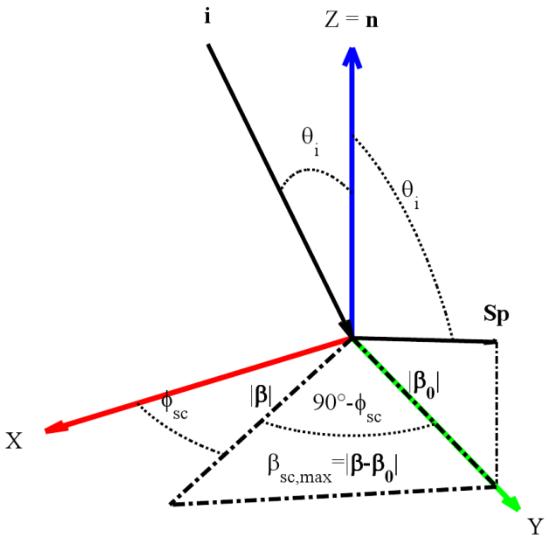

Figure B.3 – Illustration of the $\beta_{sc,max}$ value for a given direction of incidence **i** and corresponding specular direction **Sp** and a scatter direction **β**. A triangle is formed by **β**, $\boldsymbol{\beta_0}$ and $\boldsymbol{\beta}$-$\boldsymbol{\beta_0}$ with the respective lengths of the sides being |**β**|, |$\boldsymbol{\beta_0}$| and $\beta_{sc,max}$.

In the ray tracer, a gridded set of $(\beta_{sc}, \varphi_{sc})$ coordinates (i.e. each β_{sc} coordinate is combined with each φ_{sc} coordinate, thus forming a grid – see the blue dots in figure B.2) with corresponding BRDF values must be entered for each angle of incidence. Additionally, this grid of coordinates must be the same for each angle of incidence. The number of β_{sc} and φ_{sc} coordinates can be chosen freely. When tracing rays, the ray tracer will perform a linear interpolation between the gridded $(\beta_{sc}, \varphi_{sc})$ coordinates. As can be seen from figure B.2 (a) and (b), the measured data points are however scattered in the $(\beta_{sc}, \varphi_{sc})$ domain, as a consequence the measured BRDF values can not be entered directly into the tabular Harvey-Shack model. Furthermore, the coordinates $(\beta_{sc}, \varphi_{sc})$ at the measurement points differ for each incident angle, this is expected as both the expression for β_{sc} and φ_{sc} as given by equation A.10 and A.17 contain the incident direction. This means that two distinct $(\beta_{sc}, \varphi_{sc})$ coordinates are found if one would calculate the $(\beta_{sc}, \varphi_{sc})$ coordinates of a direction which has an offset of 1° from the specular direction for two different incident angles.

In order to create a gridded set of $(\beta_{sc}, \varphi_{sc})$ coordinates based on the measurement performed in both the Π_1 and Π_2 plane a linear interpolation between the corresponding UV coordinates (figure B.2) of the measurement points and their corresponding BRDF values is performed. In this specific case, the interpolation is performed for 100 logarithmically spaced β_{sc} values in the range [0..2] and 36 linearly spaced φ_{sc} values in the range [0..360[. Afterwards the interpolated data points are imported in the ray tracer, which automatically calculates the Total Integrated Scatter (TIS). In order to maintain conservation of energy the absorptance coefficient is set to equal 1-TIS. Next, the implemented tabular Harvey-Shack model is applied to a surface of a material which is oriented parallel to the XY plane and a parallel beam of rays were traced towards this surface with an incident angle of 5° and 60°. Finally, illuminance values on a hemispherical surface (radius = 1m) placed over the sample surface are calculated and projected onto the XY plane as shown in figure B.4 (a) and (b) for the 5° and 60° incident beam.

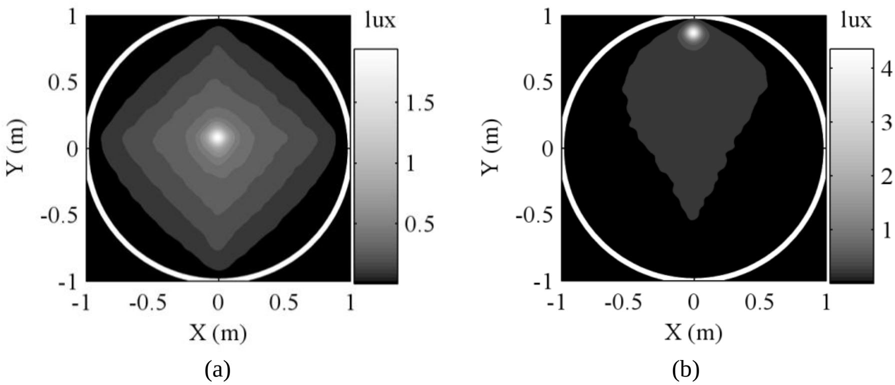

Figure B.4 – Illumination on a hemispherical surface positioned above the surface to which the tabular Harvey-Shack model is applied. (a) and (b) show the projected illuminance values onto a plane for an angle of incidence of 5° and 60° respectively. The white outer circle represents the base of the hemispherical surface with a radius of 1m.

As can be seen in figure B.4 the circular symmetry around the specular direction is present but only in a limited angular area around the specular direction. Beyond this area, a diamond shaped pattern becomes visible. Additionally, the TIS as calculated by the ray tracer equaled 67% and 75% for the incident angle of 5° and 60° respectively. However, total reflectance measurements performed in a d/8° integrating sphere geometry showed that the TIS value under an angle of incidence of 8° should be 98.4%.

To address these issues, a more sophisticated interpolation scheme is proposed, taking into account that a quasi-circular symmetry is present around the specular direction. The following steps are performed to obtain a correct tabular Harvey-Shack model which can be entered directly into the ray tracer:

1) Rotate the calculated BRDF values for each angle of incidence θ_i, expressed in the spherical coordinates $(\theta_d, \varphi_d, BRDF)$ relative to the normal with θ_d, φ_d the detector position, in such a way that the specular direction coincides with the Z-axis, i.e. a rotation of each measurement point of $-\theta_i$ degrees around the X-axis. Each point is now expressed in the spherical coordinates, $(\theta_d', \varphi_d', BRDF')$, relative to the specular direction.This rotation is obtained by the following matrix operation which was derived in Leloup et al., 2008:

$$\begin{pmatrix} d_x' \\ d_y' \\ d_z' \end{pmatrix} = \mathbf{R}(\mathbf{A}, \theta). \begin{pmatrix} d_x \\ d_y \\ d_z \end{pmatrix} \quad \text{B.3}$$

with (d_x', d_y', d_z') and (d_x, d_y, d_z) respectively the cartesian representation of the spherical coordinates $(\theta_d', \varphi_d', BRDF')$ and $(\theta_d, \varphi_d, BRDF)$, and **R**(**A**,θ) the rotation matrix around **A** over an angle θ explicitly given by:

$$\mathbf{R}(\mathbf{A},\theta) = \frac{1}{|\mathbf{A}|} \begin{pmatrix} A_x^2 + \cos\theta\left(A_y^2 + A_z^2\right) & A_x A_y(1-\cos\theta) - A_z|\mathbf{A}|^{1/2}\sin\theta & A_x A_z(1-\cos\theta) + A_y|\mathbf{A}|^{1/2}\sin\theta \\ A_x A_y(1-\cos\theta) + A_z|\mathbf{A}|^{1/2}\sin\theta & A_y^2 + \cos\theta\left(A_x^2 + A_z^2\right) & A_y A_z(1-\cos\theta) + A_x|\mathbf{A}|^{1/2}\sin\theta \\ A_x A_z(1-\cos\theta) + A_y|\mathbf{A}|^{1/2}\sin\theta & A_y A_z(1-\cos\theta) + A_x|\mathbf{A}|^{1/2}\sin\theta & A_z^2 + \cos\theta\left(A_x^2 + A_y^2\right) \end{pmatrix} \quad \text{B.4}$$

with **A** the X-axis and $\theta = -\theta_i$.

2) With the measurement points expressed relative to the specular direction, all data points now lie in the direction $\varphi_d' =$ [0°, 90°, 180°, 270°]. Additional points, $(\theta_d', \varphi_d') =$ $(90°, 0°)$, $(90° - \theta_i, 90°)$, $(90°, 180°)$, $(90° + \theta_i, 270°)$, are added to the measured data points to explicitly set the limits of the measurement range, at these coordinates the BRDF value is set to 0.

3) A linear interpolation for both θ_d', φ_d' is performed with a $\Delta\theta_d'$ of 0.1° and a $\Delta\varphi_d'$ of 1° resulting in a dense dataset for which a symmetry around the specular direction is obtained. This is shown in figure B.5 for the incident angle of 5°.

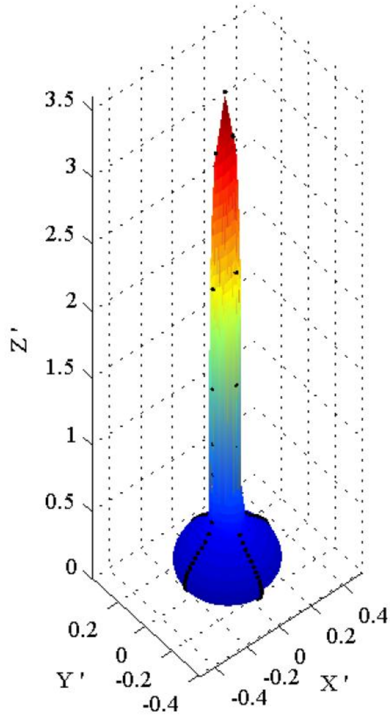

Figure B.5 – Linearly interpolated BRDF (colored surface) with symmetry around the specular direction (Z') for an incident angle of 5°, displayed in a $X'Y'Z'$ coordinate system with $X' = \sin(\theta_d')\cos(\varphi_d')BRDF'$, $Y' = \cos(\theta_d')\cos(\varphi_d')BRDF'$ and $Z' = \cos(\theta_d')BRDF'$. Black dots denote the original measurement points.

4) Rotate the interpolated data points using equation B.4 with **A** the X-axis and $\theta = \theta_i$. All data points are now again expressed relative to the normal of the sample.

5) Convert the interpolated data points to the Harvey-Shack coordinate system using equation A.10 and A.17.

6) Interpolate over a defined number of β_{sc}, φ_{sc} , values to obtain a gridded data set that can be imported in the ray tracer. In this specific case the interpolation is performed for 100 logarithmically spaced β_{sc} values in the range [0..2] and 36 linearly spaced φ_{sc} values in the range [0..360[. Care should be taken to define a BRDF value of 0 at each $\beta_{sc,max}$ value for each φ_{sc} that is interpolated.

Figure B.6 (a) and (b) show a graphical presentation of the measured data points, interpolated data points using the symmetry around the specular direction and interpolated data points in the Harvey-Shack coordinate system to be entered in the ray tracer expressed in a cartesian coordinate system U, V with $U = \beta_{sc}\cos(\varphi_{sc})$ and $V = \beta_{sc}\sin(\varphi_{sc})$ for the incident angles 5° and 60° respectively.

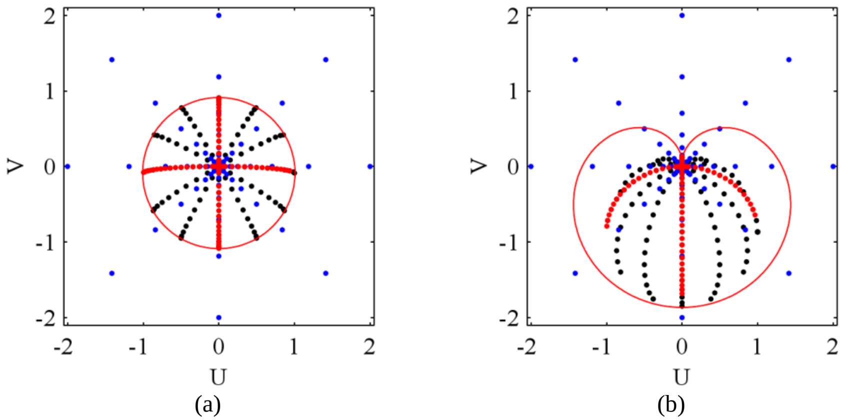

Figure B.6 –Graphical representation of the (β_{sc}, φ_{sc}) coordinates expressed in a cartesian coordinate system (U, V) corresponding to the measured scatter directions (red dots), the scatter directions as needed in the tabular Harvey-Shack model (blue dots), the interpolated scatter directions obtained from the symmetry around the specular direction (black dots) and the maximum range for which scatter directions in reflection are valid (area within the red line) for the incident angles of 5° and 60°, shown respectively in (a) and (b). The gridded (β_{sc}, φ_{sc}) coordinates (blue dots) are formed with 20 logarithmically spaced β_{sc} values in the range [0..2], and 8 linearly spaced φ_{sc} values in the range [0..360[. The interpolated scatter directions obtained from the symmetry around the specular direction are formed with a $\Delta\theta_d'$ of 10° and a $\Delta\varphi_d'$ of 30°.

When importing the data points in the ray tracer, obtained through the procedure described above, the calculated TIS equals 99.5% and 91.4% for the angle of incidence of 5° and 60° respectively. To verify the scattering behavior of a surface for which the imported BRDF data is applied, parallel beams are traced in the same way as before (under 5° and 60° incidence). The illumination on a hemispherical surface placed above the sample is again calculated and displayed in figure B.7. As can be seen the shape is now indeed more symmetric around the specular direction.

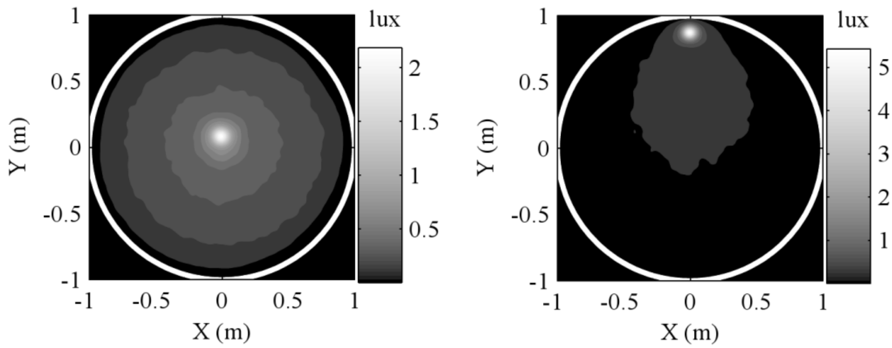

Figure B.7 – Illumination on a hemispherical surface positioned above the surface to which the tabular Harvey-Shack model is applied when interpolating the measured data when rotated to the specular direction. (a) and (b) show the projected illuminance values onto a plane for an angle of incidence of 5° and 60° respectively. The white outer circle is the base of the hemispherical surface with a radius of 1m.

In conclusion; for isotropic surface scattering that exhibits some symmetry around the specular direction only a limited number of scattered flux measurements need to be obtained in order to accurately characterize the BRDF for a given angle of incidence. After interpolating the measured data, it is advised to perform some basic ray tracing checks to see whether both the shape of the scattered radiation pattern and the TIS is consistent with the true scattered radiation pattern and TIS measured in an integrating sphere geometry.

If no symmetry around the specular direction is present more data points need to be obtained and the first interpolation scheme (linear interpolation in the UV coordinate system – see figure B.2 and B.4) should be used. Additional techniques such as Radial Basis Functions (RBF) which have proven to be very successful for 3D surface reconstruction in computer graphics [Carr et al., 2001; Dinh et al., 2002] and medical imaging [Carr et al., 1997] or Shepards method [Renka, 1988] could then be employed to create a gridded set of data points which can be imported in the ray tracer.

Also note that this interpolation issue will emerge for any ray tracer that does not accept data which was measured at various points scattered in the coordinate system being used, whether it is a Harvey-Shack, cartesian or spherical coordinate system.

Bibliography

[3M, 2013] 3M, "Vikuiti™ Brightness Enhancement Film," http://www.3m.com/, accessed September 2013.

[American Furukawa Inc., 2008] American Furukawa Inc., "MCPET datasheet," 2008, http://www.furukawaamerica.com/mcpet.html, accessed February 2013.

[Aretz and Vorländer, 2014] M. Aretz and M. Vorländer, "Combined wave and ray based room acoustic simulations of audio systems in car passenger compartments, Part I: Boundary and source data," Applied Acoustics, vol. 76, pp 82–99, 2014.

[Aretz and Vorländer, 2014] M. Aretz and M. Vorländer, "Combined wave and ray based room acoustic simulations of audio systems in car passenger compartments, Part II: Comparison of simulations and measurements," Applied Acoustics, vol. 76, pp. 52–65, 2014.

[ASAP, 2013] Breault Research Organization, http://www.breault.com/, accessed September 2013.

[Ashdown and Rykowski, 1998] I. Ashdown, R. Rykowski, "Making Near-Field Photometry Practical," Journal of the Illuminating Engineering Society, vol. 27, pp. 67-79, 1998.

[Ashdown and Salsbury, 2006] I. Ashdown and M. Salsbury, "A Near-Field Goniospectroradiometer for LED Measurements," International Optical Design, Technical Digest - Optical Society of America, paper TuD5, 2006.

[Ashdown, 1993] I. Ashdown, "Near-field photometry in practice," IESNA Annual Conference Technical Papers, pp. 413-425, 1993.

[ASTM D5767, 2004] American Society for Testing and Materials Standard D5767, "Standard Test Methods for Instrumental Measurement of Distinctness-of-Image Gloss of Coating Surfaces," (ASTM, 2004).

[ASTM E2387, 2005] American Society for Testing and Materials Standard E2387, "Standard Practice for Goniometric Optical Scatter Measurements," (ASTM, 2005).

[ASTM E430, 2011] American Society for Testing and Materials Standard E430, “Standard Test Methods for Measurement of Gloss of High-Gloss Surfaces by Abridged Goniophotometry,” (ASTM, 2011).

[Audenaert et al., 2011] J. Audenaert, G. Durinck, G. Deconinck, P. Hanselaer, “A case study on the importance of adequate input during the virtual prototyping stage of a luminaire,” Romanian Lighting Convention, pp. 84-89, 2011.

[Bertero et al., 2009] M. Bertero, P. Boccacci, G. Desidera and G. Vicidomini, “Image deblurring with Poisson data: from cells to galaxies,” Inverse Problems, vol. 25, no. 12, 2009.

[Bishop, 2007]. C. M. Bishop, *Pattern Recognition and machine learning*, Springer, New York, 2nd edition, 2007.

[Bowsher et al., 1996] J. E. Bowsher, V. E. Johnson, T. G. Turkington, R. J. Jaszczak, C. E. Jr. Floyd and R. E. Coleman, “Bayesian reconstruction and use of anatomical a priori information for emission tomography,” IEEE Transactions on Medical Imaging, vol. 15, pp. 673-686, 1996.

[Bredemeier et al., 2007] K. Bredemeier, R. Poschmann, and F. Schmidt, “Development of luminous objects with measured ray data,” Laser+Photonik, vol. 2, pp. 20–24, 2007.

[Burke and Kendall, 2005] E. K. Burke and G. Kendall, *Search methodologies: introductory tutorials in optimization and decision support techniques*, Springer, 2005.

[Butler and Stephens, 2007] L.A. Butler, A. Stephens, “Bullet Ray Vision,” IEEE Symposium on Interactive Ray Tracing, pp. 167-170, 2007.

[Carr et al., 1997] J.C. Carr, W. R. Fright and R.K. Beatson, “Surface interpolation with radial basis functions for medical imaging,” IEEE Transactions on Medical Imaging, vol. 16, no. 1, pp. 96-107, 1997.

[Carr et al., 2001] J. C. Carr, R. K. Beatson, J. B. Cherrie, T. J. Mitchell, W. R. Fright, B. C. McCallum and T. R Evans, “Reconstruction and representation of 3D objects with radial basis functions,” Proceedings of the 28th annual conference on Computer graphics and interactive techniques, pp. 67-76, 2001.

[Chien et al., 2007] W. Chien, C. Sun and I. Moreno, "Precise optical model of multi-chip white LEDs," Opt. Express, vol. 15, pp. 7572-7577, 2007.

[CIE 117, 1995] Commission Internationale de L'éclairage Technical Report 117:1995, "Discomfort glare in interior lighting," (CIE, 1995).

[CIE 121, 1996] Commission Internationale de L'éclairage Technical Report 121:1996, "The photometry and goniophotometry of luminaires," (CIE, 1996).

[CIE 167, 2005] Commission Internationale de L'éclairage Technical Report 167:2005, "Recommended practice for tabulating spectral data for use in colour computations," (CIE, 2005).

[CIE 205, 2013] Commission Internationale de L'éclairage Technical Report 205:2013, "Review of Lighting Quality Measures for Interior Lighting with LED Lighting Systems," (CIE, 2013).

[CIE 95, 1992] Commission Internationale de L'éclairage Technical Report 95:1992, "Contrast and visibility," (CIE, 1992).

[CIE TC-2-62, 2010] CIE TC-2-62, "Imaging-photometer-based near-field goniophotometer," CIE Draft No1, 2010.

[Combes et al., 2007] D. Combes, L. Bousquet, S. Jacquemoud, H. Sinoquet, C. Varlet-Grancher and I. Moya, "A new spectrogoniophotometer to measure leaf spectral and directional optical properties," Remote Sensing of Environment, vol. 109, pp. 107-117, 2007.

[Dinh et al., 2002] H. Q. Dinh, G. Turk and G. Slabaugh, "Reconstructing surfaces by volumetric regularization using radial basis functions," IEEE Transactions on Pattern Analysis and Machine Intelligence, vol. 24, no. 10, pp. 1358-1371, 2002.

[Dutré et al., 2006] P. Dutré P, K. Bala and P. Bekaert, "Advanced Global Illumination," A.K. Peters Ltd., Wellesley, Massachusetts, 2nd edition, 2006

[Eble-Hankins, 2008] M. Eble-Hankins, "Subjective impression of discomfort glare from sources of non-uniform luminance," Ph. D. Dissertation, University of Nebraska, 2008.

[Eichstädt et al., 2013] S. Eichstädt, F. Schmähling, G. Wübbeler, K. Anhalt, L. Bünger, U. Krüger and C. Elster, “Comparison of the Richardson–Lucy method and a classical approach for spectrometer bandpass correction,” Metrologia, vol. 50, no. 107, doi:10.1088/0026-1394/50/2/107, 2013

[EURAMET, 2013] EURAMET, “Publishable JRP summary report for JRP IND52 xDReflect multidimensional reflectometry for industry,” http://www.euramet.org/fileadmin/docs/EMRP/JRP/JRP_Summaries_2012/Industry_JRPs/IND52_Publishable_JRP_Summary.pdf, accessed November 2013.

[Fergus et al., 2006] R. Fergus, B. Singh, A. Hertzmann, S. T. Roweis and W. T. Freeman, “Removing Camera Shake From A Single Photograph,” ACM Trans. Graph., vol. 26, no. 3, pp. 787-794, 2006.

[Ferrero et al., 2011] A. Ferrero A, J. Campos, A. M. Rabal, A. Pons, M. L. Hernanz and A. Corrons, “Deconvolution of non-zero solid angles effect in Bidirectional Scattering Distribution Function measurements,” Proc. SPIE 8083, Modeling Aspects in Optical Metrology III, 808315, 2011.

[Gardner, 2013] J. L. Gardner, “Spectral deconvolution applications for colorimetry,” Color Res. Appl., doi: 10.1002/col.21822, 2013.

[Geelen et al., 2013] B. Geelen, N. Tack, A. Lambrechts, “A snapshot multispectral imager with integrated tiled filters and optical duplication,” Proc. SPIE 8613, Advanced Fabrication Technologies for Micro/Nano Optics and Photonics VI, 861314, 2013.

[Gesù and Starovoitov, 1999] V. Di Gesù and V. Starovoitov, “Distance-based functions for image comparison,” Pattern Recognition Letters, vol. 20, no. 2, pp. 207-214, 1999.

[Gonzalez and Woods, 2002] R. C. Gonzalez, R. E. Woods, *Digital Image Processing*, Prentice Hall, 2002.

[Gringerton and Yepez, 1992] I. I. Gringorten and P. J. Yepez, “The division of a circle or spherical surface into equal-area cells or pixels,” Hanscom Air Force Base, Mass. : Phillips Laboratory, Directorate of Geophysics, 1992.

[Harvey, 1976] J. E. Harvey “Light-Scattering Properties of Optical Surfaces,” Ph.D. Dissertation, U. Arizona, 1976.

[Hayford and David, 1997] M. J. Hayford, S. R. David, "Characterization of illumination systems using LightTools,". Proc. SPIE 3130, Lens Design, Illumination, and Optomechanical Modeling, 1997.

[Hoelen et al., 2008] C. Hoelen, H. Borel, J. de Graaf, M. Keuper, M. Lankhorst, C. Mutter, L. Waumans and R. Wegh, "Remote phosphor LED modules for general illumination – towards 200 lm/W general lighting LED light sources," Proc. SPIE 7058, 2008.

[Hunt, 1998] R. W. G. Hunt, *Measuring color*, New York, John Wiley & Sons Ltd.,3rd edition, 1998.

[Joo et al., 2009] J. Y. Joo, C. S. Kang, S. S. Park and Sun-Kyu Lee, "LED beam shaping lens based on the near-field illumination," Opt. Express, vol. 17, pp. 23449-23458, 2009.

[Joshi et al., 2010] N. Joshi N, S. B. Kang, C. L. Zitnick and R. Szeliski, "Image deblurring using inertial measurement sensors," ACM Trans. Graph., vol. 29, no. 4, pp. 30:1-30:9, 2010.

[Kari et al., 2011] T. Kari, J. Gadegaard, T. Søndergaard, T. Pedersen, and K. Pedersen, "Reliability of point source approximations in compact LED lens designs," Opt. Express, vol. 19, A1190-A1195, 2011.

[Kim et al., 2008] W. Kim, H. T. Ahn and J. T. Kim, "A first approach to discomfort glare in the presence of non-uniform luminance," Building and Environment, vol. 43, no. 11, pp. 1953-1960, 2008.

[Koshel, 2002] R. J. Koshel, "Lit appearance modeling of illumination systems," Proc. SPIE 4768, pp. 65-73, 2002.

[Krokstad et al., 1968] A. Krokstad, S. Strom and S. Sørsdal, "Calculating the acoustical room response by the use of a ray tracing technique," Journal of Sound and Vibration, vol. 8, no. 1, pp. 118–125, 1968.

[Leloup et al., 2008] F. B. Leloup, S. Forment, P. Dutré, M. R. Pointer and P. Hanselaer, "Design of an instrument for measuring the spectral bidirectional scatter distribution function," Applied Optics, vol. 47, no. 29, pp. 5454-5467, 2008.

[Leloup et al., 2012] F. B. Leloup, M. R. Pointer, P. Dutré and P. Hanselaer, "Overall gloss evaluation in the presence of multiple cues to surface glossiness," J. Opt. Soc. Am. A, vol. 29, pp. 1105-1114, 2012.

[Leloup, 2012] F.B. Leloup, "New methods and models improving the prediction of visual gloss perception," Ph. D. Dissertation, KU Leuven, 2012.

[Lewis, 1995] J.P. Lewis, "Fast template matching," Vision interface, pp. 120-123 1995.

[Li et al., 2006] H. Li, S-C Foo, K. E. Torrance and S. H. Westin, "Automated three-axis gonioreflectometer for computer graphics applications," Optical Engineering, vol. 45, no. 4, article 043605, pp. 1-11, 2006.

[LightTools, 2013] Synopsis Optical Solutions, http://optics.synopsys.com/lighttools/, accessed September 2013.

[Llacer and Veklerov, 1989] J. Llacer and E. Veklerov, "Feasible Images and Practical Stopping Rules for Iterative Algorithms in Emission Tomography," IEEE Transactions on Medical Imaging, vol. 8, pp. 186-193, 1989.

[Llacer and Veklerov, 1991] J. Llacer and E. Veklerov, "The use of a stopping rule in iterative image reconstruction," Lecture Notes-Monograph Series - Spatial Statistics and Imaging, vol. 20, pp. 209-226, 1991.

[López et al., 2012] M. López, K. Bredemeier, N. Rohrbeck, C. Véron, F. Schmidt and A. Sperling, "LED near-field goniophotometer at PTB," Metrologia, vol. 49, no. 2, s141, 2012.

[Malacara, 2004] D. Malacara and Z. Malacara, *Handbook of Optical Design*, Marcel Dekker, New York, 2nd edition, 2004.

[Mas et al., 2008] A. Mas, I. Martín, and G. Patow, "Compression and importance sampling of near-field light sources," Computer Graphics forum, vol. 27, no.8, pp. 2013-2027, 2008.

[Muschaweck, 2012] J. Muschaweck, "Optical design using luminance in ray data sets," Proc. SPIE 8485, 84850P, 2012.

[Muschaweck, 2011] J. Muschaweck, "What's in a ray set: moving towards a unified ray set format," Proc. SPIE 8170, 81700N, 2011.

[Nakamura, 2008] Y. Nakamura, “Method of discomfort glare estimation applicable to a wide range of source sizes -glare estimation system based on luminance image,” Light and Engineering, vol. 16, no. 1, pp. 84-88, 2008.

[Narendran, 2005a] N. Narendran, Y. Gu, J.P. Freyssinier-Nova and Y. Zhu, “Extracting phosphor-scattered photons to improve white LED efficiency,” Proc. SPIE 5941, 2005.

[Narendran, 2005b] N. Narendran, “Improved performance white LED,” Proc. SPIE 5941, 2005.

[Nickolls and Dally, 2010] J. Nickolls, W.J. Dally, “The GPU Computing Era,” Micro IEEE, vol. 30, no. 2, pp. 56-69, 2010.

[Nicodemus et al., 1977] F. E. Nicodemus, J. C. Richmond, J. J. Hsia, I. W. Ginsberg, and T. Limperis, “Geometric considerations and nomenclature for reflectance,” Monograph 160, National Bureau of Standards, 1977.

[Parker et al., 2010] S. G. Parker, J. Bigler, A. Dietrich, H. Friedrich, J. Hoberock, D. Luebke, D. McAllister, M. McGuire, K. Morley, A. Robison, and M. Stich, “OptiX: a general purpose ray tracing engine,” ACM Trans. Graph., vol. 29, no. 4, article 66, 2010.

[Paul and Einhor, 2000] P. M. Paul and H. D. Einhor, “Discomfort glare from small light sources,” Lighting Research and Technology, vol. 31., no. 4, pp. 139-143, 2000.

[Philips, 2013] Philips, “Luxeon Rebel White LED datasheet,” 2013, http://www.philipslumileds.com/, accessed February 2013.

[Phong, 1975] B. T. Phong, “Illumination for computer generated pictures,” Commun. ACM, vol. 18, pp. 311-317, 1975.

[Renka, 1988] R. J. Renka, “ALGORITHM 661: QSHEP3D: Quadratic Shepard Method for Trivariate Interpolation of Scattered Data,” ACM Trans. Math. Softw., vol.14, no. 2, pp. 151-152, 1988.

[Richardson, 1972] W. Richardson, “Bayesian-Based Iterative Method of Image Restoration,” JOSA, vol. 62, pp. 55-59, 1972.

[Rykowski, 2011] R. Rykowski, “Spectral ray tracing from near field goniophotometer measurements,” Light & Engineering, vol. 19, no. 1, pp. 23-29, 2011.

[Shan et al., 2008] Q. Shan, J. Jia and A. Agarwala, “High quality motion deblurring from a single image,” ACM Trans. Graph., vol. 27, no. 3, pp. 73:1-73:10, 2008.

[Sheng, 2006] L. Y. Sheng, “A study of light scattered by surface-relief holographic diffusers,” Optics Communications, vol. 264, no. 1, pp. 1-8, 2006.

[Smith, 2000] Warren J. Smith, Modern Optical Engineering: The Design of Optical Systems, McGraw-Hill, New York, 3d edition, 2000.

[Stover, 1995] J. C. Stover, *Optical Scattering: Measurement and Analysis*, SPIE, Bellingham, Washington, 2nd edition, 1995.

[Sun et al, 2006] C. C. Sun, T. X. Lee, S. H. Ma, Y. L. Lee, and S. M Huang, “Precise optical modeling for LED lighting verified by cross correlation in the midfield region,” Opt. Lett., vol. 31, pp. 2193-2195, 2006.

[Teppei et al., 2006] K. Teppei, A. Daisuke, I. Takashi, M. Takayoshi, T. Masahiro and I. Masami, “Discomfort glare caused by white LED light sources,” Journal of Light & Visual Environment, vol. 30, no. 2, pp. 95-103, 2006.

[Teppei et al., 2006] K. Teppei, A. Daisuke, I. Takashi, M. Takayoshi, T. Masahiro and I. Masami, “Discomfort glare caused by white LED light sources,” Journal of Light & Visual Environment, vol. 30, no. 2, pp. 95-103, 2006.

[TracePro, 2013] Lambda Research Corporation, http://www.lambdares.com/, accessed September 2013

[Withouck et al., 2013] M. Withouck, K. A. G. Smet, W. R Ryckaert, M. R. Pointer, G. Deconinck, J. Koenderink and P. Hanselaer, “Brightness perception of unrelated self-luminous colours;” J. Opt. Soc. Am. A, vol. 30, no. 6, pp. 1248-1255, 2013.

[Wyszecki and Stiles, 1982] G. Wyszecki and W. S. Stiles, *Color science: concepts and methods, quantitative data and formulae*, John Wiley & Sons Ltd., New York, 2nd edition, 1982.

[Xicato, 2013] Xicato, “XSM 80 Series LED Module Datasheet,” 2013, http://www.xicato.com, accessed February 2013.

[Yuan et al., 2007] L. Yuan, J. Sun, L. Quan and H-Y. Shum, “Image deblurring with blurred/noisy image pairs,” ACM Trans. Graph, vol. 26, no. 3, article 1, 2007.

Brief biography

Jan Audenaert was born on September 25, 1985 in Sint-Niklaas, Belgium. He graduated as Professional Bachelor in Information and Communication Technology from KAHO Sint-Lieven (Gent) in 2007. In 2009, he graduated as Master in Industrial Engineering from KAHO Sint-Lieven. His master thesis discussed the modeling and optimization of the boarding process of passengers on an airplane through the use of multi-agent simulations.

List of publications

Articles in internationally reviewed scientific journals

J. Audenaert, G. Durinck, F. Leloup, G. Deconinck, P. Hanselaer, "Simulating the spatial luminance distribution of planar light sources by sampling of ray files," Optics Express, vol. 21, no. 20, pp. 24099-24111, 2013.

J. Audenaert, F. B. Leloup, B. V. Giel, G. Durinck, G. Deconinck, P. Hanselaer, "Impact of the accurateness of bidirectional reflectance distribution function data on the intensity and luminance distributions of a light-emitting diode mixing chamber as obtained by simulations," Opt. Eng., vol. 52, no. 9, 095101, 2013.

J. Audenaert, F. B. Leloup, G. Durinck, G. Deconinck, P. Hanselaer, "Bayesian deconvolution method applied to experimental Bidirectional Transmittance Distribution Functions," Measurement Science & Technology, vol. 24, no. 3, 2013.

S. Leyre, F. B. Leloup, J. Audenaert, G. Durinck, J. Hofkens, G. Deconinck, P. Hanselaer, "Determination of the bulk scattering parameters of diffusing materials," Applied Optics, vol. 52, no 18, pp. 4083-4090, 2013.

W. Ryckaert, I. Roelandts, G. Durinck, S. Forment, J. Audenaert, P. Hanselaer, M. Van Gils, "Performance of led linear replacement lamps," Light & Engineering, vol. 20, no. 1, pp. 129-139, 2012.

Papers at international conferences and symposia, published in full in proceedings

V. Jacobs, R. Van Gaever, W. Ryckaert, M. Diltour, J. Audenaert, B. Van Giel, P. Hanselaer, P. Rombauts, "Simulating surgical luminaires by ray files," Proceedings of the 5th International Conference on Optical Measurement Techniques Optimess, 2012.

P. Acuna, S. Leyre, J. Audenaert, G. Durinck, G. Deconinck, P. Hanselaer, "Modeling of a reflective cavity for a remote phosphor LED application using ray-tracing software," Proceedings of the 11th Iberoamerican Conference on Lighting Luxamerica, pp. 32-37, 2012.

W. Ryckaert, I. Roelandts, M. Van Gils, G. Durinck, S. Forment, J. Audenaert, P. Hanselaer, “Performance of Led Linear Replacement Lamps,” 27th Session of the CIE, pp. 643-652, 2011.

J. Audenaert, G. Durinck, G. Deconinck, P. Hanselaer, “A case study on the importance of adequate input during the virtual prototyping stage of a luminaire,” Romanian Lighting Convention, pp. 84-89, 2011.

J. Audenaert, G. Durinck, F. Vandeghinste, G. Deconinck, P. Hanselaer, “Feasibility study of a brute-force ray tracing approach to obtain luminance maps of luminaires modeled with ray files,” SPIE Photonics Europe, 2010.

Meeting abstracts, presented at international conferences and symposia, published in proceedings or journals

K. Vandenberghe, J. Audenaert, G. Durinck, K. Labiau, W. De Geest, H. Coolens, P. Hanselaer, “Optical scattering by a holographic diffuser: measurements and data processing,” General Scientific Meeting of the Belgian Physical Society, 2013.

J. Audenaert, G. Durinck, F. Leloup, G. Deconinck, and P. Hanselaer, “Accurate measurement of the Bidirectional Transmittance Distribution Function of holographic diffusers,” Proceedings of 8th EOS Topical Meeting on Diffractive Optics, Abstract no. 4764_DO2012_01, 2012.

J. Audenaert, B. Van Giel, V. Jacobs, S. Forment, P. Hanselaer, “The use of near field goniophotometers for LED lighting applications,” Eclairage, 2012.

M. Verhoeven, J. Audenaert, G. Durinck, G. Deconinck, P. Hanselaer, “Optical measurements and ray tracing simulations of LED luminaires with a diffuse ceramic reflector,” General Scientific Meeting of the Belgian Physical Society, 2012.

M. Luxem, J. Audenaert, S. Leyre, G. Durinck, G. Deconinck, P. Hanselaer, “A remote phosphor LED module with a ceramic mixing chamber: optical measurements and ray tracing,” General Scientific Meeting of the Belgian Physical Society, 2012.

G. Durinck, J. Audenaert, W. Ryckaert, P. Hanselaer, “Illuminance and glare of two light sources with different luminance distributions,” 2nd CIE Expert Symposium on Appearance, When Appearance meets Lighting, 2010.